Stabilization of Carbon Nanotubes: An Infrared and Optical Spectroscopy Study on Peapods and Double-Walled Carbon Nanotubes under Pressure

Universität Augsburg

vorgelegt von

Badawi Ali Ahmed Anis

September 2013

Erstgutachter: Prof. Dr. Christine Kuntscher
Zweitgutachter: Prof. Dr. Wolfgang Brütting

Tag der mündlichen Prüfung: 06.09.2013

I would like to dedicate this thesis to the women in my life; my wife
Marwa, my daughters; Mariem and Maram and my loving parents.
For their love, and support over the years, which helped me
completing this dissertation.

Contents

CONTENTS

CONTENTS

Chapter 1

Introduction

Carbon nanotubes are one of the well-known allotrope of carbon with a cylindrical nanostructure. Since the discovery of carbon nanotubes by Iijima in 1991, there has been great interest in their structural, mechanical, thermodynamics, and electric properties. Among others their mechanical properties are attracting great interest. The robust mechanical properties of carbon nanotubes are due to the strong sp^2 covalent bonds between the carbon network. Recently, scientists have found that carbon nanotubes can be spun into a flexible conductive carbon thread that is few micrometers thick. These carbon threads are ten times the tensile strength of steel and is as conductive as copper, allowing the use of these materials in the light-weight, high-strength applications. Theoretical studies on the mechanical properties of the single-walled carbon nanotubes (SWCNTs) were predicted them to be very strong material, with an axial Young's modulus $\geqslant$ 1TPa. However, carbon nanotubes are known to be soft materials in its radial direction.

The main goal of the present work is to study the stability of carbon nanotubes via the pressure-induced changes in the optical response using hydrostatic pressure transmitting medium (PTM) up to 20 GPa. For this purpose, fullerene doped SWCNTs, or what is called peapods method, was used to prepare different variety of carbon nanotubes namely: C_{60}, C_{70} peapods, and double-walled carbon nanotube (DWCNTs) derived from the peapods. Additionally, iodine-filled SWCNTs (I-SWCNTs) were also prepared to extend the comparison to the effect of atoms filling on the stability of the SWCNTs and compare the results with

those of the peapods and DWCNTs.

The stability of the different carbon nanostructures: peapods, DWCNTs, and I-SWCNTs, against hydrostatic pressure has been mainly addressed by Raman spectroscopy, which monitors the vibrational properties of the nanotubes. Optical spectroscopy coupled with high pressure technique forms a powerful and novel tool to probe the electronic structure of carbon nanotubes.

Investigations proposed that at a critical pressure, a modification of the nanotubes cross section from circular to oval, elliptical or collapse at high pressure occurs. Due to the nanotube' cross-section modification, the electronic and the optical properties of the deformed tubes are strongly affected. For example, the optical absorption spectra are altered drastically under pressure, where the main absorption bands shift to lower frequencies, broaden, lose spectral weight, and finally vanish. This behaviour was attributed to the symmetry breaking and/or σ^*-π^* hybridization. The mechanical stability of the SWCNTs by filling the tubes with molecules, atoms, or with inner tube is an important issue. High-pressure Raman measurements showed that the filling with inner tubes or Argon molecules stabilizes the outer tubes and this kind of filling considered as a case of homogenous filling. On the other hand, filling nanotubes with C_{70} molecules or iodine atoms, a case of inhomogeneous filling, leads to destabilization of the nanotubes. The destabilization of the nanotubes was attributed to the inhomogeneous interaction, non-covalent van der Waals forces, between the nanotubes walls and the inner molecules, which can lead to the tube mechanical instability even at low pressure.

In general, optical spectroscopy is a powerful technique to characterize the electronic band structure in terms of the energy position and spectral weight of the excited optical transitions. As demonstrated recently, the optical response is capable of monitoring small pressure-induced deformations of the tubular cross-section, as the characteristic van Hove singularities (vHS) in the density of states in SWCNTs are very sensitive to such deformations. Within the present work, the relevance of PTM regarding the pressure-induced effects in sample under investigation will be clarified. It has been demonstrated perviously that fluids, nitrogen or argon as PTM can intercalate inside the SWCNTs, introducing a steric barrier which is responsible for the SWCNTs stabilization against the applies

pressure. Therefore, nitrogen, argon, and alcohol mixture as PTM were used to clarify the effect of the different PTM on the stability of the samples under investigations.

The overall structure of the present study takes the form of six chapters, including this introductory chapter. Chapter 2 begins by showing the theoretical dimensions of the carbon nanotube, structure of peapods, formation mechanism of the DWCNTs, and theories explaining the stability of nanotube under pressure. The third chapter is concerned with the methodology used for the present study, mainly infrared spectroscopy in combination with high-pressure technique. Also, theories related to the optical response functions and the models used for analyzing the optical spectra are presented. Chapter 4 presents the preparation methods of the samples and the characterization of the samples using: high resolution transmission electron microscope (HRTEM), Raman, and optical spectroscopy. Chapter 5 analyzing and discussing the important finding of the the present work in details about the effect of the inner filler on the mechanical stability of the SWCNTs under pressure. Finally, chapter 6 gives a brief summary and the most important findings of this thesis and includes a brief outlook of the implication of the findings to future research into this area.

Chapter 2

Properties of Carbon Nanotubes

2.1 History of Graphene

Graphene is the name given to a two-dimensional (2D) honeycomb lattice made out of one atomic thick layer of carbon atoms [1]. In 1947 Wallace [2], constructed a theoretical model for a 2D crystal arranged in a honey-comb lattice to calculate the structure of graphite, but no one at this time thought that it is possible to isolate only one atomic thick layer of carbon atoms. In 2004, a research group from Manchester University led by A. Geim and K. Novoselov demonstrated a simple method to isolate single layer graphene (SLG) from the highly oriented pyrolytic graphite (HOPG) using scotch tape to exfoliate graphene layers from the three-dimensional (3D) graphite [3, 4]. The exfoliated layers can be easily transferred on the top of SiO_2 substrate that allow its observation with normal ordinary microscope [5]. In 2010, the Nobel prize in physics was awarded jointly to Andre Geim and Konstantin Novoselov for the ground breaking experiments regarding the preparation and characterization of the 2D graphene material. At this event, graphene agitates the scientist's curiosity who share common background: physicists, chemists, biologists, engineers, and theorists to explore its unusual properties [6].

Graphene is considered as the mother of all known carbon allotropes: fullerenes, carbon nanotubes, and graphite [see Figure 2.1]. In Fullerenes molecules, the carbon atoms are arranged spherically. By the introduction of pentagons, fullerene

Figure 2.1: Graphene is the mother of all graphitic forms. Graphene is a 2D building material for all carbon allotropes. It can be wrapped up into (a) 0D buckyballs, (b) rolled into 1D nanotubes or (c) stacked into 3D graphite [1].

can be considered as a wrapped-up graphene [7]. Carbon nanotubes can be considered as a one-dimensional (1D) material obtained by rolling graphene sheet in a certain direction [8]. Graphite is considered as a 3D material made out of weakly stacked graphene layers [9].

2.2 Band Structure of the Graphene

2.2.1 Hybridization in Graphene

All carbon-based materials: diamond, graphite, graphene, fullerenes, and carbon nanotubes are unique in many ways. The superiority of the carbon-based materials over other materials is related to the many possibilities of the arrangements of the electronic state of the carbon atom, which is known as the hybridization of the atomic orbitals. Each carbon atom has six electrons with the $1s^2$, $2s^2$, $2p^2$ electronic configuration. The two electrons in the $1s$ orbital are strongly bound and they are called the core electrons. The less bound four electrons in the $2s$ and $2p$ orbitals are called the valence electrons. The energy difference between the $2s$ and $2p$ orbitals is small, so the electronic wavefunctions of these four electrons can mix or hybridize easily with each other. In graphene, carbon atoms are attached together by the overlapping between the sp^2 hybridized orbitals, where the $2s$ orbital is mixed with the two $2p$ orbitals, namely p_x and p_y. The hybridized orbitals are connected together in a planar assembly with $120°$ between

them forming σ-bonds in the xy plane. The additional p_z orbital is perpendicular to the sp^2 orbitals and forms the π-bonds [see Figure 2.2]. In all carbon allotropes, the σ-bonds are responsible for the robustness of the lattice structure. According to Pauli principle, the σ-bonds have a filled shell, and hence form the deep valence band [8, 10].
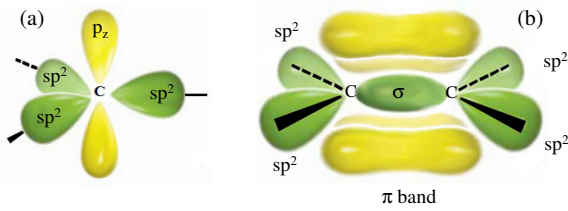
Figure 2.2: (a) 3 sp^2 hybrid orbitals in a planar assembly with 120°. The p_z orbital is perpendicular to the sp^2 orbitals. (b) The π bond occurs between the p_z orbitals and the σ bond is a direct overlap between the sp^2 hybrid orbitals [11].

2.2.2 Tight Binding Model for Graphene

Wallace in 1947 [2], was the first one to use the tight binding model (TBM) for describing the band structure of 2D graphene. In the TBM, the nearest and next nearest neighbours interactions for the p_z orbitals were considered and the overlap between wavefunctions at other atoms was neglected. Saito *et al.* [8] have nicely described the TBM for graphene. They considered only the interaction between the nearest neighbours with nonfinite overlap between wavefunctions. According to Wallace and Saito [2, 8], the interaction between the two adjacent layers in the 3D graphite was neglected compared to the intra-layer interaction, because the separation distance between the two graphene layers is 3.35Å which is larger than the distance between the nearest neighbour $\approx$1.42Å. Thus, the electronic structure of the 2D graphene layer is considered as a first approximation of the 3D graphite.

Figure 2.3 (a) shows the unit cell of graphene in real space marked with dotted rhombus and (b) the first Brillouin zone represented by a shaded hexagon. In the real space, each unit cell can be represented by two atoms A and B and spanned by the units vectors $\vec{a_1}$ and $\vec{a_2}$ enclosing an angle of 60°. In the xy plane, the real vectors $\vec{a_1}$ and $\vec{a_2}$ can be represented as

$$\vec{a_1} = \left(\sqrt{3}, 1\right) \frac{a}{2}, \qquad \vec{a_2} = \left(\sqrt{3}, -1\right) \frac{a}{2} \tag{2.1}$$

2. Tight Binding Model for Graphene

(a)

(b)
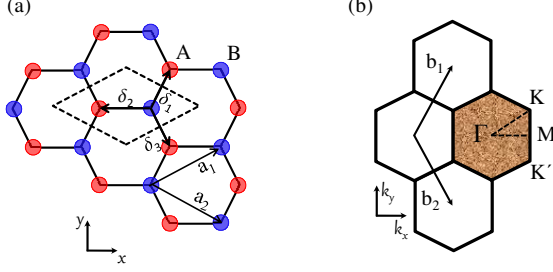
Figure 2.3: (a) Honeycomb lattice structure of graphene. The a_1 and a_2 are the lattice unit vectors and δ_i, $i = 1,2,3$ are the nearest-neighbor vectors. (b) The first Brillouin zone represented by a shaded hexagon. The high symmetry points Γ, K, and M are the centre, the corner, and the centre of the edge, respectively.

where a $= |\vec{a_1}| = |\vec{a_2}| = $ a$_{C-C} \times \sqrt{3} = 1.42 \times \sqrt{3} = 2.46$ Å. a$_{C-C}$ is the carbon-carbon distance. Using the relation between the real and reciprocal spaces in Ref. [12], the reciprocal space lattice vectors $\vec{b_1}$ and $\vec{b_2}$ can be written as

$$\vec{b_1} = \left(\frac{1}{\sqrt{3}}, 1\right)\frac{2\pi}{a}, \qquad \vec{b_2} = \left(\frac{1}{\sqrt{3}}, -1\right)\frac{2\pi}{a} \tag{2.2}$$

The three nearest-neighbor vectors in real space are given by [13]

$$\delta_1 = \frac{a}{2}\left(\frac{1}{\sqrt{3}}, 1\right), \delta_2 = \frac{a}{2}\left(\frac{1}{\sqrt{3}}, -1\right), \text{and} \quad \delta_3 = -\frac{a}{\sqrt{3}}(1,0) \tag{2.3}$$

In Figure 2.3 (b), the shaded hexagon represents the first Brillouin zone with the high symmetry points Γ, K, and M as the centre, the corner, and the centre of the edge, respectively. The two corners points K and K' are of particular interest for the physical properties of graphene. These two points are called Dirac points. The reason for giving this name will be explained later. Their positions in the momentum space are given by [13]

$$K = \left(\frac{2\pi}{\sqrt{3}a}, \frac{2\pi}{3a}\right), \qquad K' = \left(\frac{2\pi}{\sqrt{3}a}, -\frac{2\pi}{3a}\right) \tag{2.4}$$

For energy dispersion relation calculation, tight binding Bloch function should be considered [8]

$$\phi_j(\vec{k}, \vec{r}) = \frac{1}{\sqrt{N}}\sum_{\vec{R_j}}^{N} e^{i\vec{k}\cdot\vec{R}}\phi_j(\vec{r} - \vec{R_j}), \qquad (j = 1, ..., n) \tag{2.5}$$

2. Tight Binding Model for Graphene

Here, $\vec{R}_j$ is the position vector of the jth atom, $\varphi_j(\vec{r} - \vec{R}_j)$ is the local orbital of the jth atom, and N is the number of the primitive cell. According to the TBM, the electronic wavefunctions from different atoms on the hexagonal lattice can overlap. However, such overlap between the $p_z(\pi)$ and the s or p_x and p_y orbitals is strictly zero due to the symmetry of the lattice [14]. Therefore, only the p_z orbitals will be considered. By taking into account only the first nearest neighbours interactions, so the three nearest B atoms relative to A atom will be denoted by the vectors $\vec{R}_1$, $\vec{R}_2$, and $\vec{R}_3$ and defining 2×2 matrix Hamiltonian

$$H_{jj'}(\vec{k}) = \langle \phi_j | H | \phi_{j'} \rangle \qquad (j, j' = 1, ..., n) \tag{2.6}$$

Then, the contributions from the $\vec{R}_1$, $\vec{R}_2$, and $\vec{R}_3$ can be written as follows:

$$H_{AB}(\vec{k}) = \gamma_o(e^{i\vec{k}\cdot\vec{R}_1} + e^{i\vec{k}\cdot\vec{R}_2} + e^{i\vec{k}\cdot\vec{R}_3}) \tag{2.7}$$

Form the Hamiltonian $H_{AB}(\vec{k})$ and after some algebraic manipulation, the eigenenergies which give the dispersion relation of graphene can be calculated [for more details see Ref. [8]]. Then, the expression of the dispersion relation can be written as follows:

$$E(k_x, k_y) = \frac{\varepsilon_{2p} \pm \gamma_o w(\vec{k})}{1 \pm s w(\vec{k})} \tag{2.8}$$

where the phase factor $w(\vec{k})$ can be written as

$$w(\vec{k}) = \sqrt{1 + 4\cos\frac{\sqrt{3}k_x a}{2}\cos\frac{k_y a}{2} + 4\cos^2\frac{k_y a}{2}}, \tag{2.9}$$

ε_{2p} is the orbital energy of the 2p level, and the parameter γ_o is the transfer integral between the first-neighbour π-orbitals (typical values for γ_o are -2.9 to -3.1 eV). The parameter s is the overlap integral between the nearest A and B atoms. The plus sign applies to the upper π^*-energy anti-bonding band and the minus sign to the lower π-energy bonding band.

Figure 2.4 (a) and (c) show the energy dispersion relation of the 2D graphene throughout the Brillouin zone and along the high symmetry direction of Γ, K, and
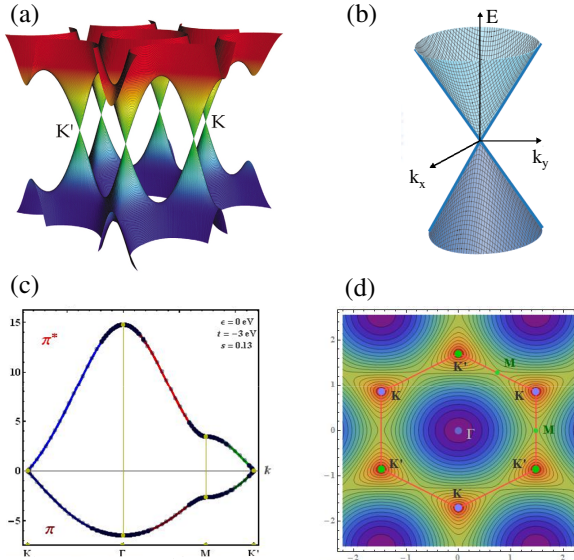
2. Tight Binding Model for Graphene

Figure 2.4: (a) Band structure of graphene. The conduction band touches the valence band at the K and K′ points [15]. (b) Enlargement of the band structure close to the K point, showing a linear spectrum (blue lines). The conical conduction band (upper cone) and valence band (lower cone) touch at the Dirac point [16]. (c) The energy dispersion along the high-symmetry directions ΓMK of the 2D Brillouin zone. (d) The contour plot of the 2D energy bands of graphene [17].

M points. The parameters ε_{2p}=0, γ_o=-3 eV, and s=0.13 were used in order to reproduce the first principle calculations of the graphene energy bands [8, 18, 19]. The upper π* and the lower π bands are degenerate at the K points through which the Fermi energy passes. When the overlap integral s becomes zero, the π and π* band structure becomes symmetric around $E = \epsilon_2 p$. In this case, the graphene energy dispersion relations are used as a simple approximation for the graphene electronic structure [8, 20]:

$$E(k_x, k_y) = \gamma_o \sqrt{1 + 4\cos\frac{\sqrt{3}k_x a}{2}\cos\frac{k_y a}{2} + 4\cos^2\frac{k_y a}{2}} \qquad (2.10)$$

Figure 2.4 (b) shows an enlargement of the band structure close to the K and K′. It is clear that conduction and valence bands are shaped like an inverted pair of cones and meet each others at $E = 0$ in the momentum space. This means that graphene is a half-metal with zero band gap. This zero gap could be related to the high symmetry between the two atoms A and B in the unit cell. Near the K point, the energy dispersion is linear, characteristic of massless particles such as photons and the electrons which can be described by Dirac equation for massless relativistic particles rather than the Schrödinger equation. This is the reason to call the K point as Dirac point [16]. Figure 2.4 (d) shows the contour plot of the

9

2D energy bands of graphene. The equi-energy contours are circles near the Dirac points but close to the zone boundary the contours are straight lines, connecting the three nearest M points [20].

2.3   Structure of Single-Walled Carbon Nanotubes

Single-walled carbon nanotube (SWCNT) can be constructed by rolling up a graphene sheet into a seamless cylinder. The SWCNT structure can be specified by the chiral vector C_h [see Figure 2.5], which defines the circumference of the nanotube. The chiral vector C_h can be written as a function of the graphene unit vectors $\vec{a_1}$ and $\vec{a_2}$ as follows:

$$C_h = na_1 + ma_2 \equiv (n, m) \tag{2.11}$$

where n and m are two arbitrary integers numbers. The chiral vector C_h is shortly written as (n,m) and this notation is used to characterize the geometry of the nanotubes. The chiral vector C_h makes an angle (θ) with the vector a_1 direction, so called the zigzag direction. The angle θ is called the chiral angle. Figure 2.6 shows different carbon nanotubes structures depending on the values of n, m, and θ. Carbon nanotube is called zigzag, if $\theta=0$ and m=0 and armchair, if $\theta=30°$ and n=m. All other nanotubes are called chiral and have a chiral angle with $0°<\theta<30°$ [8, 21]. The chiral angle θ and the nanotube diameter d_t can be expressed in terms of both n and m indices as follows:

$$d_t = \frac{a}{\pi}\sqrt{n^2 + nm + m^2} \tag{2.12}$$

$$\theta = \arccos\left(\frac{2n + m}{2\sqrt{n^2 + nm + m^2}}\right) \tag{2.13}$$

To define the unit cell of the SWCNT, the vector T is defined as the shortest repeat distance along the tube axis [24] [see Figure 2.5]. Thus, the T vector can

2. Structure of Single-Walled Carbon Nanotubes
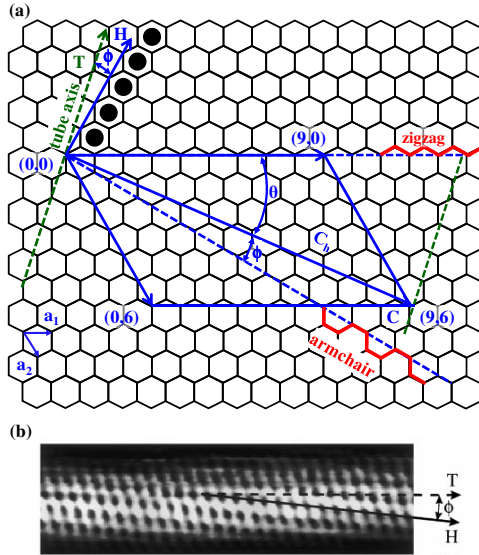
Figure 2.5: (a) An unrolled carbon nanotube projected on the graphene sheet. By rolling the nanotube, the chiral vector C_h turns on the circumference of the tube. Rolling the sheet along the dotted lines leads to zigzag or armchair nanotubes, with θ equals to $0°$ or $30°$, respectively. All other tubes are called chiral with a chiral angle $0° < \theta < 30°$. The vector H is perpendicular to the armchair direction and specifies the direction of nearest-neighbour hexagon rows indicated by the black dots. The vector T is perpendicular to the C_h and run in the direction of the nanotube axis. (b) Atomically resolved scanning tunneling microscopy (STM) image of individual single-walled carbon nanotube (SWCNT) [22].
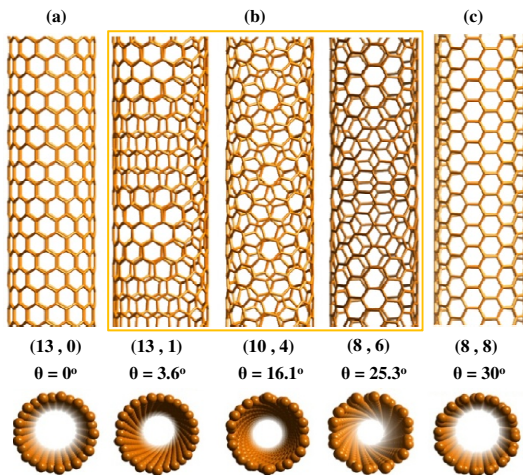
Figure 2.6: Structure of single-wall with different chiral angles between $0°$ and $30°$ and : (a) Zigzag, (b) chiral, and (c) armchair [23].

11

2. Structure of Single-Walled Carbon Nanotubes

be written as

$$T = t_1 a_1 + t_2 a_2 \equiv (t_1, t_2) \tag{2.14}$$

the coefficients t_1 and t_2 can be expressed by the two indices n and m as

$$t_1 = (2m + n)/d_R, \qquad t_2 = -(2n + m)/d_R \tag{2.15}$$

the constant d_R is the greatest common divisor of the $(2n + m, 2m + n)$ and is given by

$$d_R = \begin{cases} d, & \text{if } n - m \text{ is not a multiple of } 3d, \\ 3d, & \text{if } n - m \text{ is a multiple of } 3d \end{cases} \tag{2.16}$$

the unit cell of the SWCNT can be defined as the area enclosed by the two vectors C_h and T. The number of the hexagons, N, contained in the unit cell of the SWCNT can be expressed by the two indices n and m as

$$N = 2(m^2 + n^2 + nm)/d_R \tag{2.17}$$

Both chiral vector C_h and lattice vector T determine the SWCNT unit cell in the real space. In the reciprocal space, the corresponding vectors are K_1 along the circumferential direction and K_2 along the nanotube axis. The two reciprocal vectors K_1 and K_2 can be written as

$$K_1 = 1/N \, (-t_2 b_1 + t_1 b_2), \qquad K_2 = 1/N \, (m b_1 - n b_2) \tag{2.18}$$

where b_1 and b_2 are the reciprocal lattice vectors of the 2D graphene. The values of b_1 and b_2 are given in Equation 2.2. The unrolled SWCNT is prolonged in the direction of the T vector and has a nanoscale dimension in the direction of the chiral vector C_h, so the unrolled reciprocal space of the SWCNT is quantized along K_1 and continues along K_2 direction [21, 24]. From the expression of K_1, the $NK_1 = (-t_2 b_1 + t_1 b_2)$ is a transitional wavevector in the reciprocal space of the unrolled SWCNT. The N wavevectors, μK_1, give rise to N quantized states

in the direction of K_1, where μ is an integer number varying from $(1 - N/2)$ to $(N/2)$. Each discrete value of these N quantized states gives rise to a line of length $| K_2 |$ along the K_2 direction and a separation distance K_1 between the adjacent lines [see Figure 2.7]. The line segments defined by K_1 and K_2 in the reciprocal space of the unrolled SWCNT represent what is called cutting lines [10, 21, 24]. Figure 2.7 shows an example model for (4, 2) SWCNT, the number of the cutting lines is $N = 28$ (according to Equation 2.17). They are numbered by the index μ and ranging from $1 - N/2 = -13$ to $N/2 = 14$, where the middle cutting $\mu = 0$ line passes through the Γ point. The wavevectors along the nanotubes axis become also quantized, when the length of the nanotubes is short enough, but still higher than the unit cell length. In this case the quantization will take the form $\xi(T/L)K_2$, where ξ is an integer and ranging from $(2T - L)/2T$ to $L/2T$ [10].
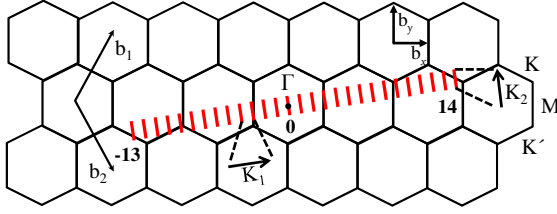
Figure 2.7: Reciprocal space of the graphene layer. The parallel red thick lines represent the 28 cutting lines for the (4, 2) SWCNT. The cutting lines are ranging from $1 - N/2 = -13$ to $N/2 = 14$, where the middle cutting $\mu = 0$ line passes through the Γ point. The dashed dotted lines represent the spacing between the adjacent lines K_1 and the length of the line K_2 [21].

2.3.1 Zone-Folding of Energy Dispersion Relations

When the 1D SWCNT is rolled up from the 2D graphene sheet, different subbands in the 1D reciprocal space of the SWCNT can be extended into the 2D reciprocal space of the graphene sheet as a set of cutting lines. This method of constructing the 1D subbands by cutting the 2D graphene electronic dispersion relation with lines is known as the zone-folding scheme [8]. The zone-folding scheme is very useful in carbon nanotube science but it encounters certain limitations for small-diameter SWCNT $\leqslant$0.6 nm. Within the zone-folding scheme calculations, the effect of hybridization between the in-plane σ orbitals and the out-of-plane π orbitals due to the large curvature of the small tubes is completely ignored.

2. Zone-Folding of Energy Dispersion Relations

Furthermore, the weak van der Waals interaction between the nanotubes due the bundling effect is also ignored, where some corrections might be needed [21]. In order to construct the electronic energy dispersion for the 1D SWCNT, the cutting lines through the first Brillouin zone of the 2D graphene should be fully represented. To construct the cutting lines representation, each cutting line is drawn originating from the Γ point in the first Brillouin zone, with an inclination angle $\phi = \pi/6 - \theta$, to the edges of the Brillouin zone. The other cutting lines are drawn parallel to the central one at distance equal to $|K_1| = 2/d_t$, where d_t is the diameter of the SWCNT, until the first Brillouin zone is completely filled with the cutting line as shown in Figure 2.8 (a), where the dashed lines represent the ends of the cutting lines. This representation is called fully reduced representation. The two others representations are shown in Figure 2.8 (b) and (c), they are called fully K_1 extended representation and fully K_2 extended representation, respectively. From the fully reduced representation, the fully K_1 extended representation can be obtained by shorting the length of cutting lines [solid lines in Figure 2.8 (a)] by a set of parallel equidistant broadening lines [dotted lines in Figure 2.8 (b)]. The distance between the broadening lines is $|K_2| = 2\pi/|T|$. Finally, all the segments will be shifted by the reciprocal lattice vector NK_1, form the fully K_1 extended representation. The fully K_2 extended representation can be obtained from the fully K_1 extended representation [as shown in Figure 2.8 (c)] by drawing a dark gray rectangle passes through the Γ point, then prolonging the rectangles in the K_2 direction. The translation of the new rectangles (light gray rectangles) must equal to $K_2 - MK_1$, where M is an integer number and equal to the shifts cutting lines between the adjacent K_1 extended representations (dark and light gray rectangles). The $K_2 - MK_1$ vector represents the separation distance between two Γ points in two adjacent rectangles. Then by continue adding rectangles till all the N cutting lines are arranged in a single line of length NK_2, as shown in Figure 2.8 (c) [10, 21].

To study the band structure of SWCNT, the zone-folding scheme to the graphene electronic dispersion relations will be applied. When the graphene energy dispersion relations are folded, the N pairs of the $1D$ energy dispersion relations $E_\mu(k_x, k_y)$ are obtained. The $1D$ energy dispersion relations are given by [10, 25]
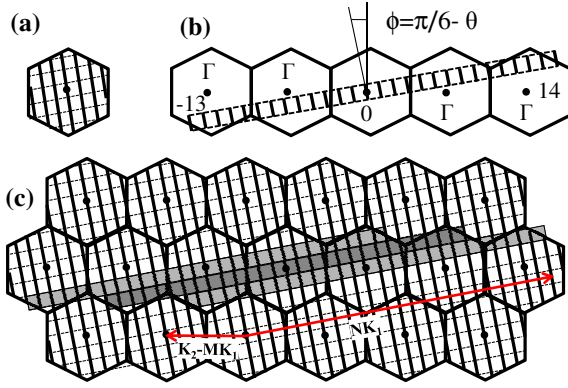
Figure 2.8: (a) The fully reduced representation of the cutting lines for (4, 2) SWCNT, filling the area of the first Brillouin zone of the graphene layer. (b) The fully K_1-extended representation of the cutting lines for (4, 2) nanotube. The solid lines represent the cutting line, where the dashed lines represent the ends of the cutting lines. (c) The fully K_2-extended representation of the cutting lines for (4, 2) nanotube. Several adjacent K_1-extended representation are arranged in lattice with basic vectors NK_1 and $K_2 - MK_1$ [21].
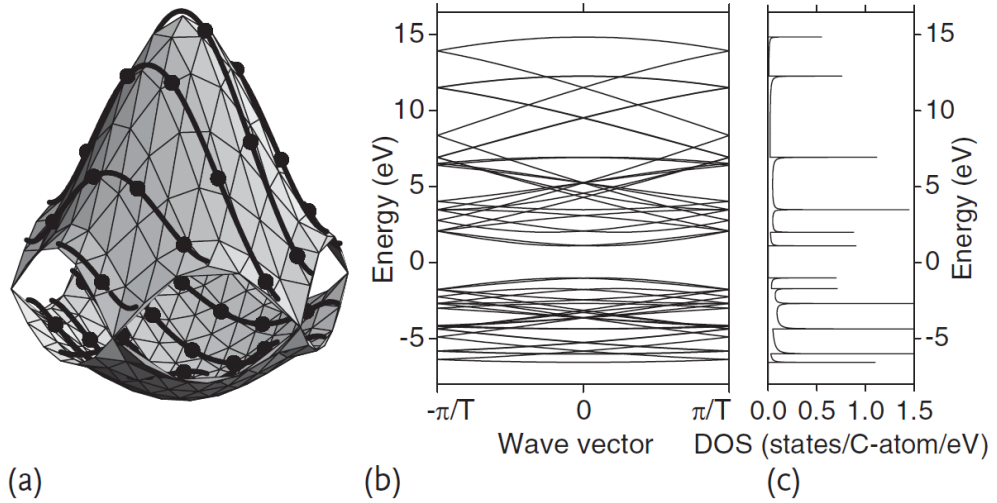
Figure 2.9: (a) The conduction and valence bands of the 2D graphene in the first Brillouin zone. Solid curves show the cutting lines for (4, 2) nanotube in the fully reduced representation. Solid dots show the ends of the cutting lines in the K_1 extended representation. (b) Band diagram of (4, 2) SWCNT obtained from the zone folding scheme of (a). (c) Density of states for the band diagram shown in (b) [10].

2. Zone-Folding of Energy Dispersion Relations

$$E_\mu(k) = E_{g2D}\left(q\frac{K_2}{|K_2|} + \mu K_1 \right) \qquad \text{with} \qquad \mu = 0, ..., N-1 \qquad (2.19)$$

where μ is discrete quantum number, $-\pi/T \leqslant q \leqslant \pi/T$, and E_{g2D} are the dispersion relation of the $2D$ graphene given by Equation 2.10. Thus the structure of the SWCNT can be obtained from the cross-sectional cutting of the $2D$ graphene energy dispersion as shown in Figure 2.9 (a), where the cuts are made as lines $qK_2/|K_2| + \mu K_1$. Following the zone-folding scheme, the electronic energy band diagram of the SWCNT can be obtained by placing the $E(k)$ for all the cutting lines from Figure 2.9 (a) in the $1D$ Brillouin zone of SWCNT as shown in Figure 2.9 (b). Figure 2.9 (c) shows the corresponding density of state (DOS). One can clearly observe in Figure 2.9 (c) the presence of spikes, or what is called van Hove singularities (vHS), in the DOS of the (4, 2) SWCNT. Each vHS originates from a different cutting lines [21].

For SWCNT, if a cutting passes through the K point of the $2D$ Brillouin zone, then the $1D$ energy bands have a zero energy gap and the nanotube is metallic. Otherwise, the nanotube is expected to show a semiconducting behaviour, with finite energy gap. The general condition for the metallic nanotubes is that the ratio of the YK vector to K_1 in Figure 2.10 is an integer [10]. The YK vector is given by

$$YK = \frac{2n+m}{3}K_1 \qquad (2.20)$$

If $(2n + m)$ or simply $(n - m)$ is a multiple of 3, then the nanotube is metallic. For armchair nanotubes, where $n = m$, are always metallic and for zigzag nanotubes, where $m = 0$, are only metallic when n is a multiple of 3. The three different cases of nanotubes are shown in Figure 2.11. In the case of metallic tubes the cutting line passes through the K point, as shown in Figure 2.11 (a). The two cases of semiconducting tubes are shown in Figure 2.11 (b) and (c). The two cases are different from each others, depending on which side of the K point, the first vHS will appear. The two cases are denoted by $S1$ and $S2$, where the $S1$ case refers to $2n + m = 3l + 1$ nanotubes and the

$S2$ case refers to $2n + m = 3l + 2$ nanotubes, where l is an integer [10, 21].
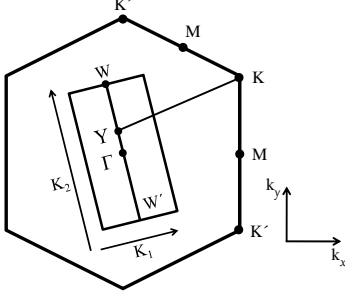
Figure 2.10: The condition for metallic energy bands: if the ratio of the length of the vector YK to that of K_1 is an integer, metallic energy bands are obtained. [10]
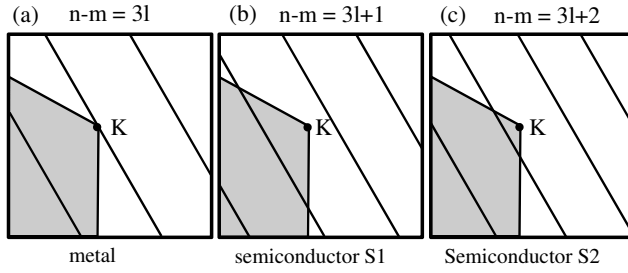
Figure 2.11: Different configurations of the cutting lines in the vicinity of the K point. (a) configuration $n - m = 3l$ corresponds to the case of metallic nanotubes. (b) and (c) configurations $n - m = 3l + 1$ and $n - m = 3l + 2$ correspond to the case of semiconducting tubes [10].

2.3.2 Electronic Density of States

As discussed perviously that the structure of SWCNT can be obtained from the cross-sectional cutting of the $2D$ graphene energy dispersion. This technique is shown in Figure 2.12 (a) for the states near the K point. The DOS related to the SWCNT band structure are shown in Figure 2.12 (b), where each cutting line in Figure 2.12 (a) gives rise to a local maximum in the DOS. In 1998, Charlier and Lambin [27] performed the first DOS calculation for the chiral carbon nanotubes. In the same year Mintmire and White [26, 28] published a universal DOS calculation for carbon nanotubes [29]. According to Mintmire and White [26, 28], the universal equation for the carbon nanotubes DOS is given by

$$n(E) = \frac{4a}{\pi^2 d \gamma_o} \sum_{m=-\infty}^{m=\infty} g(E, E_\mu) \tag{2.21}$$
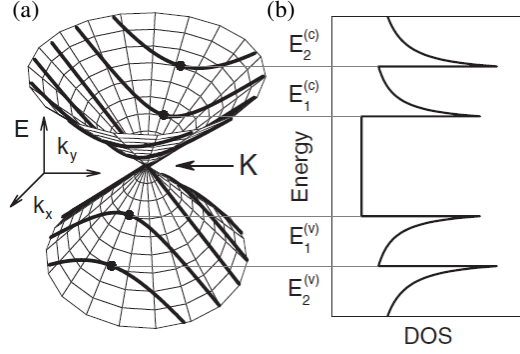
Figure 2.12: (a) The energy-momentum contours for the valence and conduction bands for a $2D$ system. The cutting lines of these contours denote the dispersion relations for SWCNT. Each cutting line gives rise to different energy sub-band. The energy extremum E_i for each cutting line at the wave vector k_i is known as the vHS. The energies $E_i^{(v)}$ and $E_i^{(c)}$ for the valence and conduction bands and the corresponding wave vectors $k_i^{(v)}$ and $k_i^{(c)}$ at the vHS are indicated on the figure by the solid dots. (b) The $1D$ density of states (DOS) for the conduction and valence bands in (a). The DOS shown in (b) is for a metallic $1D$ system, because one of the cutting lines in (a) crosses the K point in the graphite Brillouin zone [21].
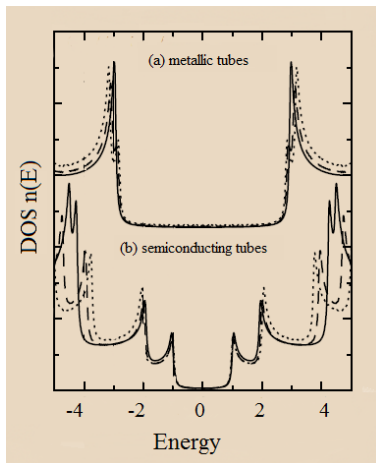
Figure 2.13: (a). Density of states for metallic nanotubes with different chiralities. Shown are the DOS for the (10,10) [solid line; d=1.36 nm, $\theta = 30°$], (14,5) [dashed line; d=1.34 nm, $\theta = 15°$], and (16,1) [dotted line; d=1.29 nm, $\theta = 3°$].(b) Density of states for semiconducting nanotubes with different chiralities. Shown the DOS for the (17,0) [solid line; d=1.33 nm, $\theta = 0°$], (13,6) [dashed line; d=1.32 nm, $\theta = 18°$], and (11,9) [dotted line; d=1.36 nm, $\theta = 27°$] [26]

2. Electronic Density of States

with

$$g(E, E_\mu) = \begin{cases} |E|/\sqrt{E^2 - E_\mu^2}, & |E| > |E_\mu| \,; \\ 0, & |E| < |E_\mu| \,. \end{cases} \tag{2.22}$$

E_μ is the quantized energy along $K_\perp$ (along the tube circumference). The quantized energy E_μ is given by

$$E_\mu = |3\mu - n - m| \gamma_o \frac{a_o}{\sqrt{3}d} \tag{2.23}$$

For $E_\mu \neq 0$, the function $g(E, E_\mu)$ shows a divergence at $E = E_\mu$ as expected for the 1D systems. For $E_\mu = 0$, the function $g(E, E_\mu) = 1$, i.e., the DOS is constant and not equal to zero, simply the case of metallic tubes. From Equation 2.23, it is clear that the DOS function is inversely proportional to the nanotube diameter d and directly proportional to the nanotubes chiral indices n and m. In general, E_μ can be written as $E_\mu = ia_o\gamma_o/\sqrt{3}d$ with $i = 3, 6$ for metallic nanotubes and $i = 1, 2, 4, 5, 7$ for semiconducting tubes [29]. Figure 2.13 (a) and (b) illustrates the DOS for different metallic and semiconducting nanotubes of different chiralities, respectively. In general, knowledge of DOS dominates many physical properties of carbon nanotubes [29]. The electronic band structure of the SWCNTs calculated from the zone-folding scheme do not include the effect of curvature of the nanotube. Hence, the zone-folding scheme can be considered as a good approximation for the larger-diameters nanotubes. For the nanotubes with diameters less than 1 nm, the first principles calculations using density functional theory (DFT) must be applied to calculate the band structure [30]. Within the zone-folding scheme [31], the energy between the ith vHS below the above the Fermi level can be written as

$$E_{ii} = \frac{2ia_{C-C}\gamma_o}{d} \tag{2.24}$$

where $i = 3, 6$ for metallic nanotubes and $i = 1, 2, 4, 5, 7$ for semiconducting tubes. The number i denotes the order of the valence and conduction energy bands. The optical transitions $E_{ii'}$ from the ith valence band to the $i'th$ conduction band occurs according to the selection rule of $\delta_{ii'} = 0$ and $\delta_{ii'} = \pm 1$ for parallel and
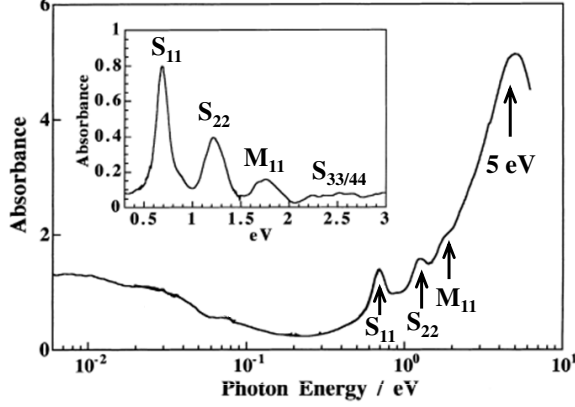
Figure 2.14: Optical absorption spectrum of SWNTs film at atmospheric pressure in a wide energy range from UV to FIR. Inset: for convenience, by subtracting the large absorption background due to π-plasmon, the absorption features labeled S_{11}, S_{22}, and M_{11} are clearly displayed [34].

perpendicular polarization of the incident electric field with respect to the carbon nanotube axis, respectively [32]. The optical transitions are suppressed in the case of perpendicular polarization. The perpendicular field will induce charges in the carbon nanotube walls, in this case the nanotube will behave as a Faraday cage and tend to cancel the external field. Thus, only the parallel polarization field will considered [32, 33]. For a mixture of semiconducting and metallic tubes, the allowed optical transitions, starting from the lowest energy, will appear according to the following order: S_{11}, S_{22}, M_{11}, S_{33}, S_{44}, M_{22},.. . The band labeled S_{ii} and M_{ii} correspond to the *ith* optical transitions in the semiconduction and metallic tubes, respectively. Figure 2.14 shows the absorbance spectrum of a free-standing SWCNTs. It consists of several pronounced absorption bands on top of a broad background, which is due to the $\pi - \pi^*$ absorption centered at around 5 eV [34]. The inset shows the absorbance spectrum after the background subtraction.

Using the linear k approximation for the isolated SWCNT, one can observe that the energy difference between the symmetrical singularities in the valence and conduction bands occur at $S_{22} = 2S_{11}$ and $S_{33} = 4S_{11}$, corresponding to a 1, 2, 4 pattern of vHS from the Fermi energy and for metallic nanotubes $M_{22} = 2M_{11}$ and $M_{33} = 3M_{11}$, corresponding to a 1, 2, 3 pattern of vHS from the Fermi energy. In this picture, the what is called trigonal warping effect is neglected [25].

2.3.2.1 Trigonal warping effect

For small diameters SWCNTs, the value of $\mid K_1 \mid = 2/d_t$ is large, and the linear dispersion relation is no longer valid. By plotting the energy contour lines near

2. Trigonal warping effect

the K points [see Figure 2.4 (d)], the energy contour for small k values near to the K and K' points is circular. For larger k values, the equi-energy contours become a triangle, connecting the three M points. The distortion of the equi-energy contours away from the circular shape is known as the trigonal warping effect. This means that the energy minima position depends on the nanotube chirality [31, 32]. Due to the trigonal symmetry of the Brillouin zone, the bands on the right side of the of the K point have energies higher than those lying on the left side of the K point at the same distance. This asymmetry increases with increasing the wrapping angle, $\phi = 30° - \theta$, from the armchair direction [see Figure 2.5 (a)] [35]. The trigonal warping effect splits the vHS peaks in smaller metallic nanotubes ($d < 2\ nm$), the splitting is maximum for zigzag metallic tubes and zero for the armchair metallic tubes [see Figure 2.15 (I)]. The splitting of the lines in the metallic nanotubes comes from the two neighbouring lines near the K point [see Figure 2.16]. In the case of armchair tubes, the two lines [red bold lines in Figure 2.16 (a)] are equivalent to each other and the DOS peak energies are equal to each other as shown in Figure 2.15 II(b), while for the zigzag nanotubes, the two line [red and violet bold lines in Figure 2.16 (b)] are not equivalent, giving rise to the DOS peak splitting as shown in Figure 2.15 II(c) [31, 32]. The splitting of the first vHs in the metallic nanotubes can be written as [25]:

$$\Delta E_{11} = \frac{6\gamma_o a_{C-C}^2 \cos(3\theta)}{d^2} \tag{2.25}$$

In the case of semicouncting nanotubes, the K and K' points are related to each other by the time reversal symmetry (they are at the oppsite corners of the BZ), and the chiraltiy in invariant under the time reversal operation. So, the k values near the K point will contribute to different spectra, namely S_{11} and S_{22} as shown in Figure 2.15 II(a) [32]. The trigonal warping effect causes the absolute energy of vHS in the case of semiconducting nanotubes to shift by an extent depending on the nanotube chiral angle [32].

In 1999 Kataura *et al.* [37] have published a plot of the calculated E_{ii} for the SWCNTs with different chiralities as a function of their diameters. Figure 2.17 is a re-plot of Kataura plot using $\gamma_o = -2.9\ eV$ which yields better agreement with the measured E_{ii}. Here, each solid black circle corresponds to different
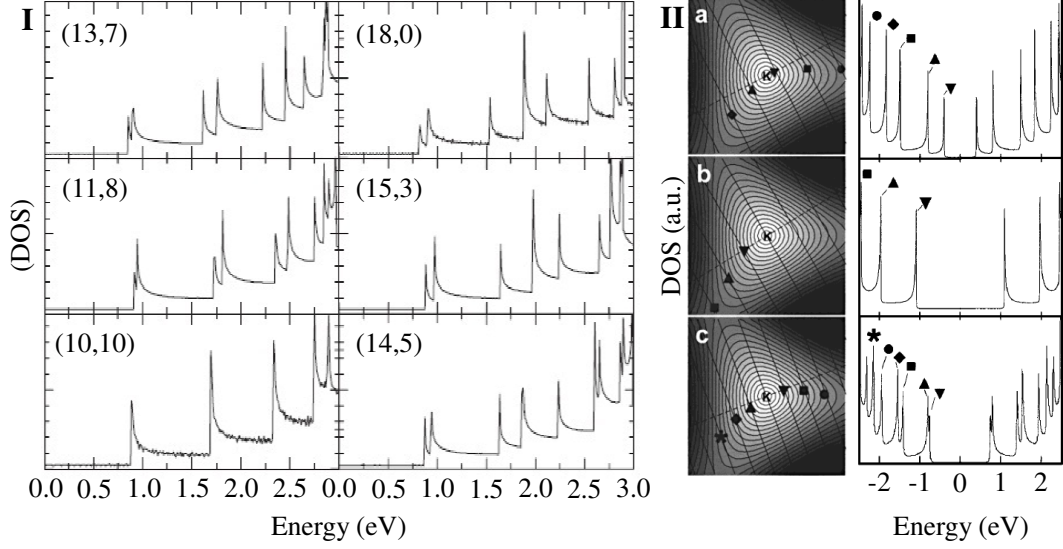
Figure 2.15: (I) The DOS vs energy for several metallic nanotubes of approximately the same diameter with different chirality, showing the trigonal warping effect on the vHS of: (10,10) (armchair), (11,8), (13,7), (14,5), (15,3) and (18,0) (zigzag) [32]. (II) Zone-folding energy dispersion relation relation of the π-band in the (a) (7,6) semiconduction tube, (b) (7,7) armchair metallic tube, and (c) (13,7) chiral metallic tube. Symbols mark the positions of the vHS in the bands [36].

semiconducting SWCNT and each open red circle corresponds to different metallic SWCNT. It is shown in Figure 2.17 that for the armchair SWCNTs, M_{22} is less than $2M_{11}$ and for the zigzag SWCNTs, S_{22} is not equal to $2S_{11}$. In the case of zigzag SWCNTs both S_{11} and S_{22} are coming from two different symmetry lines $\Gamma-K$ and $\Gamma-M$, respectively. This is an important aspect of the trigonal warping effect [31, 32]. Also from Figure 2.17, one can observe that the width of $E_{ii}(d)$ increase with increasing energy and i and decreasing the nanotubes diameters.

2.3.2.2 Effect of Curvature

Within the zone-folding scheme of carbon nanotubes, the fact that all the carbon atoms are placed on the cylindrical wall was ignored. It has been proven that, the zone folding scheme of the nearest-neighbour tight binding graphene gives a reliable electronic energies for the carbon nanotubes exceeding 1.2 nm. Due to the curvature effect, the length of the C-C bonds perpendicular to the tube

2. Effect of Curvature
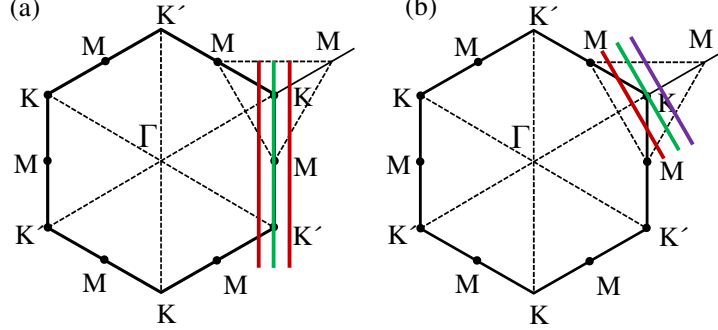
Figure 2.16: The trigonal warping effect of the van Hove singularities. The three bold lines near the K point are possible k vectors in the hexagonal Brillouin zone for metallic (a) armchair and (b) zigzag carbon nanotubes. The minimum energy along the neighboring two lines gives the energy positions of the vHS [31].
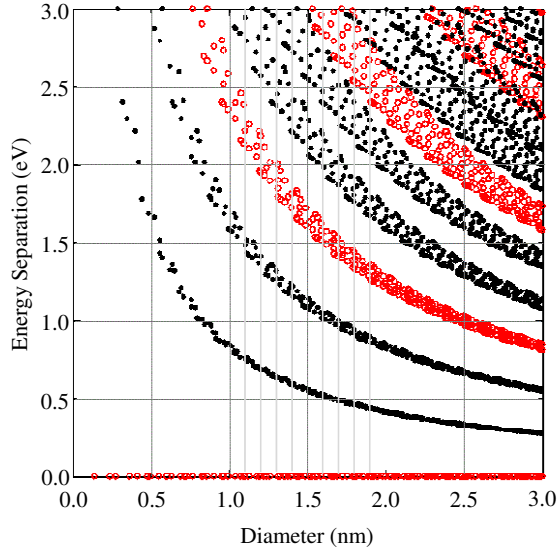
Figure 2.17: Energy separations E_{ii} for all (n,m) values as a function of nanotube diameter between 0.7 and 3.0 nm [based on the work of Kataura et al. Ref. [37]]. The results are based on the TBM, with $\gamma_o = -2.9\ eV$ and $s = 0$. The crosses and open circles denote the peaks of semiconducting and metallic nanotubes, respectively. The points for zero gap metallic nanotubes along the abscissa [38].

axis is slightly different from those parallel to the tubes axis. Thus, the two p_z orbitals are not exactly perpendicular to the nanotube surface and a finite angle relative to the normal direction to the tubes' surface will form. It has been proven that, the three σ-bonds are not in the same plane but directed towards the nearest neighbour carbon atom, i.e., they are tilted by a small angle relative to the tangential $\vec{C}$ direction. Thus, a rehybridization between the σ and π bonds is expected [39–41]. It has been found that, due to the curvature effect a small

gap opens at the Fermi energy in all metallic nanotubes except for the highly symmetric metallic armchair nanotubes. The induced gap in the non-armchair metallic tubes is given by [25, 39]

$$E_{gap} = \frac{3\gamma_o a_{C-C}^2 \cos 3\theta}{4d^2} \qquad (2.26)$$

The induced gap easily exceeds the thermal energy at room temperature, its value is around 80 meV for (9,0) SWCNT. Thus, all the $(n - m) = 3l$ SWCNTs are considered as metallic at room temperature [25]. In the case of SWCNTs with diameters less than 1 nm, the rehybridization between the orbitals leads to mixing between the anti-bonding bands σ^* and π^*, causing drastic changes in the electronic band structure. For example, mixing of σ^* and π^* orbitals in (5,0), (3,3), (4,0), and (4,2) semiconducting lowers the nanotubes π^* band to such an extent that it crosses the Fermi energy. Thus, a metallic behaviour is expected in this case [42–44].

2.3.3 Raman Spectroscopy

Raman spectroscopy is a powerful technique to characterize synthesis, purification, and physical properties of carbon nanotubes [45]. Different laser excitation energies can demonstrate different vibrational modes of the carbon nanotubes [46]. Also, Raman spectroscopy can differentiate between metallic and semiconducting nanotubes [47]. It has been established that resonance Raman spectroscopy can used to characterize carbon nanotubes at the single tube level, where SWCNTs have been deposited on silver or SiO_2 substrate [48, 49].

2.3.3.1 Phonon Structure of SWCNTs

The zone folding scheme gives a good insight into the phonon structure in SWCNTs. Since the 2D graphene sheet has two atoms per unit cell, thus six phonon modes are expected because of the three degree of freedom per each carbon atom [24, 45], as shown in Figure 2.18 (a) and (b).

In the zone-folding scheme, by superimposing the N cutting lines in the K_2-extended representation on the six phonon modes, $6N$ phonon modes for each
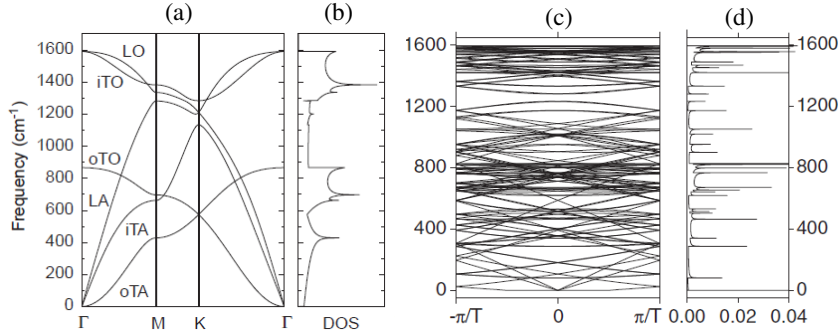
Figure 2.18: (a) Phonon dispersion of 2D graphite sheet. The phonon are labeled: out-of-plane transverse acoustic (oTA); in-plane transverse acoustic (iTA); longitudinal acoustic (LA); out-of-plane transverse optic (oTO); in-plane transverse optic (iTO); longitudinal optic (LO). (b) The phonon density of states for a 2D graphene sheet. (c) Phonon modes for the (4, 2) nanotube obtained by zone-folding. (d) Density of states for the phonon modes shown in (c). [10, 24]

carbon nanotube will obtained. From the cutting lines, $6(\frac{N}{2} - 1)$ pairs of phonon modes will arise with indices μ and $-\mu$. The $\mu = 1, ..., (\frac{N}{2} - 1)$ modes are doubly degenerate, while the phonon modes from $\mu = 0$ and $\mu = N/2$ are non-degenerate, so the total number of phonon modes will be $6(\frac{N}{2} - 1 + 2)$ or simply $3(N + 2)$. For example, in the case of (4,2) SWCNT, the number cutting lines is 28 [as discussed under section 2.3], so the total number of phonon modes will be 90, as shown in Figure 2.18 (c) and (d). In the density phonon states of SWCNTs, large number of spikes appear similar to the vHS appearing in the nanotubes DOS. Among the large number of phonons, only ~ 16 are Raman active modes and ~ 7-9 are IR active modes [21, 24, 45]. The phonons at $\mu = 0$ are belonging to the symmetric irreducible representation A and the phonons at $\mu \geqslant 1$ are belonging to the symmetric irreducible representation E, which are related to the harmonic wave along circumference of the nanotube [45].

The zone folding scheme gives non-accurate results for the lower frequency phonon modes (acoustic modes), while it gives reliable results for the higher frequency modes (optical modes). This is because the zone folding scheme neglects the curvature of the nanotube walls. This limitation for the low frequency phonon modes was solved by using the force constant model [45]. For more details about

2. Phonon Structure of SWCNTs
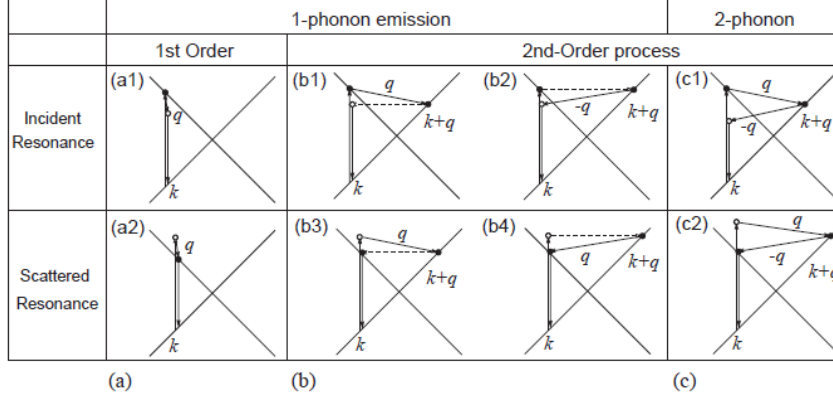
Figure 2.19: (a) First-order and (b) one-phonon second-order, (c) two-phonon second-order, resonance Raman processes. (top) incident photon resonance and (bottom) scattered photon resonance conditions. For one-phonon, second-order transitions, one of the two scattering events is an elastic scattering event (dashed lines). Resonance points are shown as solid circles [46].

the SWCNTs phonons dispersions see Ref. [50].

In general Raman scattering is an inelastic scattering of light. The scattering events can be summarized as follows: (1) excitation of an electron from the valence band to the conduction band by photon absorption, (2) the excited electron is scattered by emitting (or absorbing) phonons, and (3) relaxation of the electron from the valence band to the conduction band by emitting a photon. The number of emitted phonons before lattice relaxation can be one, two, and so on. The number of the total scattering events defines the order of Raman scattering. First order scattering involves only one phonon emission [as shown in Figure 2.19 (a)]. The case of two-phonon scattering events or one-phonon and one elastic scattering is called second-order Raman scattering [as shown in Figure 2.19 (b) and (c)] [24]. Four characteristics Raman modes are known: the radial breathing mode (RBM) around 180 cm^{-1}, the defect line (D-mode) around 1350 cm^{-1}, the graphite mode (G-mode) around 1580 cm^{-1} and the overtone of the G-mode (G'-mode) at around 2700 cm^{-1} [51] [see Figure 2.20]. The so-called RBM and G-mode are first-order Raman scattering process, where the D-mode and G'-mode are second-order Raman scattering process [24].
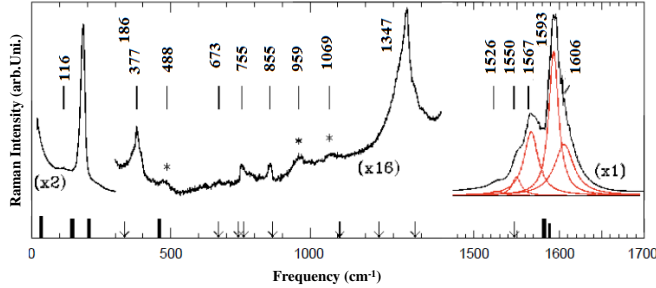
Figure 2.20: Raman spectrum of SWNT samples taken with 514.5 nm excitation. The ($*$) in the spectrum indicates features that are tentatively assigned to second-order Raman scattering [24].

2.3.3.2 The Radial Breathing Mode

The RBM is considered as a first-order Raman scattering process, where all the carbon atoms move coherently in a radial direction (totally symmetric A mode) [see Figure 2.21 (a)]. The RBM is a unique carbon nanotubes mode. The RBM is inversely proportional to the nanotubes diameter. From the theoretical calculations, the diameter of the tubes d is related to the frequency ω_r with the relation:

$$d = C + \frac{A}{\omega_r} \tag{2.27}$$

where A is a constant. The value of A is ranged from 218 to 236 depending the calculation method [46, 52–55]. If the small effect of the tube-tube interaction neglected and the mean value of A from the theoretical calculations cited above is calculated, the value of A would be 234 [56]. If the small effect of the van-der-Waals intertube interactions is neglected i.e., setting C=0, in this case the uncertainty in the diameter calculations would be around 5% [56]. This relation is valid in the case of nanotubes with diameters $1 < d_t < 2$ nm. In the case of nanotubes with diameters $d_t < 1$ nm, the simple relation given in equation 2.27 is not valid due to the nanotubes lattice distortion leading to chirality dependence of ω_r. For nanotubes with $d_t > 2$ nm, the RBM intensity is weak, due to the weaker quantum confinement [45].

2.3.3.3 The G-Mode

The G-mode is also a first-order Raman scattering process and used to characterize SWCNTs, where carbon atoms vibrate along the axis or the circumference

Figure 2.21: (a) RBM and (b) G-mode for a (10,10) nanotube. The red arrows indicate the magnitude and direction of the appropriate C-atom displacements, and the eigenvectors. The unit cell (blue atoms) is shown schematically in the lower right-hand corner [46].

of the nanotube [see Figure 2.21 (b)]. The G-mode is diameter dependent, but it is less accurate compared the RBM. In graphite, this mode is related to the tan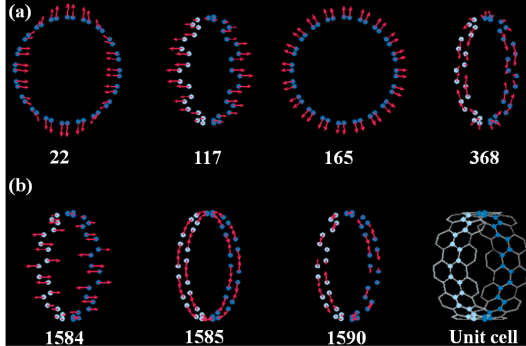gential E_{2g} Raman active mode, where the two carbon atoms in each unit cell are vibrating tangentially. In the case of SWCNTs, due to the quantum confinement of the phonon wave vector along the circumference, this mode will split to six Raman-active modes [two of each modes with $A(A_{1g})$, $E_1(E_{1g})$, and $E_2(E_{2g})$]. E_1 and E_2 modes come from the zone folding of the phonons away from the Γ point, so they have different frequencies. On the other hand, A modes are associated with the Γ point, therefore no splitting is expected. However, due to the nanotube curvature, the force constant along the nanotube circumference will be lower than that along the nanotube axis, so two different A modes are observed for the semiconducting nanotubes at 1592 cm^{-1} for the longitudinal mode and at 1569 cm^{-1} for the transverse mode [57]. The six-G-modes can be divided into two groups (1) the upper frequency modes or G$^+$, where all the carbon atoms vibrate along the nanotube axis (longitudinal phonon mode). The G$^+$ modes are diameter independent. (2) the lower frequency modes or G$^-$, where all the carbon atoms vibrate along the nanotube circumference (transverse phonon mode). The G$^-$ are diameter dependent, where the frequency decreases with decreasing the diameter [45]. Experimental Raman results of SWCNTs showed that the shape of G$^+$ and G$^-$ is dependent on wether the nanotube is semiconducting or metallic. In the case of semiconducting SWCNTs, both G$^+$ and G$^-$ components have a Lorentzian line shape with 6-15 cm^{-1} full width at half maximum (FWHM). For the metallic SWCNTs, the G$^+$ component has a Lorentzian line shape but the G$^-$ component has asymmetric line shape and can be fitted with Breit-Wigner-Fano

(BWF) line shape [24, 25, 45]. The origin of BWF line is due to the coupling between the TO phonons vibrations and the conduction electrons of the primary metallic tubes [58]. The BWF can be described by the following function

$$BWF(\omega) = I_o \frac{(1 + (\omega - \omega_o)/q\Gamma)^2}{1 + ((\omega - \omega_o)/\Gamma)^2}, \tag{2.28}$$

where ω_o is the peak position at maximum intensity I_o and Γ is the FWHM of the Lorentzian line shape. $1/q$ represents the asymmetry of the line shape and measures the interaction strength between the phonon and the conduction electrons. when the $1/q \to 0$ the BWF function becomes Lorentzian.

2.3.3.4 The D and G'-Modes

With the presence of defects in SWCNTs, second-order Raman scattering is expected. Where the electron: (1) absorbs a photon at the k state, (2) scatters to $(k + q)$ state, (3) scatters back to the state k, and finally (4) emits a photon by renomination with a hole at the k state. The scattering of the electron from $(k + q)$ to k state, can be either by:

- elastic scattering with a crystal defect followed by an elastic scattering by emitting a phonon [as show in Figure 2.19 (b_1 to b_4)] or

- by two-inelastic scattering events, by giving two phonons with the same q value but travelling in opposite direction [see Figure 2.19 (c_1 and c_2)]

The first probability gives the D-band Raman feature in SWCNTs and the second one gives the G'-band which seen as an over tone of the D-band [24]. The D-band is the most studied disordered-induced feature in SWCNTs. It occurs in the range 1250-1450 cm^{-1} and shows a dispersive behaviour with the laser energy, i.e., the frequency increases with increasing the laser excitation energy, where 63 cm^{-1}/eV shift was observed [59]. Also, the D-band shows a dependence on the nanotube diameter, it increases with increasing the diameter according to the following relation

$$\omega_D = 1354.8 \ cm^{-1} - C_D/d_t \tag{2.29}$$

where the constant C_D was found to be 16.5 cm^{-1} nm. This value is valid for various semiconducting as well as metallic nanotubes [45, 60, 61].

The so called G'-band is very informative for the SWCNTs vibrations and electronic structure. This band is called the overtone of the D-band and appears at around 2700 cm^{-1} and exhibiting a strong frequency dispersive as the laser energy varied ($\sim$ 106 cm^{-1}/eV). The G'-band depends on the nanotube chirality, giving details information about the electronic vHS. For metallic SWCNTs, the splitting of vHS for different chiral nanotubes was observed [45, 61, 62].

2.4   Structure of Peapods

It has been demonstrated that, due to the tubular structure of the SWCNTs, it can encapsulate various atoms, molecules or inner wall. The filled SWCNTs with a linear chain of fullerene molecules are known as peapods and those filled with inner wall are known as double-walled carbon nanotubes (DWCNTs). The electronic, transport, and mechanical properties of the filled nanotubes are modified upon filling. So, it is possible to fine-tune the nanotubes properties by changing the filler [63].

Filling of SWCNT with fullerene molecules is exothermic or endothermic process depending on the nanotube diameter. It has been proven that filling of (10, 10) metallic SWCNTs with C_{60} fullerene molecules is exothermic process and the resulting C_{60}@(10, 10) peapods are stable. On the other hand, the C_{60}@(9,9) and C_{60}@(8,8) peapods resulting from filling smaller (9,9) and (8,8) metallic nanotubes are not stable systems. The filling process can be discussed in terms of stabilization energy ΔE_S as follows

$$\Delta E_s \equiv E\left[xC_{60}@(n,m) - (n,m)\right] - x\left[C_{60}\right], \tag{2.30}$$

where x is the number of C_{60} molecules. Figure 2.22 shows the stabilization energy ΔE_S as a function of nanotube diameters. One can observe that as the nanotubes diameter decreases the interaction between the C_{60} molecules and nanotube walls becomes significant. The $xC_{60}@(10, 10)$ peapods is the most stable peapods system, where the π-electrons clouds of both nanotubes and C_{60}

30
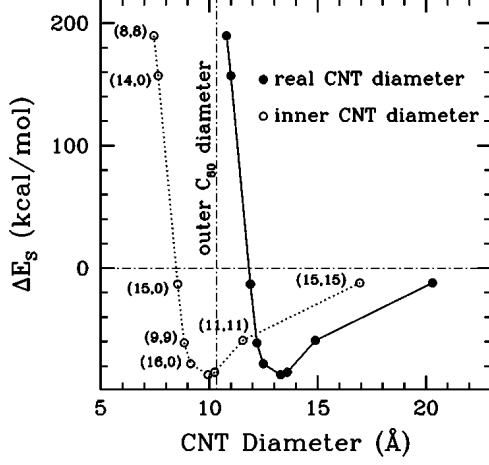
Figure 2.22: Stabilization energy ΔE_S for the introduction of a C_{60} molecule into SWC-NTs with different diameters. Exothermic peapods have negative ΔE_S and endothermic peapods have positive values [67].
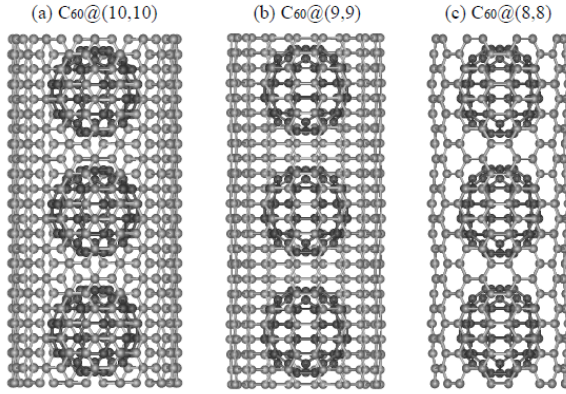
Figure 2.23: Total-energy optimized geometries of of different C_{60}-peapods (a) C_{60}@(10,10), (b) C_{60}@(9,9), and (c) C_{60}@(8,8)-peapods. Distances between C_{60} molecules are 3.14, 3.15, and 2.45 Å, for C_{60}@(10,10), C_{60}@(9,9), and C_{60}@(8,8)-peapods, respectively [65].

molecules can overlap. Also, it is clear from Figure 2.22 that the nanotube diameters in the range from 1.2 to1.4 nm are the most suitable diameters for the C_{60} molecules encapsulation. This is in a good agreement with experimental results [64] and theoretical calculations [65, 66]. As the nanotube diameters decreases, a large structural deformation and consequently lower stability is expected [67], as shown in Figure 2.23. In the case of C_{60}@(10,10)-peapods, the C_{60} molecules inside the nanotube cavity keep their original spherical shape, with 3.31 Å between the fullerene molecules and the nanotubes wall. On the other hand, the fullerene molecules in the case of C_{60}@(9,9) and C_{60}@(8,8)-peapods are distorted and elongated along the nanotubes.

Figure 2.24 (a) shows the energy bands for the (10,10) SWCNT and C_{60}@(10,10) peapods. In the case of C_{60}@(10,10) peapods, four bands cross the Fermi-level:
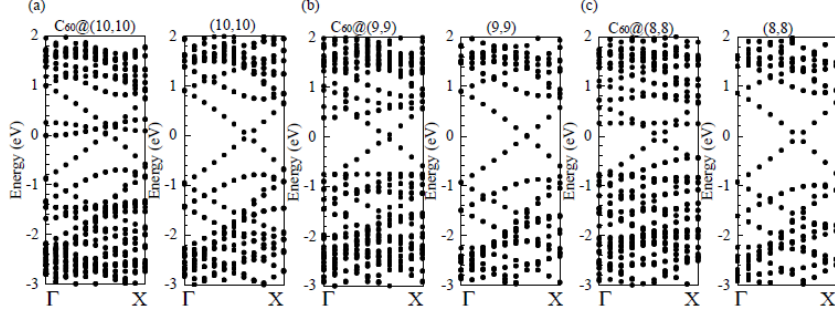
Figure 2.24: Energy band structures of encapsulated $C_{60}@(n,n)$ and of isolated (n,n) nanotube. (a) n=10, (b) n=9, and (c) n=8. Energies are measured from the Fermi level energy ϵ_F [65].

two of them have the linear dispersion of the nanotubes π-orbitals and the other two are similar to the C_{60} π-state (t_{1u}) state. This means that, the $C_{60}@(10,10)$ peapods is metal with different characters of multi-carriers. The differences between the $C_{60}@(10,10)$, $C_{60}@(9,9)$, and $C_{60}@(8,8)$ peapods are shown in Figure 2.24 (b) and (c). The differences could be attributed to the available space between the nanotube wall and the C_{60} molecules [65, 66]. Figure 2.25 (a) shows the electron charge distribution of the $C_{60}@(10,10)$ peapods. In this case, the free space between the nanotube wall and the C_{60} molecules is enough to allow the transfer of electrons from the nanotubes π-orbitals to the free space between the nanotubes and the C_{60} molecules, forming what is called nearly free electron (NFE) state. Thus a hybridization between the NFE and π and σ orbitals of the C_{60} is expected. As a result of this hybridization, the C_{60} π-orbitals will shift downward as shown in Figure 2.24 (a). In the case of $C_{60}@(9,9)$ and $C_{60}@(8,8)$-peapods [Figure 2.24 (b) and (c)], the charge distribution is quite different because the free space between the SWCNTs wall and the C_{60} molecules is not enough to create the NFE state at a couple of eV near Fermi level. Probably, the NFE is above the vacuum level [65, 66].
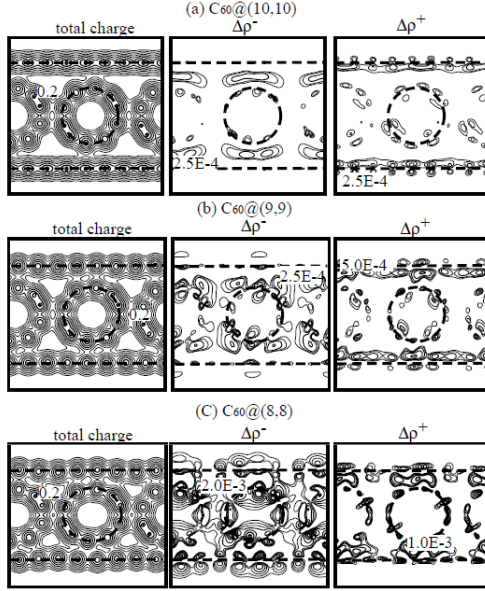
Figure 2.25: Contour plots of the total valence charge density of $C_{60}@(n,n)$. (a) n=10, (b) n=9, and (c) n=8. The contour plot of more negatively charged (electron rich) area, $\Delta\rho^-$, and that of the more positively charged, $\Delta\rho^+$. The values shown in figures are in units of $e/(a.u.)^3$ [65].

2.5 Double-walled Carbon Nanotubes

DWCNTs are considered as the simplest form of multi-walled carbon nanotubes (MWCNTs). DWCNTs form a special class of nanotube, they exhibit the morphology and the physical properties of SWCNTs and the chemical properties of MWCNTs. The small diameters of the inner wall facilitate the study of the physical properties of high curvature carbon nanotubes [68]. Two main routes are used to prepare DWCNTs: chemical vapour deposition (CVD) and peapods method. The peapods method is perfect to prepare relatively pure DWCNTs with well defined and controlled diameters. Fullerene molecules encapsulated inside the SWCNTs, can be transformed into inner tubes inside after high-temperature heat treatment in vacuum or in inert gases [69–71]. But the peapods method has one disadvantage compared to the CVD method: The formed inner tubes are short and a multiple interatube junctions between them are expected. In this case, the SWCNTs are considered to be inhomogeneously filled and contain many defects, leading to lower mechanical support from the inner tube to the outer one. In case of CVD grown DWCNTs, the inner and the outer tubes were grown simultaneously. Therefore, the mechanical coupling between them is satisfied [72].

2. Double-walled Carbon Nanotubes

The polymerization of fullerene molecules is known to be very slow at $800°$C and needs days to complete [73]. But it gives useful information about the intermediates structures formed by polymerized fullerenes. The time of polymerization can be reduced to hours by increasing the temperature to $1200°$C [69, 70]. The mechanism of the inner wall formation by the polymerization of fullerene molecules has been discussed by several authors [74–76]. The mechanism can be briefly explained as follows: carbon atoms in fullerenes are made of sp^2 bonds which are strong and decomposes at $\sim 4000°$C. However, fullerenes molecules were observed to start combine together at relatively low temperature $\sim 800°$C. The strong sp^2 bonds do not break but they combine by bonds rearrangement rotation, what is called Stone-Wales transformation [74–76]. This process is started by the (2+2) cycloaddition reaction, shown as in Figure 2.26 (step 1→2). At low temperature, polygons rather than double bond face each other in adjacent fullerenes, preventing the fusion between the adjacent molecules. At sufficient high temperature $\sim 800°$C, the fullerene molecules rotation is activated and hence the probability of double bonds facing each other increases [75]. When the cycloaddition process accomplished the generalized Stone-Wales (GSW) transformation starts. The fusion of two C_{60} to a C_{120} capsule is driven by the energy gain associated with reducing the local curvature in the system. Close inspection of the fusion reaction energy along the path showed in Figure 2.26 indicates a sequence of 23 activated processes connecting the 24 metastable states. The activation energy barriers of these GSW transformations is ≈ 5 eV but the energy released during the fusion process is sufficient to heat up the structure locally and thus further promoting activated processes of the fusion [75]. Therefore, the bond rotations turn out to be multistep processes with lower individual activation barriers. According to Han's optimum pathway, there are 24 steps of transformation [75] but there are 200 steps according to Ding's model [74].

Owning to the fullerene fusion process, the first formed tubes have diameters close to the diameter of fullerene molecules ≈ 0.71 nm [77]. After long time of heat treatment, the diameter of the first tubes will increase by what is called tube fatting process, explained by Ding [74]. As shown in Figure 2.27, firstly, a bond rotation on the nanotube surface turns four hexagons into a 7|5|5|7 structure. Figure 2.27 can be viewed as an edge dislocation in a 2D hexagonal lattice.
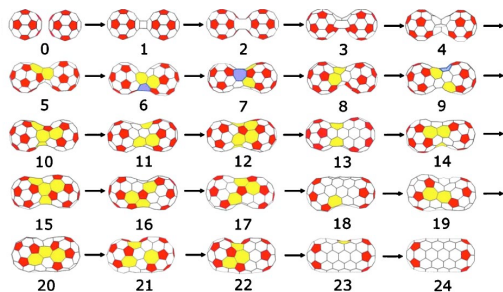
Figure 2.26: (a) Optimum pathway for the $2C_{60}$ to C_{120} fusion reaction, involving the Stone-Wales bond rotations. Polygons other than hexagons are emphasized by color and shading. [75].
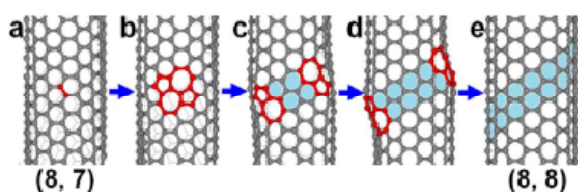
Figure 2.27: Mechanism of tube fattening. Step a→b, a C-C bond rotation creates an SW defects in the nanotube. Steps b→e, continuous separation of the two 5|7 turns on the original (8,7) tube into a fatter (8,8) armchair tube. [74].

This edge dislocation movement transforms the original small diameter tube into another with larger diameter, for example from (8,7) into (8,8) nanotube as shown in step b→e in Figure 2.27.

2.6 Carbon Nanotubes under Pressure

An efficient approach towards understanding the properties of carbon nanotubes under high pressure is to study the effect of hydrostatic pressure on the structural properties of nanotubes.

The structure deformation of crystalline bundles of (6,6), (8,8), and (10,10) SWCNTs under pressure has been demonstrated by Chan *et al*. [78] using density functional theory (DFT). The unit cell volume of the nanotube was taken as the reduced volume (RV). In the case of (10,10) SWCNTs, at pressure equal to zero, the tubes cross-section is circular and RV = 1.0 as shown in Figure 2.28(a). As applied pressure increases the unit volume decreases stepwise from VR = 1.0 to VR = 0.89 at about 2.7 GPa and a structural transition from the circular to the oval shape is expected [see Figure 2.28(b)]. At this point, with further pressure increasing, the intertube van de Waals interactions become a serious disadvantage in terms of energy. To reduce such interactions (repulsion interactions), the tubes must deformed to more flexible and compressible structure. Therefore, with
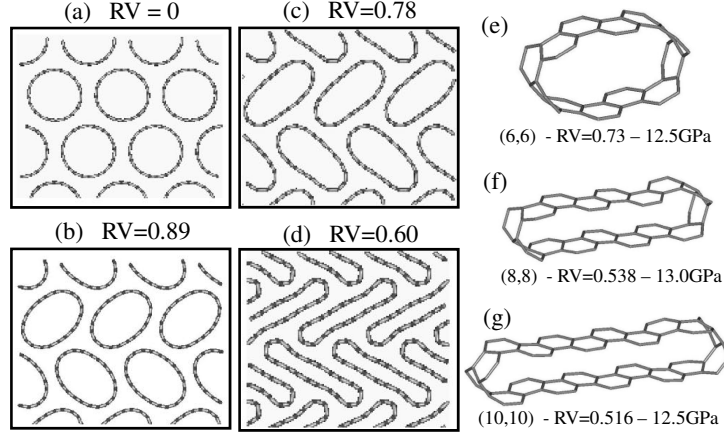
Figure 2.28: (a)-(d) show the proposed structure deformation of (10,10) SWCNTs under pressure. The unit cell volume is taken as the reduced volume (RV). The flattened tube deformation in bundles of (e) (6,6), (f)(8,8), and (g)(10,10) tubes at a lattice stress around 13 GPa. The structures of (8,8) and (10,10) tubes are similar to each other, with longer flat sections for the (10,10) tubes. The distance between the two flat graphene sections is around 3.8 Å for both the (8,8) and (10,10) structures at such high pressure, approaching the interlayer distance of 3.35 Å in graphite. The (6,6) structure is somewhat elliptical, due to its small diameter [78].

increasing the pressure after RV = 0.89, the SWCNTs will more ovalized to the structure in Figure 2.28(c) with RV = 0.78. Upon further compression, a more flattened shape [Figure 2.28(d)] is expected with RV = 0.6.

The mechanical stability of the SWCNTs by filling the tubes with molecules or with inner tubes is an important issue. High-pressure Raman measurements, which monitors the vibrational properties, showed that the filling with inner tubes or argon molecules stabilizes the outer tubes and this kind of filling considered as a case of homogenous filling [79–87]. In contrary, filling with C_{70} or iodine molecules, a case of inhomogeneous filling, leads to destabilization of the nanotubes [79, 80, 83, 88, 89].

The deformation of SWCNTs filled with argon molecules under pressure has been investigated using classical molecular dynamics simulations by Shanavas *et al.* [87]. Figure 2.29 (I) shows the pressure-volume behaviour of the SWCNTs filled with argon atoms with different densities. The argon atoms densities inside the SWCNTs are varying from 0 to 70 atoms/tube. One can observe that, the nanotube volume decreases discontinuously at some pressures, depending on
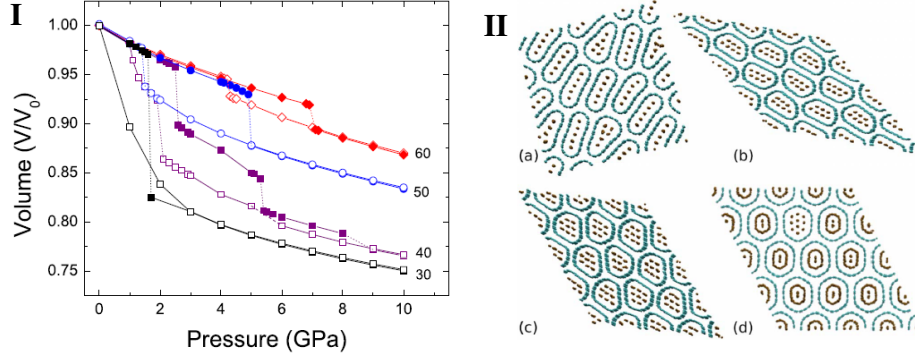
Figure 2.29: (I) Pressure-volume behavior of SWCNTs filled with 30, 40, 50, and 60 argon atoms/tube. Closed symbols represent compression and open symbols denote results of the pressure release. (II) High-pressure phases of SWCNTs filled with (a) 40, (b) 50, (c) 60, and (d) 70 atoms/tube at 10 GPa [87].

the argon atoms density, In the case of 40 atoms/tube, as an example, multiple volume drops at 2.5, 5.4, and 8.5 GPa. As the argon atoms density increases the change of the tube volume at the transition pressure become smaller. At the higher density, 70 atoms/tube, the volume change looks gradual rather than abrupt. Shanavas *et al.* [87] explained this behaviour as follows: when argon density is low, the average distance between argon atoms will be large and the van der Waals forces between the tube wall and the argon atoms will be attractive. Therefore, at low argon density, the attractive forces between the tube wall and the argon atoms will be added to the external applied pressure leading to rapid collapse. On the other hand, as the argon density increases $\geqslant 60$ atoms/tube, the interactions between the argon atoms and the SWCNT wall will be repulsive, thus leading to stabilization of the tubes against the applied pressure. Figure 2.29 (II) shows the high pressure phases of SWCNTs filled with different argon densities (a) 40, (b) 50, (c) 60, and (d)70 atoms/tube at 10 GPa. At low argon density ~ 40 atoms/tube, the collapsed tubes looks flat similar to those of empty tubes. At around 70 atoms/tube, the nanotube changed to two deformed hexagons signals a support from the inner argon atoms. This case is similar to the effect of filling the tubes with inner tube [87].

In the case of DWCNTs, it has been demonstrated that the inner tube sup-
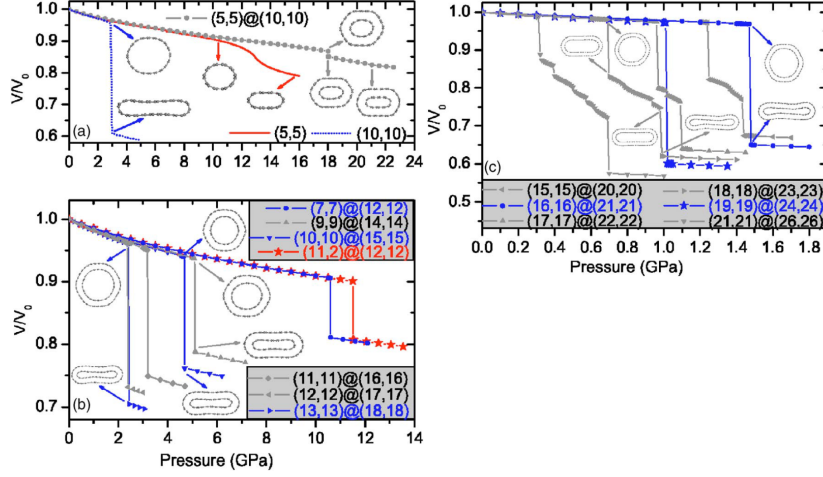
Figure 2.30: Loading curves for different armchair-armchair DWCNTs bundles as a function of hydrostatic pressure. (a) Small-diameter (5,5), (10,10) DWCNTs bundle, (b) some intermediate-diameter DWCNT bundles, and (c) the larger-diameter DWCNT bundles. [84].

ports the outer one [80, 83–86]. Yang et al. [84], proposed the structural change of DWCNTs bundles under hydrostatic pressure. The results are represented in Figure 2.30. For small diameter (5,5)@(10,10) DWCNTs bundles, shown in 2.30 (a), a small discontinues volume change at $\sim$ 18 GPa was observed followed by a cross-section deformation to two deformed hexagones. In this case the (5,5) SWCNT inner tube increases the ability of the outer (10,10) SWCNT to resist the external applied pressure up to $\sim$ 18 GPa. For intermediate DWCNTs bundles shown in Figure 2.30(b), all the tubes go through one structural phase transition and after that collapse completely. For example, the (10,10)@(15,15) DWCNT collapses at $\sim$ 4.68 GPa. This value is higher than the collapse pressure either that of (10,10) SWCNT ($\sim$ 3 GPa) or that (15,15) SWCNT ($\sim$ 1.3 GPa). In the case of larger tube diameters, the collapse behaviour is quite complex as shown in Figure 2.30(c). The (16,16)@(21,21) and (19,19)@(24,24) DWCNTs collapse after only one structural phase transition. On the other hand, (15,15)@(20,20), (17,17)@(22,22), (18,18)@(23,23), and (21,21)@(26,26) undergo two different structural phase transitions.

Chapter 3

Experimental Techniques

Optical spectra of carbon nanotube films were measured at room temperature using a Bruker IFS 66v/S Fourier transform infrared spectrometer in combination with an infrared microscope (Bruker IR Scope II) with a 15× Cassegrain objective. The IR microscope enables the measurements of optical properties under high pressure for micrometer size samples. In general, optical spectroscopy is a powerful technique to characterize the electronic band structure of SWCNTs under pressure in terms of the energy position and spectral weight of the excited interband and intraband transitions since the electronic band structure of SWCNTs is very sensitive to pressure. In this chapter, the theory of the infrared spectroscopy at high pressure is explained. A brief description of all aspects of the high-pressure measurements is also presented.

3.1 Introduction to infrared spectroscopy

3.1.1 Principle of Fourier transform

Michelson interferometer is very important optical instrument. It has been invented by the American physicist A. A. Michelson (1852-1931) [90]. The basic principle of Michelson interferometer is to split a light beam into two parts and then recombines them again to form an interferogram pattern. A diagram of Michelson interferometer is shown in Figure 3.1. The interferometer consists of two perpendicular mirrors, one of them is movable and the other is fixed. A
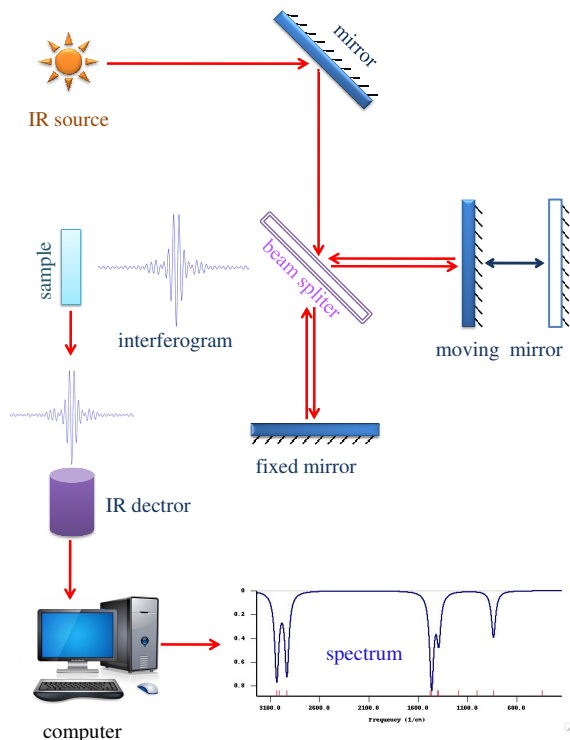
Figure 3.1: Scheme of Michelson interferometer.

semi-reflecting film, called the beam splitter, bisects the planes of the two mirrors. When a light beam strikes the beam splitter, 50% of the incident beam will reflected to one of the mirrors and 50% will transmitted through the beam splitter to the second one. The two beams reflected again from the mirrors to the beam splitter where they can recombine and interfere. If the fixed and the moving mirrors are at the same distance from the beam splitter the two beams will travel the same distance, thus the optical path difference between them will be zero. An optical path difference is obtained by translating the movable mirror away from the beam splitter. For path difference of $(n + 1/2)\lambda$, the two beams will interfere destructively and constructively for path difference of $n\lambda$. For a monochromatic radiation [see Figure3.2 (a)] the resultant interference pattern is simple and can be described by cosine function as follows [91, 92]

$$I_{(\delta)} = B_{(\nu)} \cos(2\pi\delta\nu) \tag{3.1}$$
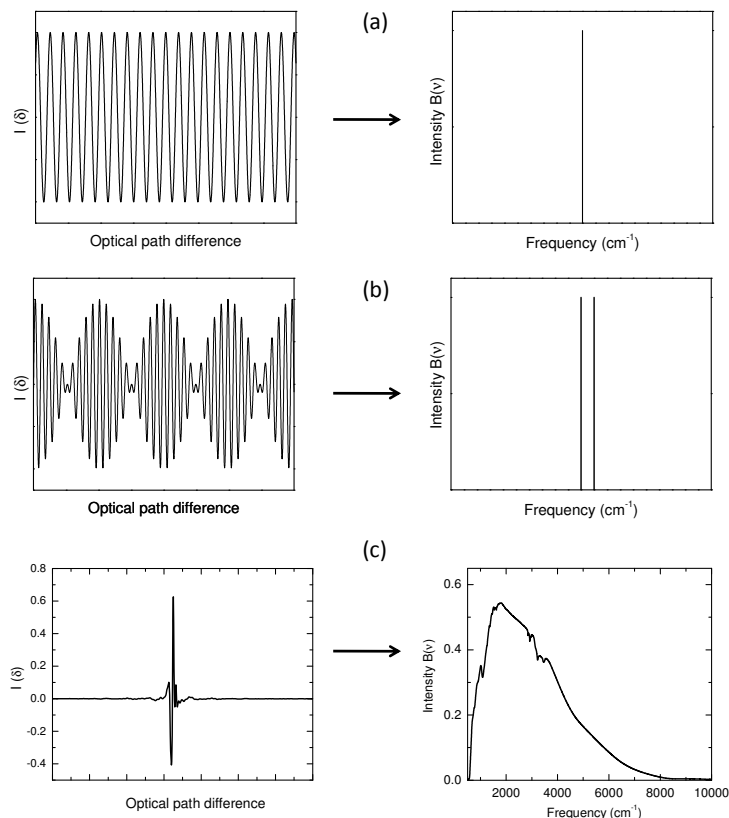
Figure 3.2: Interferograms and their corresponding Fourier transform: (a) monochromatic beam, (b) beating pattern corresponding to two beams of close wavenumbers, (c) A typical interferogram and its corresponding spectrum in the MIR frequency range.

where $I_{(\delta)}$ is the intensity of the detector signal as a function of optical path difference δ and $B_{(\nu)}$ is the spectral power density as a function of frequency ν. In the case of a source emits two frequencies, the resulting interferogram is the sum of the two frequencies interferogram [see Figure 3.2 (b)]. The interferogram in this case called a beat and depends on the path difference. For a polychromatic radiation, the interferogram is complicated because it contains all the spectral information of the radiation and the signal is viewed as a function of constructive and destructive interference from a polychromatic source as shown in Figure 3.2 (c). The interferogram obtained from polychromatic source is a direct function of the optical path difference δ:

$$I_{(\delta)} = \sum_{\nu}^{vi} B_{(\nu i)} \cos(2\pi \delta \nu i) \tag{3.2}$$

3. Fourier transform infrared spectroscopy

For a polychromatic infrared source (IR), the sum can be be replace by an integral

$$I_{(\delta)} = \int_0^\infty B_{(\nu)} \cos(2\pi\delta\nu)d\nu \tag{3.3}$$

or

$$B_{(\nu)} = \int_{-\infty}^{+\infty} I_{(\delta)} \cos(2\pi\nu\delta)d\delta \tag{3.4}$$

These two equations 3.3 and 3.4 are known as Fourier-transform pair. Equation 3.3 shows the variation in power density as a function of path difference or simply interferogram pattern and Equation 3.4 shows the intensity as a function of wavenumber. Each equation can be transformed into the other by Fourier-transformation mathematical method. The typical interferogram and its corresponding spectrum in mid infrared (MIR) region is shown in Figure 3.2 (c). For a typical interferogram, at zero optical path difference $\delta = 0$, all the cosine wave functions are in phase, therefore $I_{(\delta)}$ is maximum. For other optical path difference values, all the cosine waves cancel each other and the intensity decreases rapidly into very small positive and negative lops with diminishing amplitudes. The large optical intensity at $\delta = 0$ is called the central-burst and the size of this central-burst is proportional to the amount of the IR light striking the detector. The low intensity regions of the interferogram are called the interferogram wings [91–93].

The interferogram signal arrives the detector is an analogue signal and it has to be digitized in order that the Fourier-transform can be carried out into spectrum. The mathematical process of Fourier-transform assumes an integration over an infinite displacement. In practice, the integration process carried out over finite displacement, so the interferogram line shape may be as shown in Figure 3.3 (solid line), where the main interferogram band has a series of positive and negative pods with diminishing amplitudes. In dense spectrum, these lobes could appear as lines. The process of removal the side lops is called apodization process. The apodization process can be done by using a suitable function before carrying out the Fourier-transformation [see Figure 3.3 (dotted line)]. The challenge is to choose an appropriate function that does not modify the band shape. Because the
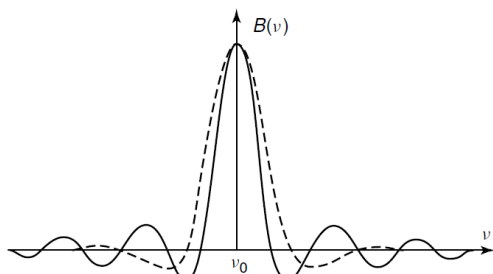
Figure 3.3: Instrument lineshape without apodization (solid line) and after apodization (dotted line) [92].

apodization may correct the side lopes but affect the FWHM of the band leading to resolution reduction [92, 94]. The FTIR resolution is limited by the maximum path difference between the two beams. The theoretical maximum resolution is given by $R_{theo} = 1.207/2\delta$. For example, a path difference of 6 cm^{-1} is required to achieve 0.1 cm^{-1} resolution. But one of the main drawback of using apodization function is the reduction of the resolution, so the practical resolution is given by $R = 0.9/\delta$, which means 9 cm^{-1} is required to achieve 0.1 cm^{-1} resolution [91, 92].

3.1.2 Fourier transform infrared spectrometer

Within this project Bruker IFS 66v/S FTIR spectrometer has been used. The optical layout of the IFS 66v/S spectrometer is shown in Figure 3.4. Depending on the source, the beam-splitter, and the detector the spectrometer can cover a broad frequency range from 10-24000 cm^{-1}. In far-infrared (FIR) region (from 10-700 cm^{-1}), a Hg discharge lamp, mayler beam-splitter, and liquid Helium cooled Silicon based bolometer detector are used. The mid-infrared region (MIR), from 500-8000 cm^{-1}, can be covered by a globar source, KBr beam-splitter, and liquid nitrogen cooled mercury cadmium telluride (MCT) detector. For near-infrared (NIR) and visible (VIS) regions, can be covered with tungsten lamp and CaF$_2$ beam splitter. Liquid nitrogen cooled InSb is used as the detector in the NIR region from 2000-12000 cm^{-1}, whereas Si diode or GaP detectors are used in the VIS from 10000-26000 cm^{-1}. In order to remove the water vapor and carbon-dioxide absorption during measurement, the IFS 66v/S spectrometer must work under vacuum.

3.1.3   Infrared microscope

In the present work, a Bruker IR Scope II coupled with the spectrometer has been used in order to study micrometer size samples inside diamond anvil cell (DAC). Figure 3.4 illustrates the layout of the infrared microscope assembly attached to the spectrometer. The IR radiation coming from the spectrometer is focused
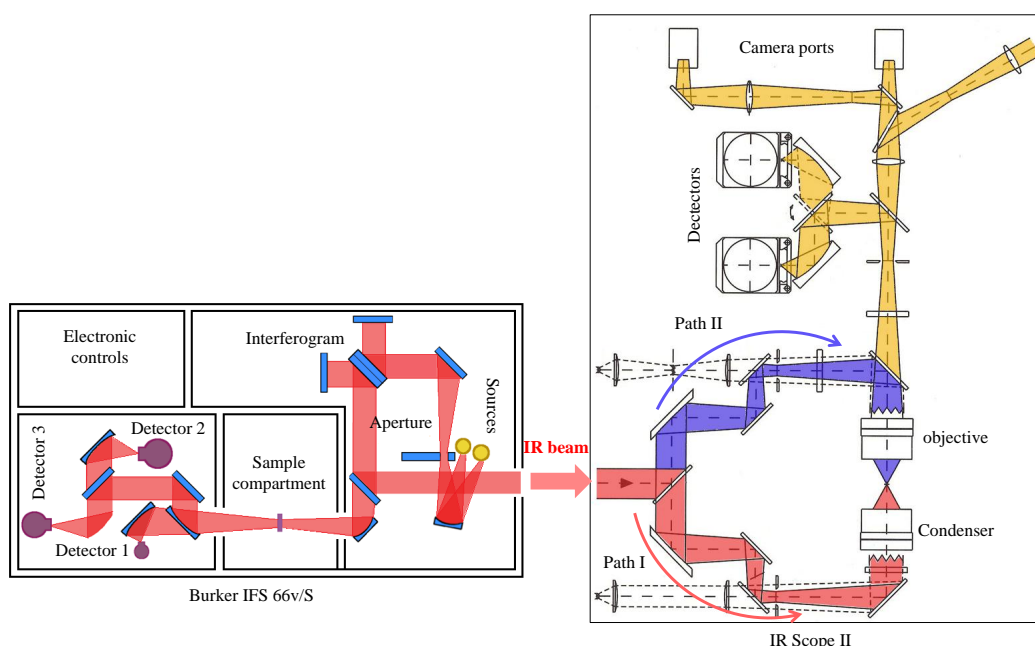
Figure 3.4: Optical layout of Bruker IFS66v/S Fourier transform infrared spectrometer coupled to IR microscope illustrating the entire configuration and the optical beam path.

onto the sample using a refractive Cassegrain condenser. After passing through the sample, the beam is collected by a Cassegrain objective. Then the beam is focused onto the detector. In this case the microscope is working in the transmission mode [see Figure 3.4 path I]. By switching the mirrors in the optical path, the microscope can be converted from the transmission mode to the reflection mode [see Figure 3.4 path II]. The objectives used in the IR scope II are

Schwarzschild objectives, each objective consists of one spherical convex and one spherical concave mirror. The objectives have 15x magnification, 24 mm working distance, and 0.4 numerical aperture. The diameter of the IR beam falling onto the sample can be varied between 20 and 250 μm by using standard apertures. Due to the wave nature of the IR beam, the radiation passing through a circular aperture is diffracted forming a diffraction pattern or what is called Airy pattern. Therefore, the size of the aperture affects the microscope resolution limit. This limit is given by Rayleight's relation:

$$\triangle r = 0.61\lambda/n \ sin(\alpha) \tag{3.5}$$

where λ is the radiation wavelength, n is the refractive index of the medium between the objective and the sample, α is the half opening angle of the objective. The $n \ sin\alpha$ is the numerical aperture of the system [95, 96]. According to this relation the minimum size of the sample in FIR region at around 100 cm^{-1} is 150 μm. In order to remove the water vapor and carbon-dioxide absorption during measurement, the microscope must purged with nitrogen gas.

3.2   Optical coefficients

In this section, the physical quantities needed to describe the optical properties of the investigated samples will be briefly discussed. The optical properties observed in solid state can be simply classified to three types: reflection, absorption, and transition. When a light radiation incident on an optical material, part of the radiation is reflected from the material's front surface and the rest will enters the material and propagate through it. Part of the propagating radiation is absorbed and the rest is transmitted to the other side. In general the reflection and absorption of an optical material can be described by the complex refractive index as follows

$$\tilde{n} = n + ik \tag{3.6}$$

where n is the material refractive index and k is the extinction coefficient. The extinction coefficient is directly related to the absorption coefficient α by the relation $\alpha = 4\pi k/\lambda$, where λ is the light's wavelength in the free space. The refractive index of the medium can be related to its relative dielectric constant ϵ_r by $n = \sqrt{\varepsilon_r}$. If n is complex, then ϵ_r is also complex. The complex dielectric function is given by

$$\tilde{\epsilon}_r = \epsilon_1 + i\epsilon_2 \tag{3.7}$$

where ϵ_1 and ϵ_2 are the real and imaginary part of the dielectric function. Then the complex dielectric function can be written as $\tilde{n}^2 = \tilde{\epsilon}_r$. Then, from Equations 3.6 and 3.7, we can write

$$\epsilon_1 = n^2 + k^2 \tag{3.8}$$

$$\epsilon_2 = 2nk \tag{3.9}$$

and

$$n = \frac{1}{\sqrt{2}}\sqrt{\epsilon_1 + \left(\epsilon_1^2 + \epsilon_2^2\right)^{1/2}} \tag{3.10}$$

$$k = \frac{1}{\sqrt{2}}\sqrt{-\epsilon_1 + \left(\epsilon_1^2 + \epsilon_2^2\right)^{1/2}} \tag{3.11}$$

The optical parameters like the reflection or transmission can be obtained by converting ϵ_1 and ϵ_2 to n and k. According to Fresnel equation, the reflectivity is given by

$$R = \left|\frac{\tilde{n} - 1}{\tilde{n} + 1}\right|^2 = \frac{(n - 1)^2 + k^2}{(n + 1)^2 + k^2} \tag{3.12}$$

This equation is valid when the medium is air or vacuum. The transmittance of the material is given by [97]

$$T = \frac{[(1-R)^2 + 4Rsin(\phi)^2]e^{-\alpha d}}{(1 - Re^{-\alpha d})^2 + 4Re^{-\alpha d}sin(\beta + \phi)^2} \quad , \tag{3.13}$$

where α is the power absorption coefficient given by $4\pi k/\lambda$, d is the thickness of the material, and β and ϕ are the phase change upon passing through the material and reflection, respectively. They are defined as

$$\phi = arctan\left\{\frac{-2k}{1 - n^2 - k^2}\right\} \quad ; \beta = \frac{2\pi nd}{\lambda} \quad . \tag{3.14}$$

3.2.1 Lorentz model

Lorentz-model describes the interaction between the atom and the external applied electric field. The model considers that the electrons of the atoms move in a harmonic motion forced by the external applied electric field. The model is valid for all the transitions for which the final state of an electron lies in a different band but with the same k-vector. Lorentz-model assumes an interaction between the external field and an atom with a single resonant frequency ω_o. Since the oscillating motion loses its energy by collisional processes, therefore a damping factor must be added to the equation of motion. The damping factor has the effect of reducing the peak absorption coefficient and broadening the absorption line [98, 99]. The frequency-dependent dielectric function of the Lorentz-model can be written as

$$\tilde{\varepsilon} = 1 + \frac{4\pi e^2}{m} \sum_j \frac{Nf_j}{\left(\omega_j^2 - \omega^2\right) + i\Gamma_j\omega} \tag{3.15}$$

where m is the free-electron mass, N is the number of charge carriers, ω_j is the resonance frequency of the excitation, ω is the frequency of the incident radiation, Γ is the damping rate, and f_j is the oscillator strength. The f_j expresses the quantum mechanical transition probability. The frequency-dependent of ϵ_1 and

Figure 3.5: (a) Frequency dependence of the real ϵ_1 and imaginary ϵ_2 parts of the dielectric function. (b) Frequency dependence of the real and imaginary parts of the refractive index calculated from the dielectric constant [98].

ϵ_2 of the Lorentz-model are given by

$$\epsilon_1 = 1 + \frac{4\pi Ne^2}{m} \frac{\omega_o^2 - \omega^2}{(\omega_o^2 - \omega^2)^2 + \Gamma^2\omega^2} \tag{3.16}$$

$$\epsilon_2 = \frac{4\pi Ne^2}{m} \frac{\Gamma\omega}{(\omega_o^2 - \omega^2)^2 + \Gamma^2\omega^2} \tag{3.17}$$

Figure 3.5 (a) shows the frequency dependence of the real ϵ_1 and imaginary ϵ_2 parts of the dielectric function. One notes that ϵ_1 increases with increasing the frequency. This is called the normal dispersion. However, ϵ_1 decreases with increasing the frequency near ω_o. This is called the anomalous dispersion [98]. From Figure 3.5 (a) it is clear that the relation between ϵ_2 and the frequency is symmetric about ω_o with maximum value of $4\pi Ne^2/m\Gamma\omega_o$. Figure 3.5 (b) shows the Frequency dependence of the real and imaginary parts of the refractive index calculated from the dielectric constant.

3.3 Infrared spectroscopy under high pressure

Application of pressure can provide us with useful information about how the atomic and electronic properties of the material change under extreme conditions

e.g., phase transformations, optical properties, and magnetic properties. By applying pressure the interatomic distances decrease and hence the lattice becomes stiffer. With further pressure increase beyond a critical value, the atoms have to overcome strong repulsive potential and the lattice becomes incompressible. As the interatomic distances decrease, the outer electronic orbitals will overlap, leading to broadening of the electronic energy bands and shifting of the energy bands with respect to Fermi-level [100]. In this section all the details related to the high pressure measurement will be explained in details.

3.3.1 Diamond anvil cell

Diamond anvil cell (DAC) is a simple device used to apply pressure on micrometer size samples. A general scheme for the DAC is shown in Figure 3.6. The DAC consists of two diamonds which are perfectly held opposite to each others, where the sample is compressed between the culets. A metallic gasket with a small hole in the middle which serves as the sample chamber is placed between the two diamonds. The hole is then loaded with few ruby balls for pressure determination. Then, the hole filled with a proper pressure transmitting medium. To apply pressure, the DAC's faces are forced towards each others. Due to the large ratio between the applied force on the diamond's outer surface and the culet area, high pressure values in the range of gigapascal (GPa) can be achieved. Thus, the smaller the culet area, the higher is the pressure that can be achieved. Diamonds are usually selected from brilliant-cut gem stones. The lower octahedral culet is grinded to flat surface of approximately 400-800 μm depending on the DAC type and the maximum pressure to be achieved. Then, the culet is usually set parallel to the (100) or the (110) plane of the diamond. The diamond face opposite to the culet face is called the table and it has an area of 8-12 mm^2. Diamond is very hard and incompressible material and it has the advantage of being transparent to a wide range of the electromagnetic radiation. Diamond type-IIA is pure, transparent, and almost impurities free which makes this kind of diamond suitable for optical pressure spectroscopy studies under high pressure [101]. In the spectral range between 1700-2700 cm^{-1}, a strong multi-phonons absorption is observed, so this region must be ignored during the spectrum analysis.
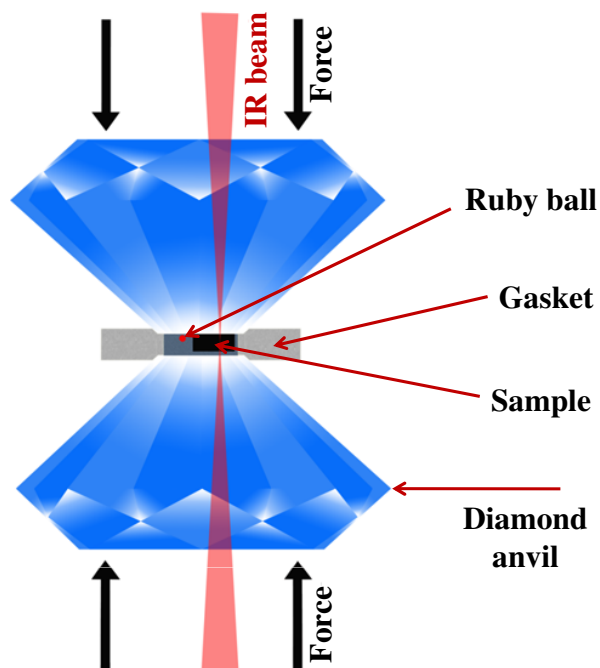
Figure 3.6: Schematic representation of the working principle of a DAC.

A metallic gasket is used to provide a chamber for the sample and the pressure transmitting medium (PTM) and also to protect the two diamonds. Different materials can used as a gasket depending on the pressure value to be achieved and the physical properties of the material under investigation [101]. For non-magnetic materials, stainless-steel gasket can be used but for magnetic materials CuBe gasket is used. Also, for magnetic materials, Inconel gasket can be used to achieve high pressure values because it is harder than CuBe and contains less amount of iron compared to stainless-steel $\sim$3 % maximum. A suitable gasket material is pressed between the two diamonds anvils to a thickness of $\approx$ 70-90 μm. Then, by using a Electric Discharge Machine (EDM), a hole can be drilled in the middle of the pressed area which serves as sample chamber. The drilled gasket is fixed to the lower diamond for filling with sample, ruby ball, and pressure transmitting medium. The same orientation of the gasket during the pressing between the two diamond anvils has to be kept during applying the pressure. The typical diameter of the hole is ranging from one third to two fifth of the culet size. When liquid helium or liquid nitrogen is used as pressure transmitting medium, the hole shrinks after filling, so bigger holes are needed. For this project,

stainless-steel gaskets were used for both Cryo DAC mega and Syassen-Holzapfel DACs. To reach high pressure up to $\sim$ 20 GPa using Syassen-Holzapfel DAC, Stainless-steel gaskets were pressed to thicknesses of $\sim$ 75-85 μm and the hole sizes were in the range of 120-150 μm. In the case of Cryo DAC mega DAC, to reach pressure values up to 15 GPa the hole sizes were in the range of 200-250 μm.

3.3.2 DACs used for this project

Within this project, two types of DACs were used (i) Syassen-Holzapfel and (ii) cryoDAC Mega DACs. The working principle of both DACs is very similar. The differences between the two DACs are due to different ways of force generating and the anvil-alignment mechanisms. The working principle of both DACs are described in the following subsections

3.3.2.1 Syassen-Holzapfel DAC

This cell was designed by Huber Syassen and Holzapfel in 1977. Photo and cross-sectional view of Syassen-Holzapfel DAC are shown in Figure 3.7 (a) and (b), respectively. The diamond used in this DAC is type-IIA with high of 1.6 mm and 400 μm culet diameter. The numerical apertures of the backing plate side and the piston side are 36° and 24°, respectively. The mechanism of applying pressure is generated by a thread-and-knee mechanism [101, 102]. By turning simultaneously the two threads rods, the lower ends of the brackets will move toward each others. Consequently, compressing the moving piston and generate pressure. Due to the special design of Syassen-Holzapfel DAC, where the long piston moves strictly parallel to the axis of the DAC, the DAC has an excellent alignment stability. This results a large force multiplication and generation of pressure up to 25 GPa.

3.3.2.2 CryoDAC Mega DAC

The CryoDAC-Mega is a commercial DAC manufactured by Almax easyLab Group Ltd [103]. A photo of the DAC parts are shown in Figure 3.8. The CryoDAC-Mega DAC is a very versatile DAC made from CuBe alloy. It is suitable for both optical and X-ray diffraction studies of magnetic materials at room
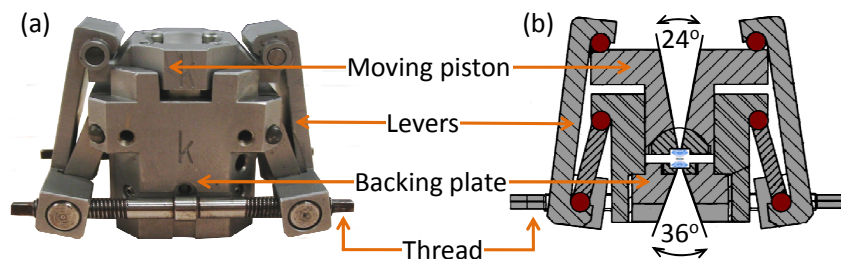
Figure 3.7: (a) Photo and (b) cross-sectional view of Syassen-Holzapfel DAC [101].
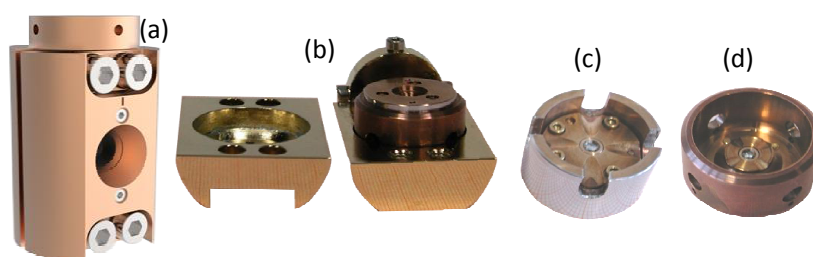
Figure 3.8: (a) Photo the DAC (b) Body of the DAC (c) Piston assembly with top diamond anvil, (d) Cylinder assembly with bottom diamond anvil.

and cryogenic temperatures. Due to its high numerical aperture it is well suited to use with FTIR and other types of spectrometer. The diamond anvils are mounted within force-fitted CuBe rings and mechanically fixed to their tungsten carbide support plates, thereby avoiding use of epoxy resins or other adhesives. The CryoDAC-Mega is held within two CuBe blocks as shown in Figure 3.8 (b). The cylinder assembly with bottom diamond anvil is fixed to the one of the CuBe blocks, while the piston assembly with top diamond anvil is fixed strictly over the cylinder. The second CuBe block fits over the piston and is used to apply load to the cell by means of four bolts. The diameter of the complete assembly is 38 mm. The culet diameter is 600 μm and a maximum pressure of 15 GPa can

be achieved with the use of CuBe or stainless-steel gaskets [1]. Before applying pressure using DAC the two diamond anvils must be perfectly aligned with respect to each others. This could be achieved by using tilting and/or transitional screws. The two culets must be carefully placed on each others under normal optical microscope. An interference fringes between the two diamond anvils will appear. After that tilting or position shift must be adjusted from the proper screws till the interference disappeared.

3.3.3 Pressure measurement

In this project, the ruby luminescence technique was used for the pressure measurement. Ruby is α-alumina (α-Al$_2$O$_3$) doped with a small fraction of Chromium ions Cr^{3+}. The Chromium ions replace the aluminium ions, where each Chromium ion is surrounded by six Oxygen O^{2-} ions. The free Cr^{3+} ion has three electrons in the 3d shell. Due to the strong crystal field, the five 3d orbitals of the Cr^{3+} ion no longer have the same energy. In α-Al$_2$O$_3$ crystal the strong crystal field leads to a cubic and trigonal splitting of the energy levels of the Cr^{3+} ions [104, 105]. At room temperature all electrons are in the ground state A$_2$. When the ruby balls are illuminated with green laser (λ=523 nm and power of 6 mW) the electrons are excited to T$_2$ and T$_3$ levels, then the electrons undergo fast non-radiative decay to the metastable ^{2}E doublet state. From metastable doublet state, the electrons relax to the ground energy level ^{2}A$_4$ with the emission of characteristic radiations R$_1$ and R$_2$ lines at 694.2 nm and 692.8 nm, respectively, at ambient conditions. Under hydrostatic pressure the distance between the Cr and O ions decreases. Therefore, the crystal field at the Cr^{3+} will increase and the energy splitting changes, leading to a decrease of the energy gap between the ^{2}E doublet state and the ground state. Thus, the R$_1$ and R$_2$ lines shift to higher wavelength as shown in Figure 3.9 (b). For pressures below 30 GPa the pressure-induced shifts of the Ruby R$_1$ line can be described by the equation [106]:

$$P(GPa) = \left(\frac{A}{B}\right)\left[\left(1 + \frac{\delta\lambda}{\lambda_o}\right)^B - 1\right] \tag{3.18}$$

---

[1] All information about CryoDAC Mega DAC was adapted from Almax easyLab Group Ltd web page [103].
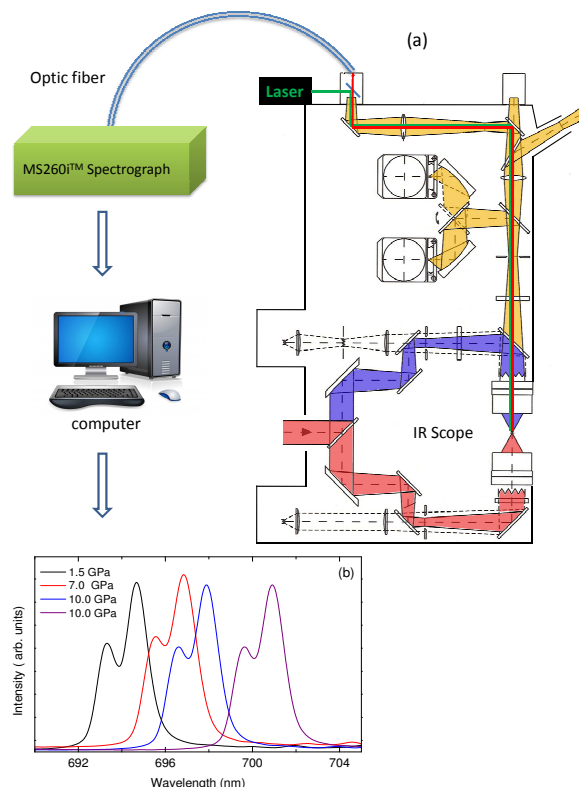
Figure 3.9: (a) Schematic representation of ruby luminescence setup used for pressure measurement. (b) The luminescence spectra of ruby excited by green laser for selected pressures at room temperature.

where A = 1904 GPa, B = 7.665, $\delta\lambda$ is the shift in the frequency of R_1 line with increasing pressure, and λ_o is the wavelength at ambient pressure (694.23 nm for R_1 at 298 K). The ruby lines R_1 and R_2 are sensitive to temperature and exhibit a positive shift with temperature. The linear scale holds good at any temperature down to 4.2 K [101, 107–109]. Figure 3.9 (a) shows the schematic representation of the ruby luminescence setup coupled to the IR microscope. The ruby ball placed inside the DAC is shined by a green laser of wavelength 532 nm produced by the diode-pumped solid-state laser with a power of 6 mW. The laser line transmitted through a dichroic mirror, where it reflects light of wavelengths in the range 500-580 nm and transmits light with other wavelengths. Thus, the 650 nm luminescence spectrum of the red light from the ruby is transmitted through the mirror to a high resolution charge coupled device (CCD) spectrograph via an optical fiber. In this project, a commercial CCD spectrograph MS260i^{TM}

[1] grating-type imaging spectrograph was used. It consists of an asymmetrical in-plane Czerny-Turner optical configuration with unequal entrance and exit focal lengths of 220 mm and 257 mm, respectively. The grating of this spectrograph consists of 1800 lines/mm. A set of computer optimized toroidal mirrors produce accurate images of the input slit in the flat output plane. The spectrograph has a excellent spatial resolution of 40μm. The signal at the exit slit is then detected by a CCD camera. The detection element of the CCD camera has 1024×127 pixels in an area of 26×26 μm^2. The accuracy of pressure determination using this ruby luminescence arrangement is 0.1 GPa.

3.3.4 Pressure transmitting medium

Within the present study, three pressure transmitting media were used (i) alcohol-mixture (4:1 methanol-ethanol), (ii) liquid argon, and (iii) liquid nitrogen. The gasket is glued to the seat of the lower diamond and then the sample is loaded with few ruby balls into the hole followed by the pressure transmitting medium filling. In the case alcohol-mixture filling, only one drop from the alcohol is dropped carefully overt the sample and the ruby balls after that the DAC has to be closed quickly. Then, a small pressure is applied to keep the alcohol inside the hole.

For argon filling an in-house-assembled cryogenic-filling setup has been used. The gasket is glowed to the seat of the lower diamond and loaded with sample and few ruby balls. After that the DAC is partially closed so that the cryogenic medium can flow in and fill the sample chamber. Then the DAC is fixed to holder with special adaptations to accommodate the way of applying pressure. The holer with the DAC is inserted inside a stainless-steel chamber and fixed with screws to ensure sufficient vacuum inside the chamber. The chamber is pumped with roughing pump and then purged with argon. This process has to be repeated several times in order to reduce water vapour to acceptable level. The chamber is then cooled with liquid nitrogen bath. Then argon gas is flowed into the chamber and regulated such that a constant gas pressure of about 0.8 bar is maintained in

---

[1]All the information about the CCD spectrograph was adapted from the MS260i CCD spectrograph information manual [110].

the chamber. During this process, the argon liquefies and flows inside the DAC. The DAC is then closed with the aid of the remote access mechanism provided in the cell holder. In the case of nitrogen filling, the same processes of argon filling are repeated except that the holder with the DAC is inserted directly to liquid nitrogen. Then, the DAC is closed with the aid of the remote access mechanism provided in the cell holder.

It has been shown that the pressure transmitting medium (PTM) plays an important role for the pressure-induced effects in carbon nanotubes [111]. Therefore, it is necessary that the medium provides hydrostatic pressure on the material under investigation, to record accurate intrinsic material properties. Thus, it is important to characterize the pressure media used in this work. Klotz et al. [112], presented a systematic and comparative study of the pressure-induced solidification for different pressure transmitting media using the ruby luminescence technique. Figure 3.10 shows the pressure dependence of the standard deviation σ for (a) 4:1 methanol:ethanol alcohol, (b) argon, and (c) nitrogen PTM. From Figure 3.10 (a), one notes that alcohol-mixture is a hydrostatic PTM below 10 GPa but becomes quasi-hydrostatic above 10 GPa due to solidification. Argon is a rare gas and has the advantage that it is relatively easy to load and inexpensive but it solidifies at 1.4 GPa at 300 K. As shown in Figure 3.10 (b), the hydrostaticity limit of argon is $\sim$ 10 GPa. Nitrogen solidifies at 2.4 GPa and has a hydrostaticity limit of $\sim$ 15 GPa as shown in Figure 3.10 (c). From the above discussion we can conclude that nitrogen has higher hydrostaticity level compared to argon and alcohol-mixture as PTM.

3.4 Free-standing films preparation

All the nanotubes samples under investigations in this project are black powder, so it difficult to measure optical spectroscopy for such materials. Therefore, optically homogeneous transparent free-standing films have been prepared to be suitable for the transmission measurement. For this purpose the filtration method of the nanotubes from Triton X-100 suspension was used [113]. The idea of this method is to filter under vacuum a dilute surfactant-based suspension of purified nanotubes onto a filtration membrane. After filtration the nanotubes tend to

3. Free-standing films preparation
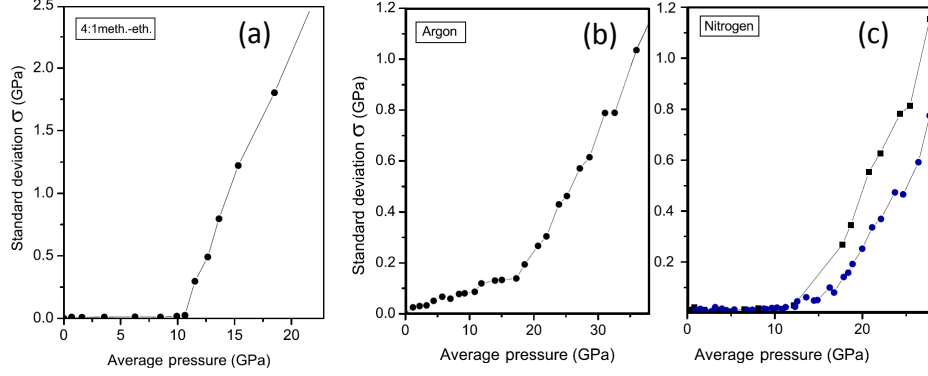
Figure 3.10: Pressure dependence of the standard deviation σ for (a) 4 : 1 methanolethanol alcohol, (b) argon, and (c) nitrogen [112].

overlap due to the van der Waals forces dominating after removing the surfactant. The advantages of this technique are (i) the film thickness is controlled by the nanotube concentration and volume of the suspension filtered, (ii) the films are transparent for IR beam, and (iii) the high mechanical stability of the free-standing films. Free-standing films from SWCNTs, C_{60}-peapods, C_{70}-peapods, DWCNTs/C_{60}, DWCNTs/C_{70} and I-SWCNTs samples were prepared as the following procedure: a stable suspension of nanotubes samples was prepared using Triton X-100 as a surfactant with the help of ultrasonic probe. The suspension must be transparent with faint gray color and stable. By careful pouring of the suspension over a cellulose nitrate membrane (0.22 μm GSWP-Millipore) attached to a glass funnel under vacuum [Figure 3.11 (a)], very thin bucky-paper was obtained [Figure 3.11 (b)]. The prepared bucky-paper was washed several times with distilled water and ethyl alcohol to remove the excess of the Triton X-100. A small piece of the bucky-paper was transferred in an acetone bath. The cellulose nitrate membrane will dissolve in the acetone bath and a free-standing film of nanotubes will float over the acetone surface as shown in Figure 3.11(c). The free-standing film was removed from the acetone solution by using Aluminum foil with a hole in the middle [Figure 3.11 (d)]. A small piece of the free-standing film $\approx$ 60-70 μm was loaded into the diamond anvil cell (DAC) for high pressure measurements as shown in Figure 3.11 (e).
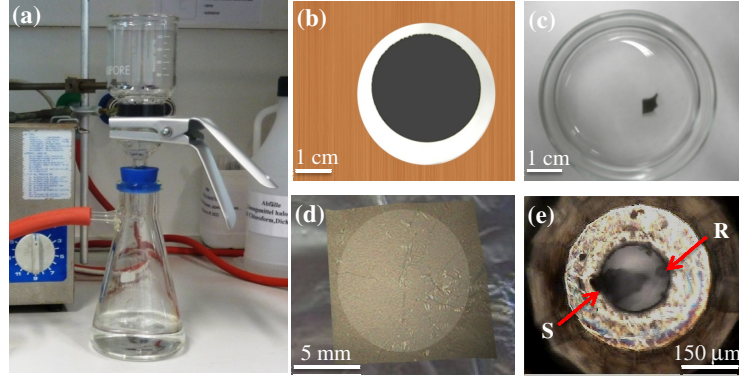
Figure 3.11: (a) Cellulose nitrate membrane(0.22 μm) attached to a funnel under vacuum. (b) Photograph of the carbon nanotubes- derived bucky paper. (c) Free standing carbon nanotubes film floating over acetone solution after dissolution of the cellulose nitrate membrane in the acetone solution. (d) Optical image for the free standing film over Aluminum foil. (e) Optical image for the DAC loaded with carbon nanotubes film (S) and a ruby ball (R) for the pressure determination.

3.4.1 Transmission measurements

For transmission measurements, the intensity $I_{sample}(\omega)$ of the radiation transmitted through the sample and the intensity $I_{reference}(\omega)$ of the radiation transmitted through the PTM in the DAC are measured as shown in Figure 3.12. In the case of free-standing film at ambient conditions, $I_{reference}(\omega)$ is the radiation transmitted through the air. From $I_{sample}(\omega)$ and $I_{reference}(\omega)$ the transmittance and absorbance spectra are calculated according to $T(\omega)=I_{sample}(\omega)/I_{reference}(\omega)$ and $A(\omega)= -\log_{10}T(\omega)$, respectively.
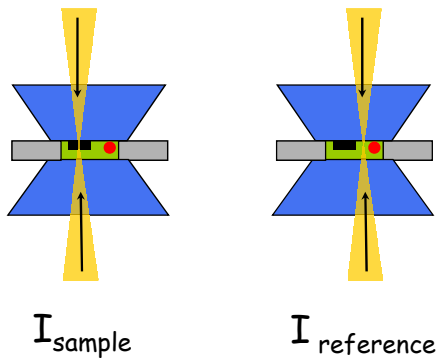
Figure 3.12: Sketch of the measurement configuration for obtaining the transmission of a sample in a DAC.

3.5 Raman spectroscopy

Within this project, two Raman spectrometers were used:

1. Raman spectra performed by M. Fisher in collaboration with Dr. M. Schreck, Experimental Physics 4 - Universität Augsburg. The samples were excited by 488 and 515 nm argon lasers at room temperature and the spectra were recorded by a triple Raman spectrometer T64000 (Horiba Jobin Yvon), interfaced to an Olympus BX-40 microscope (100 x LWD objective). The laser power impinging on the sample was 0.1 mW. The Raman spectrometer was calibrated by using mercury line at 435.8 nm.

2. Raman spectra performed by K. Haubner in the group of Prof.Dr. L. Dunsch, Center of Spectroelectrochemsitry, Department of Electrochemsitry and Conducting Polymers, IFW Dresden. The samples were excited by the 676 nm of an Kr^+ laser (Innova 305, Coherent) and the spectra were recorded by a T-64000 spectrometer (Horiba Jobin Yvon) interfaced to an Olympus BX-41 microscope (50 x LWD objective). The laser power impinging on the cell window was 1 mW. The Raman spectrometer was calibrated before each set of measurements by using the F1g line of Si at 520.2 cm^{-1} for reference.

3.6 Electron Microscopy

High resolution transition electron microscopy (HRTEM) were performed by F. Börrnert in the group of Dr. M. H. Rümmeli, IFW Dresden. The samples were characterized in different preparation stages with a JEOL JEM-2010F transmission electron microscope retrofitted with two CEOS third-order spherical aberration correctors for the objective lens (CETCOR) and the condenser system (CESCOR). The microscope was operated using an electron acceleration voltage of 80 kV to reduce knock on damage. Local energy dispersive X-ray (EDX) spectra were taken with a Bruker XFlash 5030T silicon drift detector attached to the microscope.

Chapter 4

Samples Preparation and Free-Standing Films Characterizations

4.1 Samples Preparation

The focus of this investigation is the preparation and characterization of size-controllable DWCNTs. For this purpose, the chemical vapor deposition (CVD) and fullerene-peapods methods will be used. For size-controllable DWCNTs preparation via the CVD method, the catalysts will be engineered by precisely controlling the Fe and Mo nanoparticles [114]. In the case of the peapods method, C_{60} and C_{70}-peapods will be prepared using the sublimation method as a preliminary products and the DWCNTs will be produced as a final product by tempering the peapods at 1250°C. In addition, iodine-filled SWCNTs (I-SWCNTs) will be prepared. All the prepared samples will be characterized by using scanning electron microscopy (SEM), high resolution transmission electron microscope (HRTEM), Raman spectroscopy, and optical spectroscopy. Furthermore, the pressure-induced phenomena in peapods and DWCNTs will be studied by optical microspectroscopy.

4.1.1 Chemical Vapor Deposition Method

4.1.1.1 Catalysts Preparation $Fe_{0.9}Mo_{0.1}Mg_{13}O$

Fe and Mo nanoparticles supported on Magnesium Oxide (MgO) have been demonstrated to be efficient for synthesis of DWCNTs. The combustion route method was used for the catalysts preparation [115, 116]. The typical preparation method is as follows: weighted amount of Ammonium molybdate hydrate $(NH_4)_6Mo_7O_{24}.4H_2O$ (99.98 % - Sima-aldrich) was added to an aqueous solution containing ferric nitrate $Fe(NO_3)_3.9H_2O$ (99.99%-aldrich) and magnesium nitrate $Mg(NO_3)_2.6H_2O$ ($\simeq$ 99%-aldrich), keeping the molar ratio of Mo:Fe:MgO at 0.1:0.9:13. An appropriate amount of combustion agent (urea) was added to the aqueous solution. The ratio of urea is three times the stoichiometric ratio. Then the mixture was kept in an oven at 70°C for 12 h. A thick orange-red solution was formed. Then the solution was placed in a furnace preheated at 550°C. The thick orange-red solution immediately started boiling and blazed with a white flame. The total combustion process overs in 10 min. The combustion product was baked at 550°C for 3 h and ground to a fine powder.

4.1.1.2 DWCNTs Grown by the CVD Method

Synthesis of DWNTs was carried out an in-house-assembled CVD setup. The complete CVD setup is shown in Figure 4.1. The preparation method is as follows: 200 mg of the $Fe_{0.9}Mo_{0.1}Mg_{13}O$ catalyst was spread uniformly onto a quartz boat. The quartz boat was inserted into the center of the quartz tube mounted inside an electrical tube furnace. Subsequently, the furnace was heated to 950°C in an argon atmosphere. Then, a mixture of gases, typically ethylene and Argon was introduced into the reactor. The flow rates of ethylene and argon were maintained at 50 and 100 sccm, respectively. After 20 min, the reactor was cooled to room temperature in an Argon atmosphere. The resulting black dense material containing carbon nanotubes (CNTs) around the oxide grains was ground carefully to a fine powder.
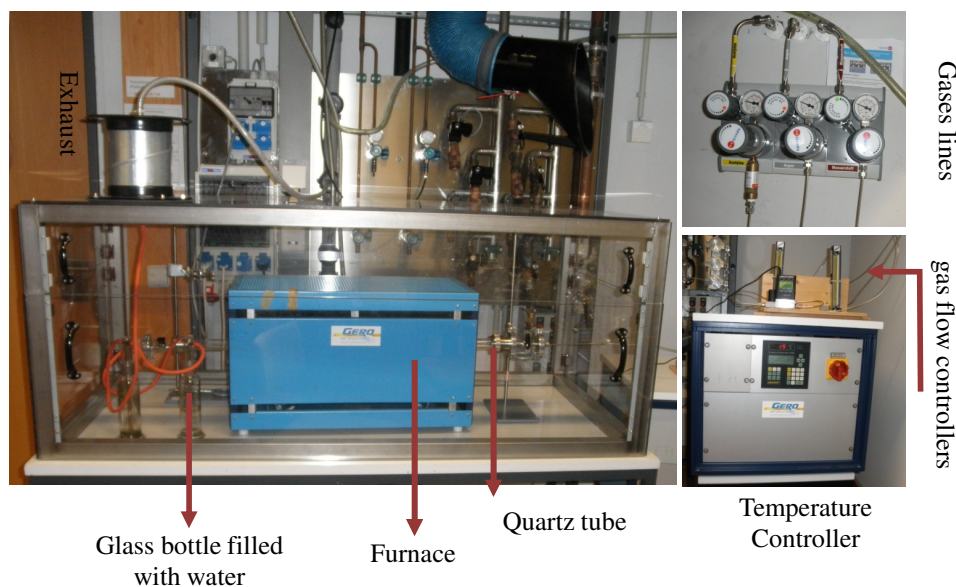
Figure 4.1: complete an in-house-assembled CVD setup chemical vapour deposition setup.

4.1.1.3   CNTs Purification

The as-prepared CNTs were treated with concentrated hydrochloric acid (HCl) at 60°C for 24 h according to the procedure in the literature [116, 117]. To not destroy the nanotubes due to the acid treatment, the nanotubes were kept in water, and then HCl acid was gradually added. The temperature was increased gradually to 60°C under reflux condition for 24 h. The product was washed with distilled water several times to remove and neutralize the acid. Then the product was dried, dispersed in ethanol under sonication, and filtered using Millipore (0.2 μm) filter paper. The filtered product was dried in an oven at 100°C for 2 h. In order to effectively remove the amorphous carbon present on the nanotubes walls, the dried sample was heated to 850°C in a furnace at a rate of 3°C per minute in flowing hydrogen at 100 sccm and held at that temperature for 6 h. The resulting sample was again stirred in concentrated HCl at 60°C for 3 h and heated in a furnace at 850°C for 6 h in flowing hydrogen (100 sccm).

4.1.1.4 SEM and HRTEM Characterization

Figure 4.2 (a) and (b) show the SEM images of the as prepared CNTs with low and high magnification, respectively. The images indicate the presences of CNTs bundles with diameters ranging from 20 to 60 nm and a length of $\approx$ 20 μm. Also, the images show the presence of noncrystalline carbon and large quantities of the catalyst. Figure 4.2 (c) and (d) show the SEM images of CNTs after the purification process with low and high magnification, respectively. The images show a large amount of tangled nanotubes with several tens of micrometers length. It is clear from the SEM images that CNTs have prepared without any significant amount of amorphous carbon and also no presence of the catalyst. To estimate the amount of DWCNTs in the sample, the HRTEM will be used. Figure 4.2 (e) and (f) show the HRTEM for two different regions of the purified

Figure 4.2: Low (a) and high (b) magnification SEM images of the as prepared CNTs obtained by CVD method over $Fe_{0.9}Mo_{0.1}Mg_{13}O$ catalyst. Low (c) and high (d) magnification SEM images of purified CNTs. (e) and (f) HRTEM of the purified CNTs at two different positions. The images show the formation of MWCNTs with at least 6 walls.

4. Samples Preparation

CNTs sample. It is clear from the images that the sample contains multi-walled carbon nanotubes (MWCNTs) with at least 6 walls. This means a lot of eff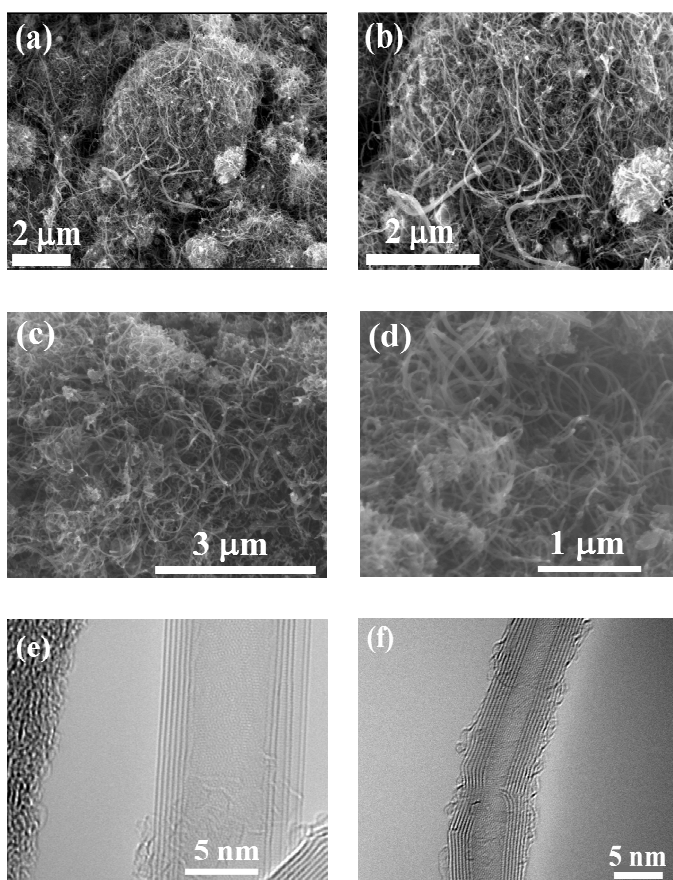orts still needed to optimize the catalysts composition, not only to prepare pure DWCNTs but also to fine tune the DWCNTs diameters. Since the main goal of the present work is to study the optical spectroscopy of DWCNTs under high pressure, so a narrow tubes diameter distribution of DWCNTs is needed. To prepare DWCNTs with a narrow diameters distribution, the alternative plan will be used. In this plan, DWCNTs were prepared using the peapods method. Two types of peapods: C_{60}-peapods and C_{70}-peapods were prepared.

4.1.2 Peapods Method

4.1.2.1 Preparation of C_{60} and C_{70}-peapods

Chemicals. Arc discharge SWCNTs were purchased from Carbon Solutions Inc. (Type P2, average diameter 1.4 nm and batch No. 02-444). The P2-SWCNTs were prepared using arc discharge method. C_{60} and C_{70} fullerene with purity 99.98% was purchased from Term USA. Triton X-100 ($\sim 10\%$ in H_2O) was purchased from Sigma-Aldrich.

Synthesis. The empty SWCNTs were filled with C_{60} and C_{70} molecules using the sublimation method [118]. The typical preparation method is described as follows: SWCNTs were tempered in furnace at 575°C (the temperature was increased by 1°C/min.) for 1 h. This process is important to open the caps of the SWCNTs and also to remove any amorphous carbon from the sample. 25 mg of SWCNTs and 25 mg of C_{60} or C_{70} molecules were degassed under dynamic vacuum (1×10^{-6}mbar) at 200°C for 24 h, subsequently, the SWCNTs and the fullerene molecules were sealed in a quartz tube under vacuum $\approx 1\times10^{-6}$ mbar and heated at 750°C for 5 days continuously. To remove the non reacted fullerene from the outer surface of the SWCNTs, the peapods were heated at 700°C under dynamic vacuum for 3 h. The prepared peapods were then transformed to DWCNTs by tempering the peapods at 1250°C for 24 h under dynamic vacuum and subsequently cooling the furnace to room temperature. The notations DWCNTs/C_{60} and DWCNTs/C_{70} will be used for the DWCNTs prepared from C_{60} and C_{70} peapods, respectively.

4.1.2.2 Iodine-filled SWCNTs

Iodine-filled SWCNTs (I-SWCNTs) were prepared using the method described by Guan *et al.*, [119]. The typical preparation method is described as follows: opened-caps SWCNTs were degassed under dynamic vacuum $\approx 1\times10^{-6}$mbar at 200°C for 24 h. A mixture of SWCNTs bulk powder and iodine were sealed in quartz tube under vacuum $\approx 1\times10^{-4}$ mbar and heated at 150°C for 1 day continuously. To remove the non reacted iodine from the outer surface of the SWCNTs, the I-SWCNTs were heated at 50°C under dynamic vacuum for 3 h. Figure 4.3 shows a closed evacuated quartz tube containing SWCNTs and iodine powders and a heated tube with violet iodine vapour.

Figure 4.3: Top: closed evacuated quartz tube containing SWCNTs and iodine powders. bottom: Heated tube with violet iodine vapour

4.2 Characterization

4.2.1 HRTEM Characterization

Figure 4.4 (a) shows the HRTEM low-magnification image of the empty P2-SWCNTs before the heat treatment. The image indicates the presence of carbon nanotubes bundles with average tube diameters ranging from 10-20 nm and also the presence of insignificant amount of amorphous carbon. The heat treatment at 575°C opens the nanotubes caps and removes most of the amorphous carbon from the outer surface of the nanotubes as shown in Figure 4.4 (b). From Figure 4.4 (b) we can observe only few traces of the amorphous carbon over the nanotubes surface, this is because the HRTEM can focus on individual nanotube and easily
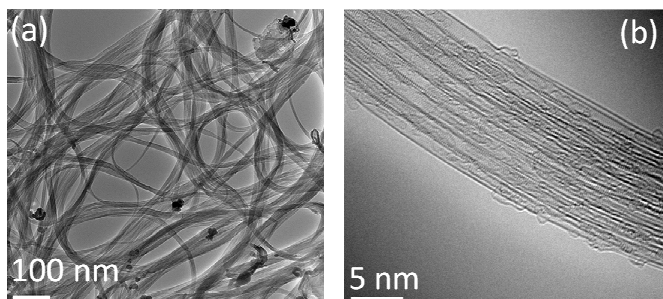
Figure 4.4: (a) low magnification HRTEM image of empty P2-SWCNTs before the heat treatment. (b) high magnification HRTEM image of empty P2-SWCNTs after heat treatment at 575°C.

detect such insignificant amount of amorphous carbon. The magnified image also reveals that the starting SWCNTs are empty with an average diameter of 1.42 nm, which is suitable for the incorporation of the C_{60} and C_{70} molecules into the interior of the nanotubes, since the minimum diameter of SWCNTs required for the incorporation is 1.28 nm [65].

Figure 4.5 (a) and Figure 4.6 (a) show the formation of 1D chain peapods from C_{60} and C_{70} molecules inside the SWCNTs, respectively. The images indicate the high filling ratio of the peapods, which is $\geqslant 95\%$ and $\geqslant 90\%$ in the case of C_{60} and C_{70} peapods, respectively. Figure 4.5 (b) and Figure 4.6 (b) show that the distance between each two adjacent C_{60} molecules is close to 1 nm. The high filling ratio in this case could be attributed to the higher temperature used and long treatment time (750°C for 5 days). Since the process of increasing temperature inside a closed tube is isochoric process, the pressure inside the tube will increase due to the vaporization of more fullerene molecules [118] consequently, the kinetics of the fullerene molecules will increase and hence large number of the fullerene molecules will arrive to the surface of the SWCNTs. With the large number of the vaporized molecules arriving to the surface of the SWCNTs and the long treatment time, more C_{60} or C_{70} molecules will be forced to incorporate inside the nanotubes, leading to the high filling ratio. From Figure 4.5 (c) and Figure 4.6 (c) one can observe the effect of the electron beam irradiation on the C_{60} and C_{70} molecules. The C_{60} and C_{70} molecules started to polymerize into small capsules. This behaviour could be explained as follows: The binding energy of the carbon atoms in the fullerene molecules is about 7.4 eV [77] which is less than that of carbon nanotubes (about 10 eV) [120]. The energy from the electron beam will displace carbon atoms from the fullerene molecules easily than from
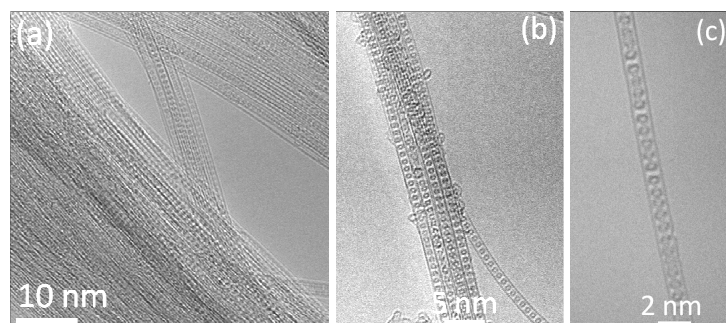
Figure 4.5: (a) HRTEM image of C_{60}-peapods bundles clearly showing the high filling ratio of the nanotubes. (b) C_{60}-peapods bundle, showing that the C_{60} are highly close-packed. (c) HRTEM image showing the formation of short capsules under the influence of the electron beam irradiation.
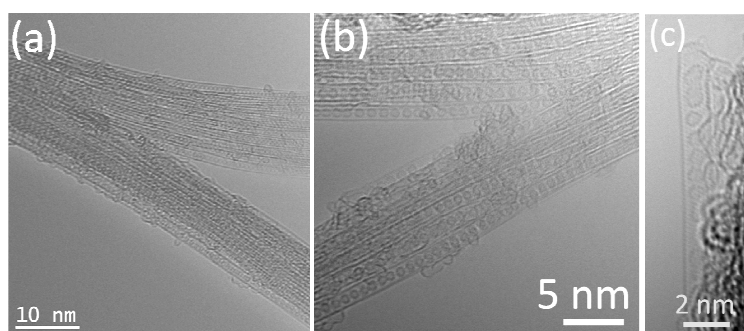
Figure 4.6: HRTEM image of (a) C_{70}-peapods bundles clearly showing the high filling ratio of the nanotubes. (b) C_{70}-peapods bundle, showing that the C_{70} are highly close-packed. (c) HRTEM image showing the formation of short capsules under the influence of the electron beam irradiation.

the nanotubes. The polymerization starts with an arrangement process of the deformed C_{60} molecules giving more stable short capsules inside the boundaries of the SWCNTs [121].

Figure 4.7 (a) and Figure 4.8 (a) show the HRTEM images of the DWCNTs/C_{60} and DWCNTs/C_{70}, respectively. It is clear from the images that DWCNTs derived from the C_{60} and C_{70}-peapods were prepared after heat treatment at 1200°C for 24 hrs. Figure 4.7 (b) and Figure 4.8(b) show top view images for both samples. Figure 4.7 (c) and Figure 4.8 (c) show only one DWCNTs, to confirm the formation of the inner tube inside the SWCNTs. One can observe that the inner tube is defect free. This can be attributed the the multi-steps of rotation C-C
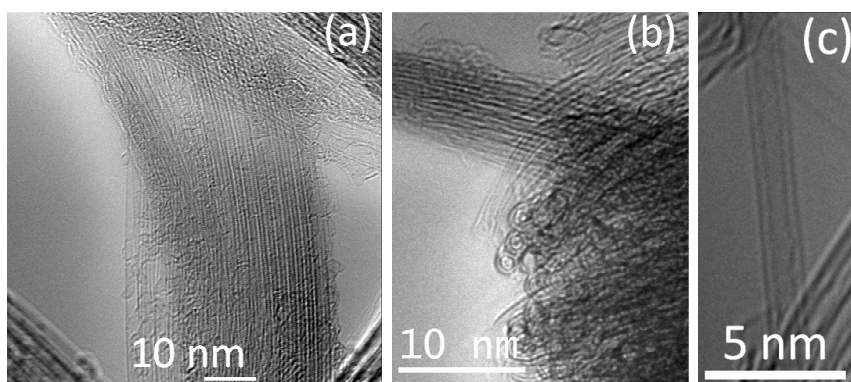
Figure 4.7: HRTEM image of a bundle DWCNTs/C_{60} derived from /C_{60}-peapods. (b) Top view HRTEM of DWCNTs/C_{60} bundles. (c) HRTEM image of a single DWCNT.
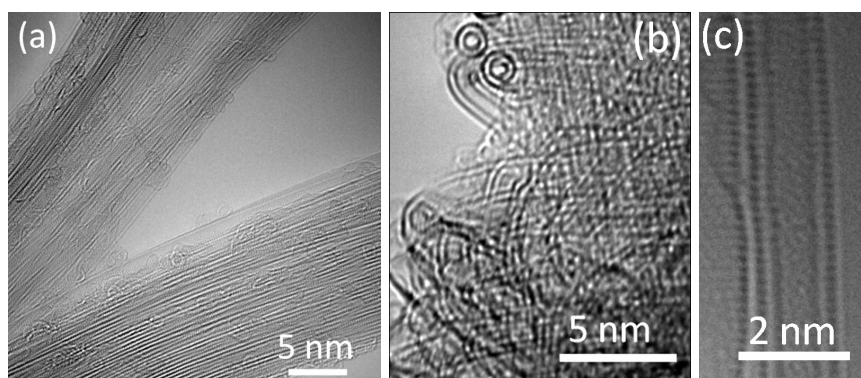
Figure 4.8: HRTEM image of a bundle DWCNTs/C_{70} derived from /C_{70}-peapods. (b) Top view HRTEM of DWCNTs/C_{70} bundles. (c) HRTEM image of a single DWCNT.

bonds in the sp^2 carbon network or what is called Stone-Wales (WS) transformation, it takes long time and needs high temperature [74].

Figure 4.9 (a) and (b) show a comparison between the calculated tube diameters of DWCNTs/C_{60} and DWCNTs/C_{70}, respectively. A closer inspection of Figure 4.9 (a) and (b) reveals that the average tubes diameters are 1.5 nm and 1.6 nm in the case of DWCNTs/C_{60} and DWCNTs/C_{70}, respectively.

Figure 4.10 (a) shows the HRTEM of the I-SWCNTs images under "normal" high-resolution low-voltage conditions. One can observe dark spots at the centre of the images from iodine atoms, especially at the upper part of the image where
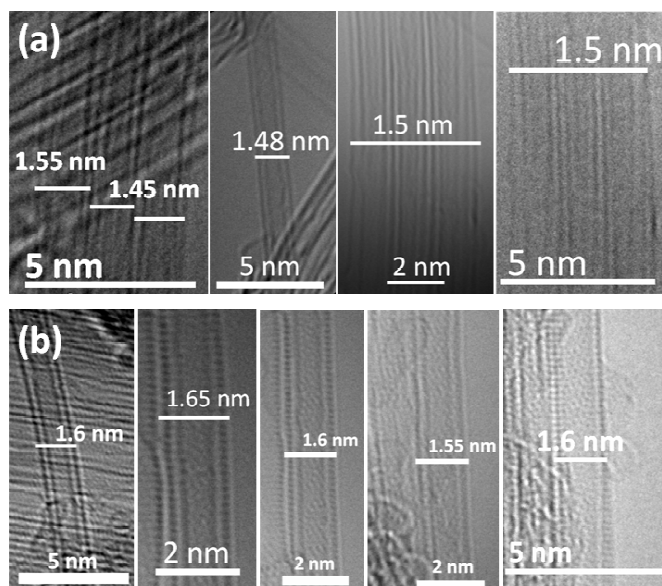
Figure 4.9: Calculated tube diameters of (a) DWCNTs/C_{60} and (b) DWCNTs/C_{60} from many single HETEM images.
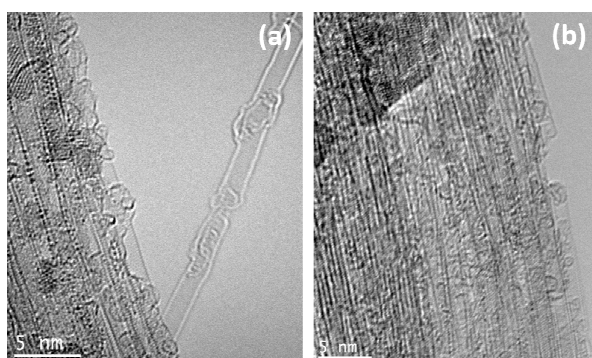
Figure 4.10: HRTEM of I-SWCNTs with two different magnifications.

one can clearly recognize a crystalline or at least order structure. Iodine is relatively heavy element compared to carbon and since the HRTEM works at low electron energies, so the contrast of the iodine atoms should be very clear. During the measurements, the energy-dispersive X-ray (EDX) spectra showed a very clear iodine signal. This means that, due to the low boiling point of iodine and the enlarged interaction cross section due to the low electron energies, the iodine atoms inside the nanotubes are readily evaporated and iodine atoms inside the carbon nanotubes would move too fast to be imaged. Because of this assumption, the electron beam dose was lowered with a factor of more than 1/200. The result can be seen in images Figure 4.10 (b). The image quality is not that high because of acquisition times of up to 100 s and small sample drift. Also very view dark

spots from iodine atoms can be observed inside the tubes. It is still possible that the iodine is evaporated inside the tubes. According to previous published data [119, 122], to visualize single atoms by HRTEM, a high performance CCD (1000 × 1000) detector with an efciency of 2 counts per electron is used for the image acquisition. A high signal-to-noise ratio of 3, corresponding to the condence level of 80% for the single-atom imaging. When the acquisition time is reduced down to 0.9 sec the electron beam irradiation damage of the sample will also reduced. So, it seems that it is tricky to image the iodine atoms inside the nanotubes using HRTEM. In next subsection 4.2.2, the filling of SWCNTs with iodine atoms will be proved using Raman spectroscopy.

4.2.2 Raman Spectroscopy

4.2.2.1 Raman Spectroscopy of Peapods

It has been demonstrated that filling of SWCNTs with molecules or atoms is expected to induce a certain shift in the RBM mode frequency. Previous Raman studies on C_{60} peapods [123–126], have been shown that the filling of thicker SWCNTs with C_{60} fullerene molecules shifts the RBMs to lower frequencies compared to the RBMs of the empty SWCNTs, while the RBMs are shifted to higher frequencies in the case of thinner tubes filling. These shifts can be explained as follows: starting with (10,10) SWCNTs which are the most energetically favourable nanotubes for the C_{60} filling [as discussed under the subsection 2.4]. Since the average tubes diameter of the (10,10) SWCNTs is 1.37 nm and the C_{60} molecule diameter is 0.71 nm [77], then the inter wall spacing between the C_{60} molecules and the SWCNTs wall is $\approx$ 0.33 nm. This value is consistent with the interlayer distance of graphite $\approx$ 0.335 nm [127], suggesting that the C_{60} molecules are tightly nested inside the nanotubes. This means that the C_{60}@(10,10) peapods are energetically stable but due to the space limitation the C_{60} molecules will hinder the motion of the C-C atoms and hence shift the RBMs modes to higher frequencies. In the case of thicker (11,10) and (11,11) SWCNTs, due to the relatively large empty space between the nanotube wall and the C_{60} molecules, electrons are transferred from the π-orbitals of the nanotubes to the empty space between them, forming the NFE state as shown in Figure 4.11 (a). Then, the
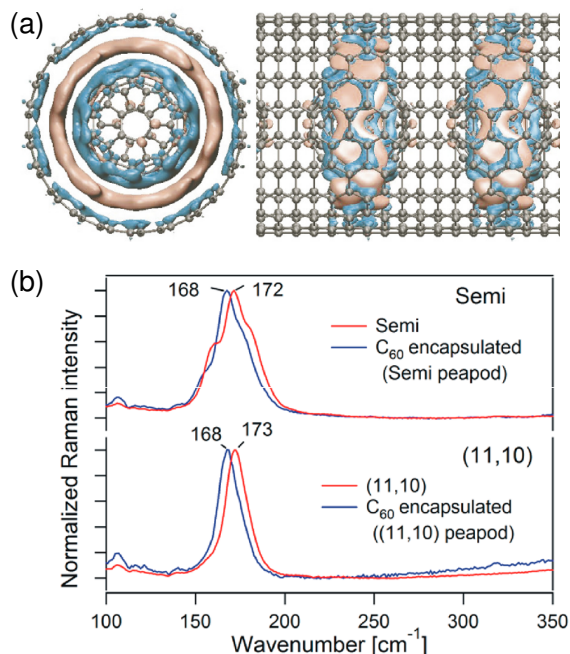
Figure 4.11: (a) Isosurfaces of the electron rich area, $\triangle\rho^-$ (pink isosurfaces), and that of the more positively charged area, $\triangle\rho^+$, (cyan isosurfaces) for the (11, 11) nanotube filled with and C_{60} [125]. (b) The changes of the RBM of the (11,10) caused by C_{60} filling (excitation wavelength of 514 nm) [128].

π and σ orbitals of the C_{60} molecules will hybridize with the NFE state. As a result, the electron density on the wall of the SWCNTs will decrease leading to the C-C bonds softening and hence shifting the RBMs to lower frequencies. Recently K. Yanagi *et al.* [128], isolated single chirality (11,10) SWCNTs from a mixture of different nanotubes chiralities after that the (11,10) nanotubes were filled with C_{60} molecules. The upper panel of Figure 4.11(b) shows the Raman spectra for a mixed state of several chiralities semiconducting SWCNTs with 1.44 nm average diameter before and after the C_{60} filling. The RBMs of the SWCNTs are composed of several peaks due to different chiralities. One can observe that after filling the peak centred at 172 cm^{-1} due to (11,10) chirality is shifted by 4 cm^{-1} to lower frequencies. The lower panel of Figure 4.11(b) shows only one sharp RBM of the single chirality (11,10) nanotubes at 173 cm^{-1}. After filling the RBM at 173 cm^{-1} was down shifted by 5 cm^{-1}. This was attributed to the charge transfer from the nanotubes which will soften the C-C bonds and hence shift the RBM to lower frequencies.

In this subsection the Raman spectra of C_{60}-peapods and C_{70}-peapods are shown. The spectra will be compared to the empty SWCNTs and also to the
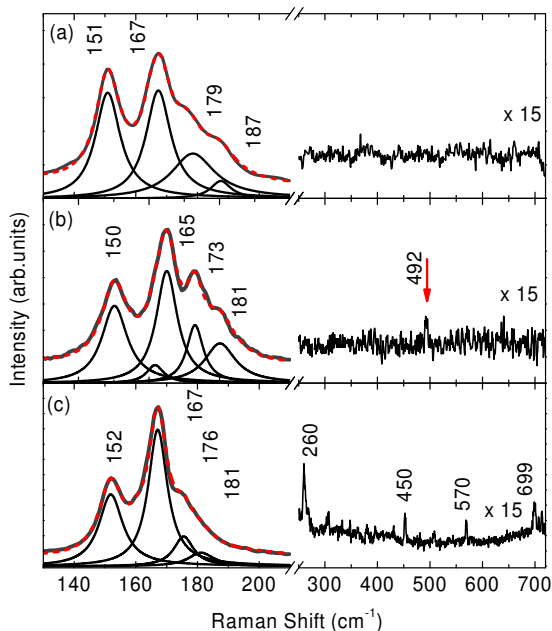
Figure 4.12: Raman spectra recorded with a 515 nm excitation wavelength of the RBM for (a) SWCNTs, (b) C_{60} peapods and (c) C_{70} peapods. In the frequency range 400-700 cm^{-1}, the weak mode at $\sim$ 492 cm^{-1} in (b) corresponds to the radial symmetry mode $A_g(1)$ of the C_{60} molecules and the Raman modes in (c) corresponds to the symmetry mode $A_1^{'}$ of the C_{70} molecules. Raman spectra in the range 400-700 cm^{-1} were multiplied by a factor of 15. The dashed-red line is a fit to the data with Lorentzian functions. The Lorentz contributions are shown as well.

previously published data.

Figure 4.12 shows the Raman spectra of the (a) SWCNTs, (b) C_{60}-peapods, and (c) C_{70}-peapods in the low frequency range between 120-240 cm^{-1}. For all samples, the RBMs of the primary tubes (outer tubes) can be observed. The peaks range from 150-187 cm^{-1}. To specify the contribution of the outer tubes, the spectra were fitted using Lorentzian function and the outer tubes diameters were calculated from equation 2.27. The calculated values of the SWCNTs diameters are in the range from 1.30-1.55 nm with average tube diameter of 1.41 nm. As shown in Figure 4.12 (b), the RBMs of the C_{60}-peapods are shifted by a small amount $\sim$ 1-6 cm^{-1} towards lower frequencies. This shift is not considered as an increase in the SWCNTs diameters due to the C_{60} molecules encapsulation but due to the charge transfer between C_{60} molecules and the walls of the SWCNTs [123]. With average tubes diameter of 1.41 nm and 0.71 nm diameter of C_{60} molecule, then the free space between the nanotube wall and the C_{60} molecule is $\approx$0.35 nm. This value is slightly higher than the interlayer distance of graphite $\sim$ 0.335 nm, suggesting that the free space between the C_{60} molecules and the wall of the nanotube is enough to generate the NFE between them. According to the previous discussion, the charge transfer from the nanotubes induces the C-C

bonds softening and hence shifting the RBMs to lower frequencies. In our earlier work [129], we observed that the filling of SWCNTs with C_{60} molecules induces a blue-shift of the RBMs due the C-C radial motion hindrance. This discrepancy could be attributed to the excitation wavelength used: In Ref. [129] we used a 488 nm laser line for excitation, which enhances the RBMs of the small-diameter carbon nanotubes [47]. In the case of C_{70}-peapods [see Figure 4.12 (c)], one can observe that the RBMs of the nanotubes are not affected by the encapsulation of the C_{70} molecules.

This could be explained as follows: According to previous HRTEM study on C_{70}-peapods, the ellipsoidal C_{70} molecules are arranged in transverse (standing) position (with the 0.792 nm axis) for $\sim$ 1.49 nm diameter nanotubes and in longitudinal (lying) position (with the 0.691 nm axis) for nanotubes with diameter $\sim$ 1.36 nm [130]. According to Verberck *et al.* [131, 132], the critical nanotube diameter for the C_{70} filling in the longitudinal (lying) position is 1.37 nm and for the transverse (standing) position is 1.44 nm. The nanotubes diameters between the 1.37 and 1.44 nm, the C_{70} molecules are arranged in a titled position. Since the SWCNTs used in the present work have diameters distribution in the range of 1.30 to 1.55 nm, we can assume that a large fraction of the C_{70} peapods are filled with C_{70} molecules in the transverse (standing) position. This assumption is in agreement with a high-pressure Raman study on C_{70}-peapods [133], where the flipping of the C_{70} molecules from the transverse to the longitudinal position was observed at $\approx$ 1.5 GPa. Since the hybridization between the fullerene molecules and the nanotube wall depends on the free space between them, we will try to roughly estimate the free space in our C_{70}-peapods and compare it with that of the C_{60}-peapods. In the transverse position, the free space between C_{70} and the tube is 1.4 nm - 0.792 nm = 0.608 nm, so the free space in our C_{70}-peapods is comparable to that in 1.31 nm diameter SWCNTs filled with C_{60} molecules. According to Rochefort [67], the 1.3 nm SWCNT filled with C_{60} molecules is energetically stable but not the ideal case for the hybridization between the NFE states of the nanotube wall and the C_{60} states. This behaviour signals that a possible charge transfer between C_{70} molecules and the SWCNT wall is too small to lead to significant shifts in the RBMs.

In the frequency range 250-700 cm^{-1} no significant Raman features are ob-

served for the empty SWCNTs. In case of the C_{60} peapods [see Figure 4.12 (b)], one can observe the weak Raman radial symmetry mode $A_g(1)$ of the C_{60} molecules at 492 cm^{-1} (indicated by small arrow) [123, 134]. The vibrational frequency of this mode is downshifted by $\sim$ 4 cm^{-1} as compared with the C_{60} solid as shown in Figure 4.13 (a), where the C_{60} solid radial symmetry mode $A_g(1)$ is observed at $\sim$ 496 cm^{-1} [135]. The softening of this mode is due to the formation of linear chain (like polymerization) between the C_{60} molecules inside the SWCNTs cavity, since the intermolecular distance between the C_{60} molecules was found to be 0.97 nm, shorter than the intermolecular distance 1.0 nm in the fcc crystal [136]. The appearance of the $A_g(1)$ mode is an indication for the high filling of the SWCNTs with the C_{60} molecules [137, 138]. In the case of C_{70} peapods, one can observe the appearance of new Raman active peaks [see Figure 4.12 (c)]. These new peaks are due to the $A_1^{'}$ of the C_{70} molecules Raman active mode at 260, 450, 570, and 699 cm^{-1} [134, 139, 140]. The appearance of these peaks with relatively high intensities is a good indication for the high filling of the C_{70} peapods [137, 138]. Compared to the Raman spectra of C_{70} solid [see Figure 4.13 (b)], one can observe that the vibrational frequencies of these modes are downshifted by $\sim$ 1-5 cm^{-1}. The softening of the C_{70} modes could be attributed to the formation C_{70} molecules chain inside the SWCNTs cavity. The low intensities of the C_{60} and C_{70} modes in the case of C_{60} and C_{70} peapods, respectively, compared to the intensities of C_{60} and C_{70} solid, indicate that all the fullerene molecules are encapsulated inside the nanotubes and there are no molecules outside the SWCNTs which signals the high purity of the prepared peapods samples.

Figure 4.14 shows the tangential mode region of (a) SWCNTs, (b) C_{60}-peapods, and (c) C_{70}-peapods. In the frequency range 1200-1500 cm^{-1} only the D-mode at 1348 cm^{-1} is observed for the SWCNTs. In contrast, in the case of C_{60} peapods, additional to D-mode at 1348 cm^{-1}, the Raman-active mode $A_g(2)$ of the C_{60} molecules at 1469 cm^{-1} is observed. The average integrated intensity ratio $A_g(2)$/G-mode = 2×10^{-3} suggests the high filling ratio of the peapods [137, 138]. For the C_{70}-peapods, in addition to the D-mode, new Raman-active modes can be observed at 1226, 1259, 1446 and 1470 cm^{-1} (indicated by small arrows) due to the $E_1^{''}$, $E_2^{'}$, $E_1^{''}$ and $A_1^{'}$, respectively, of the C_{70} molecules [134, 139, 140].
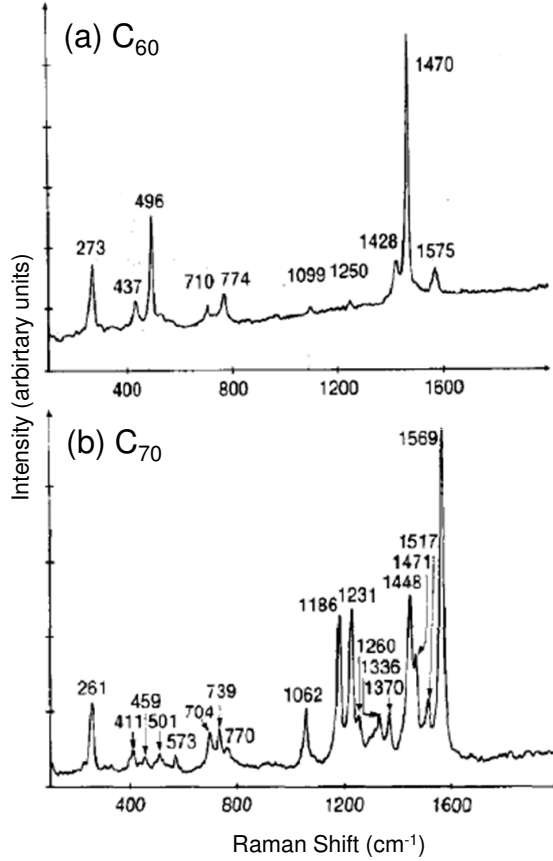
Figure 4.13: Raman spectra of film of purified (a) C_{60} and (b) C_{70} fullerenes [135].

The average integrated intensity ratios between E_1'', E_2', E_1'', A_1' and G-mode are 9.5×10^{-3}, 9.0×10^{-3}, 15.0×10^{-3} and 13.0×10^{-3}, respectively, indicating the high filling ratio of the C_{70} peapods [137, 138]. In general, the high intensities ratio of the Raman active modes in the case of C_{70}-peapods compared to the C_{60}-peapods [see Figures 4.12 and 4.14], is not an indication of the high filling of the C_{70}-peapods but due to the relatively large number of the intratubular C-atoms in the C_{70}-peapods compared to the number in the C_{60}-peapods [141].

In the high frequency range 1500-1650 cm^{-1} the G mode is observed for all samples. In the case of SWCNTs the band centered at 1595 cm^{-1} is related to the G^+ peak, which is mainly due to the $A_1^{LO}(S)$ longitudinal mode of the semiconducting primary tubes [142, 143]. The lower frequency bands appeared at 1555, 1569 and 1576 cm^{-1} are due to the the G^- peak. The 1555 cm^{-1} is ascribed to $E_2^{LO}(M,S)$ longitudinal mode of the metallic and semiconducting tubes [144]
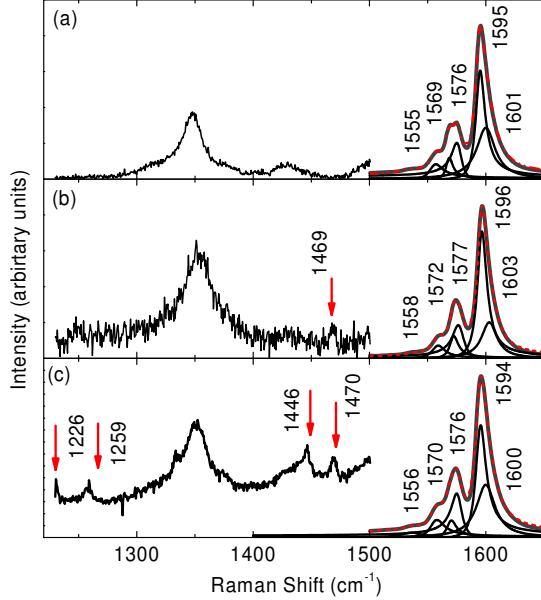
Figure 4.14: Raman spectra recorded with a 515 nm excitation wavelength of the G-mode for (a) SWCNTs, (b) C_{60} peapods, and (c) C_{70} peapods. The Raman mode at 1496 cm^{-1} in (b) corresponds to the symmetry mode $A_g(2)$ of the C_{60} molecules. The Raman-active modes at 1226, 1259, 1446 and 1470 cm^{-1} in (c) corresponds to the E_1'', E_2', E_1'' and A_1', respectively, of the C_{70} molecules. Raman spectra in the range 1200-1500 cm^{-1} were multiplied by a factor of 40. The dashed-red line is a fit to the data with Lorentzian functions. The Lorentz contributions are shown as well.

and the two band at 1569 and 1576 cm^{-1} are due to A_1^{TO}(S,M) transverse mode of the semiconducting and metallic tubes, respectively. The extra peak around 1601 cm^{-1} originates from the E_2^{TO}(M,S) modes [142–144]. For the C_{60}-peapods [Figure 4.14 (b)], the three components of the G^- mode are blue shifted by 1-3 cm^{-1}), while no significant shift is observed for the G^+ component at 1996 cm^{-1}. It is well known that the G^+ components originate from the carbon atoms vibrating along the nanotube axis, while the G^- components originate from the carbon atoms vibrating along the tubes circumference [45]. This means that the radial overlapping between the π states of SWCNTs and C_{60} molecules will hinder the vibrations of carbon atoms along the circumference of the tubes and hence shifts the G^- components up. In contrast, in the case of C_{70}-peapods, the G mode components appear at the same positions as in the SWCNTs, which means that the charge transfer between the C_{70} molecules and the outer tube seems to be too small to be observed in the Raman data [56].

4.2.2.2 Raman Spectroscopy of DWCNTs

Figure 4.15 shows the Raman spectra of (a) SWCNTs, (b) DWCNTs/C_{60}, and DWCNTs/C_{70} in the low frequency range 120-240 cm^{-1}. For all the samples,
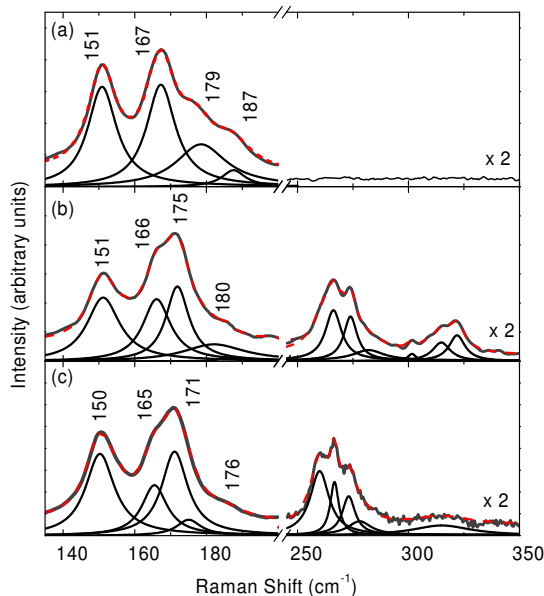
Figure 4.15: Raman spectra recorded with a 515 nm excitation wavelength of the RBM for (a) SWCNTs, (b) DWCNTs/C_{60}, and (c) DWCNTs/C_{70}. The excitations lines in the frequency range 230-350 cm^{-1} in (b) and (c) correspond to the RBM of the inner tubes of the DWCNTs/C_{60} and DWCNTs/C_{70}, respectively. Raman spectra in the range 230-350 cm^{-1} were multiplied by a factor of 2. The dashed-red line is a fit to the data with Lorentzian functions. The Lorentz contributions are shown as well.

the RBMs for the primary tubes (outer tubes) can be observed. The peaks range from 150-178 cm^{-1}. To specify the contribution of the outer tubes, the spectra were fitted using Lorentzian function. The outer tubes diameters were calculated from equation 2.27. Compared to the SWCNTs, the RBMs in the case of DWCNTs/C_{60} and DWCNTs/C_{70} are shifted towards lower frequencies by 5-7 cm^{-1} and 1-10 cm^{-1}, respectively. The peaks positions and the calculated tubes diameters for the DWCNTs/C_{60} and the DWCNTs/C_{70} are listed in Table 4.1. One can observe that, in the case of DWCNTs/C_{60}, the diameters of the outer walls are in the range of 1.36-1.56 nm, with an average tubes diameter of 1.43 nm and for the DWCNTs/C_{70}, the diameters of the outer walls are in the range of 1.37-1.56 nm, with an average tubes diameter of 1.45 nm. The downshift of the RBMs and the corresponding slight increase in the outer tubes diameters compared to the SWCNTs can be attributed to the tubes fattening [see section 2.5] with the long heat treatments (1250°C and 24 hrs) via several Stone-Wales transformation on the SWCNTs surface [73, 74].

In the frequency range 240-350 cm^{-1}, compared to the SWCNTs, several new peaks with quite low intensity in the case of DWCNTs/C_{60} and DWCNTs/C_{70} are observed [see Figure 4.15]. These new peaks are associated with the small E_{22}^S semiconducting secondary tubes with $\sim$ 0.7-0.8 nm [56, 123]. The 512 nm

Table 4.1: Raman peak positions and tubes diameters estimated from the RMB frequencies of the SWCNTs, DWCNTs/C_{60} and DWCNTs/C_{70} (outer and inner tubes). The tubes diameters were calculated from $d=234/(\omega_r)$, where d is the tube diameter (nm) and ω_r, the RBM frequency (cm^{-1}).

	SWCNTs		DWCNTs/C_{60} outer tubes		DWCNTs/C_{60} inner tubes	
	ω_r cm^{-1}	d nm	ω_r cm^{-1}	d nm	ω_r cm^{-1}	d nm
	151	1.55	150	1.56	266.2	0.87
	167	1.40	166	1.41	273.8	0.85
	179	1.30	172	1.36	282.2	0.83
					314.8	0.74
					332.0	0.72
Average		1.41		1.43		0.8
	SWCNTs		DWCNTs/C_{70} outer tubes		DWCNTs/C_{70} inner tubes	
	151	1.55	150	1.56	260.0	0.90
	167	1.40	165	1.42	266.7	0.87
	179	1.30	171	1.37	273.3	0.85
					278.0	0.84
					315.0	0.74
Average		1.41		1.45		0.85

excitation is unsuitable for secondary tubes resonant enhancement, so quite low intensity is expected [56, 145]. According to equation 2.27, the values for the inner tubes' diameters amount to 0.72-0.87 nm with average tubes diameter of 0.8 nm in the case of DWCNTs/C_{60} and 0.74-0.9 nm with average tubes diameter of 0.85 nm in the case of DWCNTs/C_{70}. These values are higher than the diameter of the parent fullerene molecules (0.71 and 0.792 nm for C_{60} and C_{70}, respectively). This difference could be attributed to the tubes fattening due to the long heat treatment; where at the beginning the formed inner tubes have diameters equal to the C_{60} or the C_{70} molecules diameter and with long heat treatment, tubes with larger diameters are grown by the transformation of the diameters by several Stone-Wales transformation [73, 74, 129]. The peak positions and the calculated tube diameters values of the outer and inner tubes in the case of SWCNTs, DWCNTs/C_{60} and DWCNTs/C_{70} are listed in Table 4.1. From Table 4.1, one can observe that the average outer and inner tubes diameters in the case of

DWCNTs/C_{70} is slightly higher than the average of the DWCNTs/C_{60}. This behaviour is consistent with HRTEM data [see subsection 4.2.1] and with the previously published data [141].

Figure 4.16 shows the G-mode region of (a) SWCNTs, (b) DWCNTs/C_{60}, and (c) DWCNTs/C_{70}. In the frequency range 1200-1500 cm^{-1} only the D-mode is observed for the all samples under investigation. Compared to the SWCNTs, the D-mode was splitted into two modes at 1318 and 1349 cm^{-1} in the case of DWCNTs/C_{60} and to 1318 and 1351 cm^{-1} in the case of DWCNTs/C_{70}. The peaks at lower frequencies are attributed to the small diameters inner tubes $\sim$ 0.7-0.8 nm and the peaks are higher frequencies are attributed to the outer tubes [60]. One can observe that in the case of DWCNTs/C_{70}, the D-mode of the outer tube is shifted by 4 cm^{-1} compared to the the SWCNTs and by 1 cm^{-1} compared to the DWCNTs/C_{70}. As discussed in the subsection 2.3.3.4, the D-band shows a dependence on the nanotube diameter, it increases with increasing the diameter according to Equation 2.29. This means that the outer tubes in the case DWCNTs/C_{70} is larger than the outer tubes of both DWCNTs/C_{60} and the empty tubes. This is also in consistent with the results obtained from the RBM calculation. In the high-frequency range 1500-1650 cm^{-1} for both DWCNTs/C_{60}, and (c) DWCNTs/C_{70} [Figure 4.16 (b) and (c)], the three components of the G mode appear at the same positions compared to the SWCNTs, which means that the charge transfer or the interaction between the inner and outer tubes seems to be too small to be observed in the Raman data [56].

4.2.2.3 Raman Spectroscopy of Metallic Tubes

According to the carbon nanotubes Raman map in Ref. [145], the 2.4 eV (515 nm) laser excitation enhances the Raman resonance of the outer tubes with E_{33}^{S} and E_{44}^{S} transitions and only very view families of the inner tubes with E_{22}^{S} transitions. In the case of 1.83 eV (676 nm) the outer tubes with families 30 and 33 resonate with E_{11}^{M} transition and inner tubes of family 19 resonate with E_{22}^{S} transition [143, 145]. Now the 1.83 eV (676 nm) laser excitation will be used to study the behaviour of the metallic tubes in all samples under investigation. Figure 4.17 (a) shows the tangential mode region of the empty SWCNTs recorded with
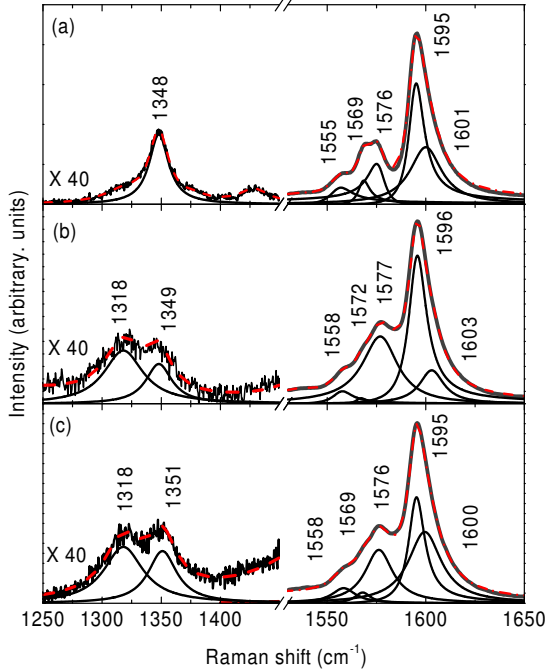
Figure 4.16: Raman spectra recorded with a 515 nm excitation wavelength of the G-mode of (a) SWCNTs, (b) DWCNTs/C_{60}, and (c) DWCNTs/C_{70}. Raman spectra in the range 1200-1500 cm^{-1} were multiplied by a factor of 40. The dashed-red line is a fit to the data with Lorentzian functions. The Lorentz contributions are shown as well.

a 676 nm excitation wavelength. In the case of 515 nm excitation wavelength [see Figures 4.14 and 4.16], the G-mode was represented well by superposition of many Lorentzian oscillators of the semiconducting tubes but with the 676 nm excitation wavelength, the G-mode is well fitted by the superposition of two different lines: two Lorentzian components and a symmetric BWF component [see equation 2.28]. From the Raman map of the DWCNTs [145] the peak centred at 1593 cm^{-1} is due to the G$^+$ component and matches only the large primary semiconducting tubes via the E_{33}^S. The asymmetric BWF line shape is assigned to the G$^-$ component of the primary metallic tubes. Figure 4.17(b) and (d) shows the the tangential mode of C_{60} and C_{70} peapods, respectively. No significant change in the peak position of both G$^+$ and G$^-$ components which indicates that the G mode does not change significantly with the presence of fullerene molecules. In the case of both DWCNTs/C_{60} and DWCNTs/C_{70} [see Figure 4.17(c) and (e)], a new Lorentzian band centred at a round 1582 and 1583 cm^{-1} in the case of DWCNTs/C_{60} and DWCNTs/C_{70}, respectively. This band could be assigned to the inner semiconducting tubes with $d \approx$ 0.8 nm with E_{22}^S transitions.
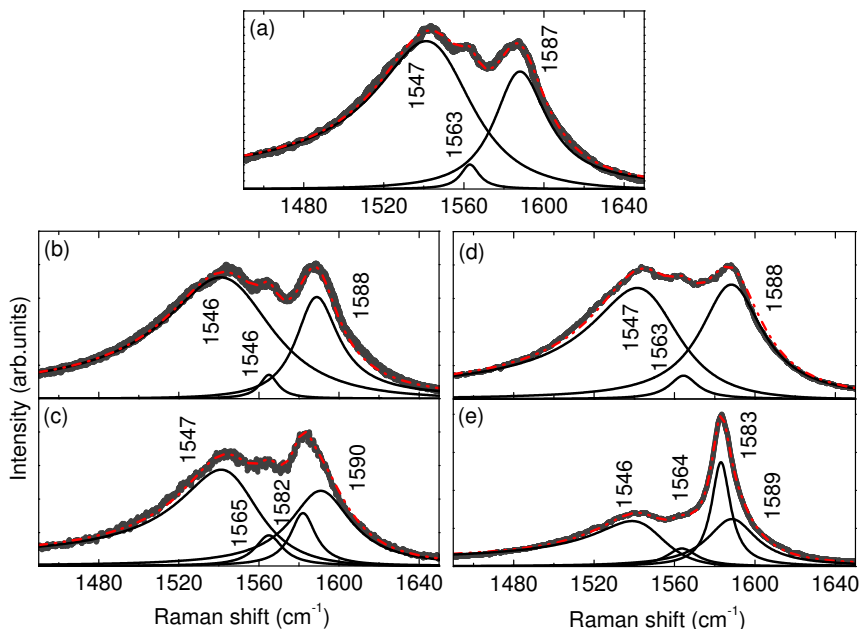
Figure 4.17: Raman spectra recorded with a 676 nm excitation wavelength of the G-mode for (a) SWCNTs, (b) C_{60}-peapods, (c) DWCNTs/C_{60}, (d)C_{70}-peapods, and (e) DWCNTs/C_{70}. The asymmetric Breit-Wigner-Fano (BWF) line shape centred at around 1547 cm^{-1} is assigned to the G^{-} component of the primary metallic tubes. The dashed-red line is a fit to the data with Lorentzian functions. The Lorentz and (BWF) contributions are shown as well.

4.2.2.4 Raman Spectroscopy of I-SWCNTs

Figure 4.18 shows the Raman spectra of (a) SWCNTs and (b) I-SWCNTs in the low frequency range 120-400 cm^{-1}. The peak at 176 cm^{-1} and its overtones at 331 and 351 cm^{-1} in (b) originate after the encapsulation of iodine atoms inside the SWCNTs. Wang *et al.* [146] observed a Raman active mode at 174 cm^{1} for I-SWCNTs excited by 514.5 nm. To clarify the origin of this band, they performed a density functional theory (DFT) calculations for the vibrational properties of the isolated I_3^-, I_5^-, and I_7^- polyiodide chains. From the DFT calculations the expected Raman-active frequencies are 95.6, 148.8, and 152.4 cm^{1}, respectively. Due to the similarity in the peak position of the I_5^- and I_7^- Raman bands, Wang *et al.*, attributed the appearance of the peak at 174 cm^{1} to the two polyiodides. The deviation between the experimental and theoretical values could be attributed to the interaction between the SWCNTs and the iodine chains. Accordingly, we

81
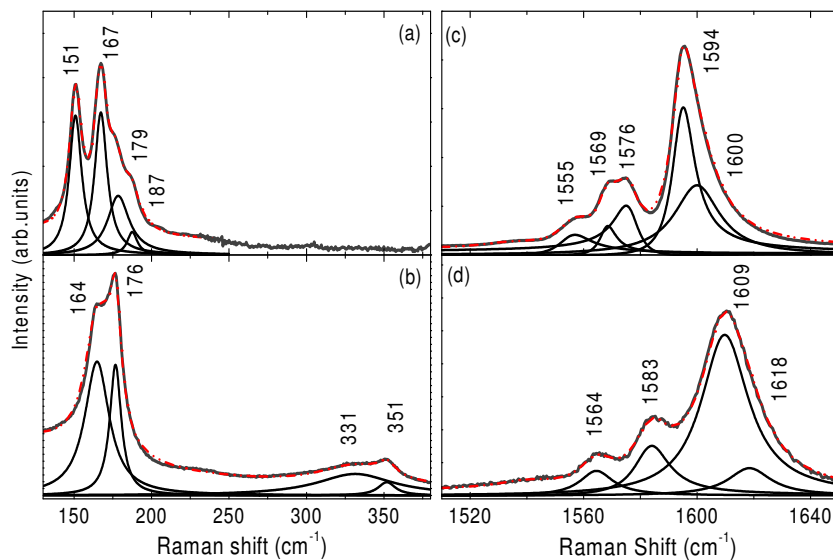
Figure 4.18: Raman spectra recorded with a 515 nm excitation wavelength of the RBM mode for (a) SWCNTs and (b) I-peapods. The peak at 176 cm^{-1} and its overtones at 331 and 351 cm^{-1} in (b) originate from the charged polyiodine chains. The G-mode of SWCNTs and I-peapods appears in (c) and (d) respectively. The dashed-red line is a fit to the data with Lorentzian contributions are shown as well.

interpret the peak at 176 cm^1 due to the presence of the two polyiodide chains I$_5^-$ and I$_7^-$ inside the SWCNTs. One can observe also that the RBM of the SWCNTs at 151 cm^{-1} is shifted to higher frequencies by 13 cm^{-1}. This could be attributed to the C-C bonds stiffening due to the removal of the electrons from the SWCNTs walls by hole doping [123]. Figure 4.18 shows the G-mode region for (c) SWCNTs and (d) I-SWCNTs. As discussed in the subsection 4.2.2.1, the two components G$^+$ and G$^-$ of the G-mode in the case of SWCNTs are observed. For I-SWCNTs, the G lines are upshifted by $\approx$ 9-18 cm^{-1} compared to the empty SWCNTs. This could be attributed to the electrons transfer from the SWCNTs to the iodine molecules, generating negatively charged polyiodine chains [146]. From the electrochemical doping study of SWCNTs, the G mode was found to be upshifted by 320 cm^{-1} per hole per C atom added to the π-band of the SWCNTs [147].
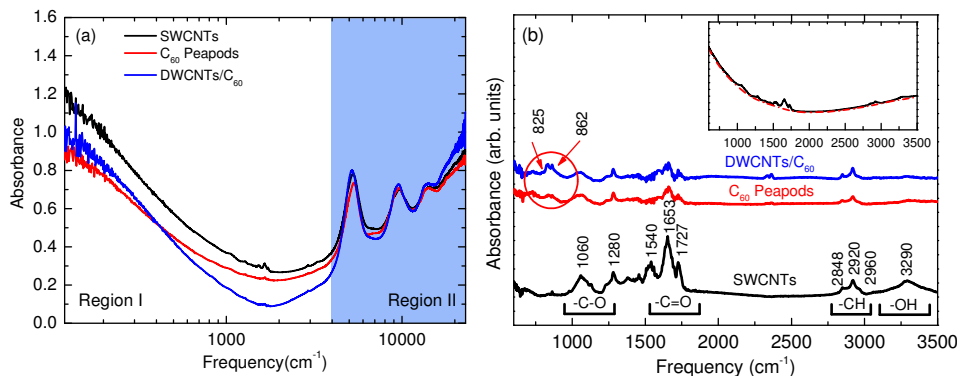
Figure 4.19: (a) Absorbance spectra of SWCNTs, C_{60}-peapods, and DWCNTs/C_{60}. Region I is the frequency range of the low-energy excitations while Region II corresponds to the optical transitions range. (b) Absorbance spectra of SWCNTs, C_{60}-peapods, and DWCNTs/C_{60} in the MIR region after the back-ground subtraction with polynomial function (dashed red line) as shown in the inset of (b). The horizontal bars at the bottom of (b) identify the typical frequency intervals for different IR active modes for the specified chemical groups.

4.2.3   Infrared and Optical Spectroscopy

In this section the optical properties of all sample under investigation in this work will be discussed in details. All the samples are in the form of free-standing films [the preparation method of the free-standing was discussed under the subsection 3.4]. The optical properties of the free-standing films will be studied in a wide frequency range from the FIR to the VIS region. The discussion will be divided to two parts: (i) FIR-MIR region and (ii) NIR-VIS region.

4.2.3.1   FIR-MIR Infrared Spectroscopy

Figure 4.19 (a) shows the infrared absorption spectra on a wide frequency scale from the FIR to the VIS range for SWCNTs, C_{60} peapods, and DWCNTs/C_{60} free-standing films. Between 4000-22000 cm^{-1} (Region II), the optical transitions S_{11}, S_{22} and M_{11} are observed. These transitions will be discussed in detail in the subsection 4.2.3.2. In the frequency range 4000-100 cm^{-1} (Region I), for all the samples under investigation the broad MIR and FIR electronic absorption continuum is observed. The strong absorption in the FIR region could be attributed to the free-carriers absorption in the metallic tubes. The SWCNTs used in this

project are commercial nanotubes prepared by the arc-discharge method and nitric acid was used during the purification process of the tubes. Using strong acids during the purification causes a hole doping of the SWCNTs and hence increases the free-carriers which contribute to the FIR absorption [148–150]. One can also observe that the infrared absorption in the FIR is broad. This could be explained as follows: scanning electron microscopy images showed that the free-standing film of SWCNTs prepared by using the suspension method have a spaghetti-like morphology, with curved, sinuated, and crossed bundles [151]. This inhomogeneous structure will create defects states between the conduction and valence bands of the nanotubes which might cause a notable broadening of the FIR absorption [152]. One notices that in MIR and FIR regions, the C_{60}-peapods and DWCNTs/C_{60} share the same feature as the SWCNTs. Here, we can not quantitatively analyze the MIR and FIR band because the samples under investigations have different thicknesses because they were prepared from different patches. The inset of Figure 4.19 (b) shows relatively weak IR-active modes hardly seen on the absorption spectrum of the SWCNTs. We used the cubic polynomial function [dashed red line in the inset of Figure 4.19 (b)] to subtract the background in order to enhance the visibility of such weak peaks. The subtracted background spectra for SWCNTs, C_{60} peapods, and DWCNTs/C_{60} are shown in Figure 4.19(b). For SWCNTs, the broad band centred at 3290 cm^{-1} is ascribed to the OH stretching mode. The origin of this mode could be ascribed to the carboxylic acid groups attached to the SWCNTs walls during the purification process. The triplet at $\approx$ 2848, 2920, and 2960 cm^{-1} are assigned to the C-H$_n$ functional groups. The band at $\approx$ 1727 cm^{-1} is due to the C=O stretching vibration. The two bands at $\approx$ 1653 and 1280 cm^{-1} are ascribed to the NO$_2$ asymmetric and symmetric vibrations, respectively. The presence of the NO$_2$ groups attached to the walls of the SWCNTs could be due to the purification process or the presence of some cellulose nitrate from the filtration membrane during the free-standing films preparation [as disused under subsection 3.4]. The band at $\approx$ 1060 cm^{-1} could be assigned to the C-O stretching vibration [153, 154].

In the case of C_{60}-peapods and DWCNTs/C_{60} we can observe that some bands are completely removed and the others are reduced in strength. This is because the preparation of the peapods and DWCNTs requires high temperature and high

vacuum treatment [as discussed under the subsection 4.1.2]. The intensity of the C-H$_n$ triplet is almost the same compared to the SWCNTs. This triplet may be due to hydrocarbons contamination in the spectrometer. The most interesting observation is the appearance of the two modes at 825 and 862 cm^{-1} [marked with red circle] in the case of C$_{60}$-peapods and DWCNTs. These two modes are carbon nanotubes IR-active modes and assigned to the first order E$_1$ and A$_1$ symmetry, respectively [153]. These IR-active modes are due to the dynamic dipole moment because SWCNTs do not support the static dipole moment [153]. According to previous infrared spectroscopy studies on the SWCNTs [155, 156], the treatment of the SWCNTs at 1100°C under dynamic vacuum should remove most of hydrocarbons groups attached to the surface of the SWCNTs, so the appearance of theses two modes in the case of DWCNTs is believed to be due to the high temperature ($\approx$ 1250°C) and high vacuum treatment used during the sample preparation which removed most of the organic groups attached to the walls of the tubes [153]. According to Ref.[153], it is possible to see about 18 IR-active modes after the purification of the SWCNTs under high vacuum and high temperature $\approx$ 1400°C. Therefore, with careful purification of the samples more IR-active modes will be seen and this will give in the future the possibility to study the effect of high pressure on the SWCNTs IR-active modes. In Ref. [157] the authors discussed the coupling between some IR-modes with the electron in this region. One of the outlooks of this work is to extend the high pressure study on the behaviour of the IR-active modes using hydrostatic pressure transmitting medium.

Figure 4.20 (a) shows the infrared absorption spectra on a wide frequency scale from the FIR to the VIS range for the free-standing film of SWCNTs, C$_{70}$-peapods, and DWCNTs/C$_{70}$. Figure 4.20 (b) shows the infrared absorption spectra for the SWCNTs and I-SWCNTs in the FIR to the VIS range. In Region I, for all the samples under investigation the broad FIR and MIR electronic absorption continuum is observed. The above described analysis is also applied to the infrared absorbance spectrum of all samples. The background-subtracted absorbance spectra for the samples under investigation in Figure 4.20 (a) and (b) are not shown because they will share the same feature discussed under the subsection 4.2.3.1. From the above discussion, the filling of the SWCNTs with
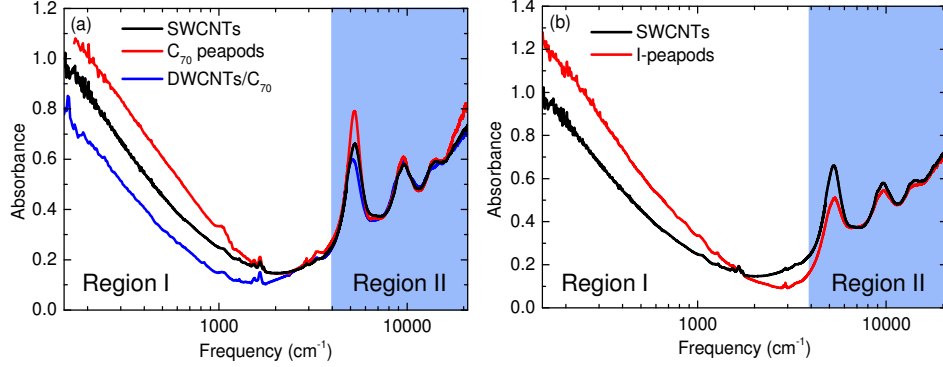
Figure 4.20: (a) Absorbance spectra of SWCNTs, C_{70}-peapods, and DWCNTs/C_{70}. Region I is the frequency range of the low-energy excitations while Region II corresponds to the optical transitions range. (b) Absorbance spectra of SWCNTs and I-SWCNTs. Region I is the frequency range of the low-energy excitations while Region II corresponds to the optical transitions range.

C_{60}, C_{70}, iodine or inner tubes can not compared quantitatively in the MIR and FIR region because all the samples under investigations have different thicknesses because they were prepared from different patches as discussed above.

4.2.3.2 NIR-VIS Optical Spectroscopy

Figure 4.21 shows the optical absorption spectrum of the SWCNTs between 4000-22000 cm^{-1} (Region II). Several pronounced absorption bands are observed on the top of a broad background centred at around 5 eV, which is due to the π-π^* electronic interband transition of the graphene sheet. The background was estimated by a linear function. The optical absorption spectrum before and after the background substraction is shown. The bands labeled as S_{ii} and M_{ii}, correspond to the ith optical transitions in the semiconducting and metallic tubes, respectively.

Figure 4.22 (a) shows the background-subtracted absorbance spectrum of SWCNTs. In general the spectrum is characterized by four broad absorptions bands at $\approx$ 0.65, 1.2, 1.8, and 2.2-2.6 eV. The S_{11}, S_{22}, and $S_{33/44}$ bands are due to the first, second, and higher optical transitions in the semiconducting tubes. The band centred at $\approx$ 1.8 eV is assigned to the first optical transition, M_{11}, in

Figure 4.21: Absorbance spectrum for the SWCNTs film together with the linear background (dashed red line) and the absorbance spectrum aft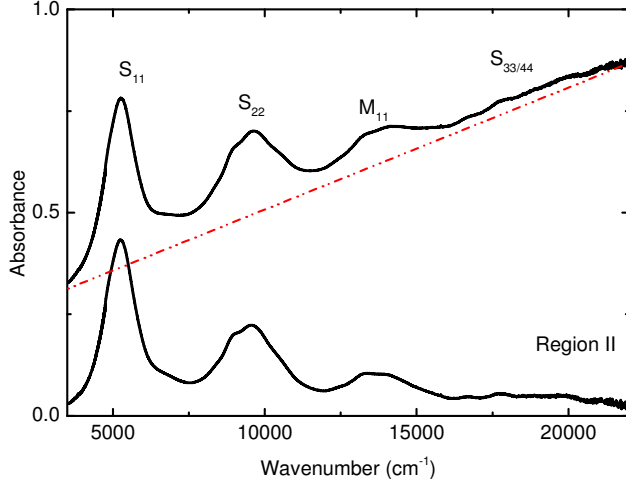er background subtraction. The labels S_{ii} and M_{ii} denote the i*th* optical transition in semiconducting and metallic tubes, respectively.

the metallic tubes. The optical transitions exhibit a fine structure, which reflects the nanotube diameter distribution in the sample. Kataura *et al.* [37] showed that the energy differences (E_{ii}) between the vHS peaks have a width in energy and this width depends on the nanotube chirality. The nanotubes with the same diameter but with different chiralities have a wide width of energy distribution between the vHS. The observed width of the peak positions in the resonant Raman spectra for SWCNTs is consistent with the width in the optical absorption data [31]. The spread of the optical absorption bands is large for the higher energies compared to the lower energies, i.e., $M_{11} > S_{22} > S_{11}$. This behaviour was attributed to the trigonal warping effect [see subsection 2.3.2.1], where the equi-energy contours are circular around the K-point but near the zone boundary the contours are triangular. Therefore, all the absorption bands were fitted with several Lorentzian oscillators to describe each band. By fitting the absorption bands, all the frequencies of various contributions are listed in Table 4.2.

The above-described analysis was also applied to the optical absorbance spectrum of the free-standing C_{60}-peapods and DWCNTs/C_{60}. The background-subtracted spectra together with the fitting curve and the various Lorentz terms are shown in Figure 4.22(b) and (c)]. The extracted frequencies of the Lorentz oscillators are included in Table 4.2. In C_{60}-peapods all the Lorentzian contributions are slightly shifted to higher energies, and in DWCNTs/C_{60} all contributions are slightly shifted to lower energies compared to the corresponding features in

Figure 4.22: Background-subtracted absorbance spectra of (a) SWCNTs, (b) C_{60} peapods, and (c) DWCNTs/C_{60} together with the fit of the absorption bands using Lorentzian oscillators.The vertical,dashed line marks the position of the S_{11} band in SWCNTs.

SWCNTs (see Table 4.2). In the case of peapods, a hybridization between the NFE state and the t_{1u} state of the C_{60} is expected, since the average tube diameter is nearly equal to the critical value at which the hybridization starts. In this case, the hybridization is expected to reduce the effective tube diameter, and hence the optical absorption bands are blue-shifted [63, 64]. In case of the DWCNTs/C_{60}, due to the fattening of the tubes with long heat treatment the effective tube diameters will increase [74], and hence the absorption bands will be shifted to lower energies according to the Kataura plot [37].

Since the average inner and outer tubes diameters of the DWCNTs/C_{60} are ≈ 0.7 and 1.4 nm, respectively, then from Equation 2.24, the S_{11} and S_{22} optical transitions are expected to be at around ≈ 0.6 eV and 1.2 eV, respectively for outer tubes and for inner tubes at around ≈ 1.2 eV and 2.4 eV. This means that the region between 1 and 1.5 eV [see Figure 4.22 (c)] consists of an overlap between the S_{22} optical transitions of the outer tubes and S_{11} optical transitions of the inner tubes. Similarly, the region between 1.5 and 2.3 eV can overlap the M_{11} optical transitions of the outer tubes and S_{22} optical transitions of the inner tubes. Satio *et al.* [158–160] have studied the electronic band structure of the

Table 4.2: Peak-position frequencies (in cm^{-1}) of the Lorentzian contributions from the different optical absorption bands for SWCNTs, C$_{60}$ Peapods, and DWCNTs/C$_{60}$ (error bar 10 cm^{-1} for S$_{11}$ and S$_{22}$; error bar 30 cm^{-1} for M$_{11}$, S$_{33}$, and S$_{44}$.

	S$_{11}$	S$_{22}$	M$_{11}$	S$_{33/44}$
SWCNTs				
	4800	8960	13300	17763
	5255	9610	14180	18873
	6920	10330	15098	19909
C$_{60}$ Peapods				
	4914	9020	13440	16875
	5350	9670	14260	17910
	9640	10340	15120	18947
DWCNTs/C$_{60}$				
	......	8930	13270	17700
	5185	9580	14100	18780
	6870	10300	......	19835

DWCNTs, they found that depending on the inner and outer carbon nanotubes diameters and also the periodicity of the circumferential direction (n,m), some of the absorption bands are splitted and new absorbtion bands are appeared. Contrary to expectations, no new contribution from the inner tubes appeared in the spectrum of the DWCNTs/C$_{60}$. This may be due to the coincidence between the optical transition from the inner and outer tubes and this makes the analysis of this region in the case of DWCNTs quite complex [141].

The above analysis described the C$_{60}$ peapods and DWCNTs/C$_{60}$ was also applied for the C$_{70}$-peapods and DWCNTs/C$_{70}$. Figure 4.23 shows the background-subtracted absorbance spectra of (a) SWCNTs, (b) C$_{70}$ peapods, and (c) DWCNTs/C$_{70}$ free-standing films. The absorption bands were fitted with Lorentzian oscillators and the contributions are listed in Table 4.3. According to Table 4.3, all the Lorentzian contributions in the C$_{70}$-peapods are not significantly changed, all the changes are within the error bar. As discussed in the subsection 4.2.2.1 that large fraction of the C$_{70}$ molecules are arranged in the transverse (standing) and the C$_{70}$-peapods is comparable to that in 1.31 nm diameter SWCNTs filled with C$_{60}$ molecules. According to Rochefort [67], the 1.3 nm SWCNT filled with C$_{60}$ molecules is energetically stable but not the ideal case for the hy-
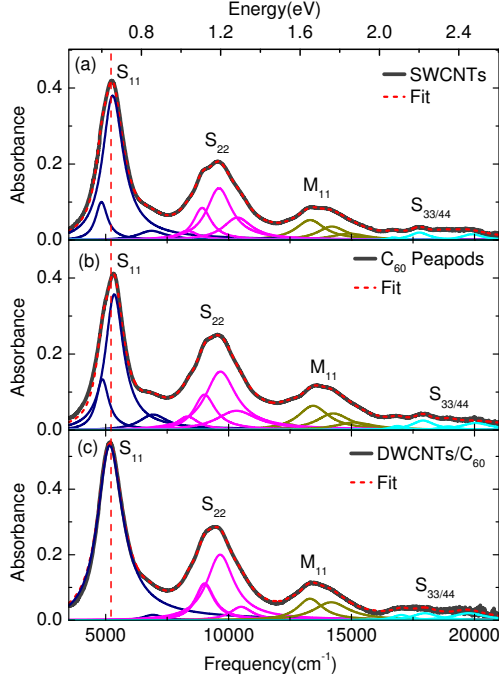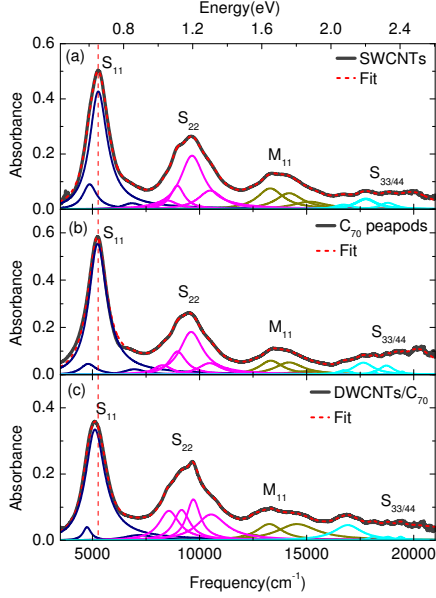
Figure 4.23: Background-subtracted absorbance spectra of (a) SWCNTs, (b) C_{70} peapods, and (c) DWCNTs/C_{70} together with the fit of the absorption bands using Lorentzian oscillators. The vertical, dashed line marks the position of the S_{11} band in SWC-NTs.

bridization between the NFE states of the nanotube wall and the C_{60} states. The effective tube diameter–and hence the energy position of the absorption bands–is not expected to be severely changed in this case. In the case DWCNTs/C_{70} all contributions are shifted to lower energies compared to the corresponding features in SWCNTs and also compared to the DWCNTs/C_{60} (see Table 4.2). This could be attributed to the fattening of the tubes with long heat treatment the effective tube diameters will increase [74], and hence the absorption bands are shifted to lower energies, according to the Kataura plot [37]. Also the increase of the tube diameters in the case of DWCNTs/C_{70} compared to DWCNTs/C_{60} is consistent with the HRTEM and Raman results and also with the previously published data [141].

According to the above discussion and based on equation 2.24, we can observe that the broad band between 1 and 1.5 eV in the case of DWCNTs/C_{70} [see Figure 4.23 (c)] consists of many pronounced contributions from the S_{22} optical transitions of the outer tubes and S_{11} optical transitions of the inner tubes. Also the obvious band centred at 16920 cm^{-1} ($\approx$ 2.1 eV) could be assigned to the S_{22} optical transitions of the inner tubes. The appearance of the new contributions from the inner tubes of DWCNTs/C_{70} compared to DWCNTs/C_{60} is not an indication of the high filling but it could be due to different inner tubes distribution

Table 4.3: Peak-position frequencies (in cm^{-1}) of the Lorentzian contributions from the different optical absorption bands for SWCNTs, C_{70} Peapods, and DWCNTs/C_{70} (error bar 10 cm^{-1} for S_{11} and S_{22}; error bar 30 cm^{-1} for M_{11}, S_{33}, and S_{44}.

	S_{11}	S_{22}	M_{11}	$S_{33/44}$
SWCNTs	4800	8960	13300	17763
	5255	9610	14180	18873
	6920	10330	15098	19909
C_{70} Peapods	4800	8970	13320	18150
	5240	9610	14140	18725
	6920	10330	......	19465
DWCNTs/C_{70}	4745	8570	13250	16920
	5115	9160	14550	......
	6920	9710	......	......
	......	10540	......	......

in the case of DWCNTs/C_{70}. This behaviour could be explained as follows: as discussed above, large fraction of the C_{70} peapods are filled with the ellipsoidal C_{70} molecules in transverse position (with the 0.792 nm axis) and the rest of the peapods are filled with C_{70} molecules in the tangential position (with the 0.691 nm axis). This means that during the transformation of the C_{70} molecules to inner walls by heat treatment, the formation of different inner tubes diameters and also different chiralities is expected .

Figure 4.24 (a) and (b)show the background-subtracted absorbance spectra of SWCNTs and I-SWCNTs free-standing films, respectively. The absorption bands were fitted with Lorentzian oscillators and the contributions are listed in Table 4.4. From Table 4.4 one can observe that all the contributions in the case of I-SWCNTs are not significantly changed, all the changes are within the error bar. Compared to the empty SWCNTs the intensity of the S_{11} optical transition is reduced. It has been demonstrated that the hole doping of SWCNTs can remove electrons from the valence band [149, 161, 162]. Consequently, some allowed optical transitions are reduced. therefore, the reduction of the S_{11} optical in the case of I-SWCNTs could be attributed to the removal of electrons from the valence band of the I-SWCNTs [see Figure 4.24(c)]. To confirm this idea, S_{11}/S_{22} spectral weight ratio for SWCNTs, C_{60}-peapods, C_{70}-peapods, I-SWCNTs, DWCNTs/C_{60}, and DWCNTs/C_{70} were calculated. The values are
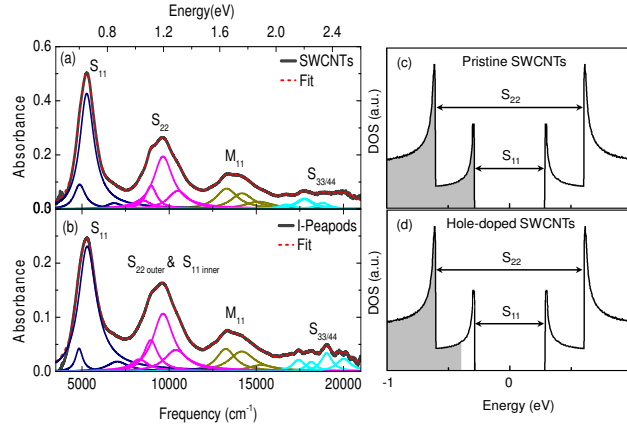
Figure 4.24: Background-subtracted absorbance spectra of (a) SWCNTs and (b) I-SWCNTs together with the fit of the absorption bands using Lorentzian oscillators. The right panel shows the Electronic density of states (DOS) of (c) pristine semiconducting (16,3) SWCNTs, where the valence band is filled with electrons and (d) Hole-doped semiconducting SWCNTs; the S_{11} spectral weight is decreased due to the partial depletion of the valence band electrons.

1.35, 1.33, 1.38, 1.10, 1.38, 1.00, respectively. All the S_{11}/S_{22} spectral weight ratio for all the samples is around 1.38 except two samples; I-SWCNTs and DWCNTs/C_{70}. The lower ratio in the case of I-SWCNTs can be ascribed to the removal of electrons from the first allowed optical transition due the hole doping and hence a reduction in the S_{11} optical transition is expected. But in the case of DWCNTs/C_{70} the spectral weight ratio is lower than that of SWCNTs and I-SWCNTs. This is due to the increase of the spectral weight of the broad band between 1 and 1.5 eV [see Figure 4.23(c)] because of the appearance of more contribution from the S_{22} optical transitions of the outer tubes and S_{11} optical transitions of the inner tubes.

Table 4.4: Peak-position frequencies (in cm^{-1}) of the Lorentzian contributions from the different optical absorption bands for SWCNTs and I-SWCNTs (error bar 10 cm^{-1} for S$_{11}$ and S$_{22}$; error bar 30 cm^{-1} for M$_{11}$, S$_{33}$, and S$_{44}$.

	S$_{11}$	S$_{22}$	M$_{11}$	S$_{33/44}$
SWCNTs				
	4800	8960	13300	17763
	5255	9610	14180	18873
	6920	10330	15098	19909
I-SWCNTs				
	4830	8940	13250	17435
	5300	9650	14170	18125
	6960	10390	15100	19033
	......	......	......	20000

4.3   Summary

Within the present work the CVD method was used to prepared size-controllable DWCNTs. From the SEM images, the prepared samples contain pure CNTs without any significant amount of amorphous carbon but the images reveal that the sample contains MWCNTs rather than DWCNTs. Therefore, the peapods method was used to prepare DWCNTs.

HRTEM images showed that DWCNTs/C$_{60}$ and DWCNTs/C$_{70}$ were prepared from the highly filled C$_{60}$ ($\geqslant$ 95%) and C$_{70}$ ($\geqslant$ 90%) peapods, respectively. From the HRTEM images, the average outer tubes diameters were found to be 1.5 and 1.6 nm in the case of DWCNTs/C$_{60}$ and DWCNTs/C$_{70}$, respectively.

Raman spectroscopy results showed that in the case of C$_{60}$-peapods, the charge transfer between the C$_{60}$-molecules and the tube wall causes a softening of the C-C bonds of the SWCNTs, shifting the RBMs to lower frequencies. On the other hand, the RBMs in the case of C$_{70}$-peapods are not affected by the filling with C$_{70}$ molecules. The appearance of the Raman active modes: A$_g$(1) and A$_g$(2) in the case of C$_{60}$ peapods, E$_1^{''}$, E$_2^{'}$, E$_1^{''}$, A$_1^{'}$ in the case of C$_{70}$ peapods, and For, I$_5^-$ and I$_7^-$ polyiodide chains in the case of I-SWCNTs indicates the high filling ratio of the filled SWCNTs.

Compared to the SWCNTs, the RBMs in the case of DWCNTs/C$_{60}$ and DWCNTs/C$_{70}$ were shifted to lower frequencies by 5-7 cm^{-1} and 1-10 cm^{-1},

respectively. The average outer and inner tubes diameters were found to be 1.43 and 0.8 nm in the case of DWCNTs/C_{60} and 1.45 and 0.85 nm in the case of DWCNTs/C_{70}, respectively. The downshift and the slight increase in the outer tubes diameters compared to the SWCNTs was attributed to the tubes fattening with the heat treatment.

The G modes in the case of C_{60} peapods were shifted to higher energies due to the radial overlapping between the fullerene molecules and the tubes, while in the case of C_{70} peapods the charge transfer or the interaction between the C_{70} molecules and the outer tube seems to be too small to be observed in the Raman data. For the I-SWCNTs, the G lines were upshifted by 9-18 cm^1 compared to the empty SWCNTs due to the electron transfer from the SWCNTs to the iodine molecules. In the case of DWCNTs/C_{60}, and (c) DWCNTs/C_{70}, the three components of the G mode appear at the same positions compared to the SWCNTs, which means that the charge transfer or the interaction between the inner and outer tubes seems to be too small to be observed in the Raman data.

For all the samples under investigation quantitative analysis was not possible for the broad absorption continuum in the FIR-MIR region because of the different thicknesses of the free-standing films. In the case of DWCNTs/C_{60}, the two IR active modes at 825 and 862 cm^{-1} were attributed to E_1 and A_1 symmetry, respectively. The appearance of these two modes means that purification of the nanotubes under high temperature and dynamic vacuum is required to enhance the visibility of the nanotubes IR active modes.

In comparison with SWCNTs all the optical transitions were shifted to higher energies in the case of C_{60} peapods due to the reduction of the effective tube diameter, whereas no significant shifts were observed for C_{70}-peapods. In the case of DWCNTs/C_{60} and DWCNTs/C_{70} all the optical transitions were shifted to lower energies due to the tubes fattening. Due to the hole doping of SWCNTs by iodine atoms in the case of I-SWCNTs, the S_{11}/S_{22} spectral weight ratio is smaller than the empty SWCNTs because of electron removal from the valence band of the nanotube.

Chapter 5

Results and Discussion

In this chapter, pressure-dependent infrared and optical spectroscopy studies on the SWCNTs, C_{60}-, C_{70}-peapods, DWCNTs/C_{60}, and DWCNTs/C_{70} film are presented and discussed. The pressure-dependent transmission measurements were performed up to $\approx$ 20 GPa using alcohol-mixture, argon, and nitrogen as pressure transmitting medium over a broad frequency range between 150- 20000 cm^{-1}. The effect of the different pressure transmitting media on the electronic properties of the nanotubes under pressure will discussed in detail.

5.1 SWCNTs under Pressure

Figure 5.1 shows the back-ground subtracted optical absorbance spectra at the lowest pressure values for SWCNTs, using (a) nitrogen, (b) argon, and (c) alcohol-mixture as pressure transmitting medium (PTM) in the NIR-VIS range. One can observe that compared to the free-standing SWCNTs film [see Figure 4.22], the absorption bands are broadened and the fine structure due to different tube diameters is smeared out. Therefore, a smaller number of Lorentz contributions are needed for obtaining a good fit of the spectra. This can be seen in Figure 5.1, showing the optical absorbance spectra of SWCNTs at the lowest pressure together with the total fitting curve and the Lorentz terms. In the further analysis and discussion, only the strong Lorentz contributions will be considered. In the case of SWCNTs, one can observe only one strong contribution for the S_{11} band
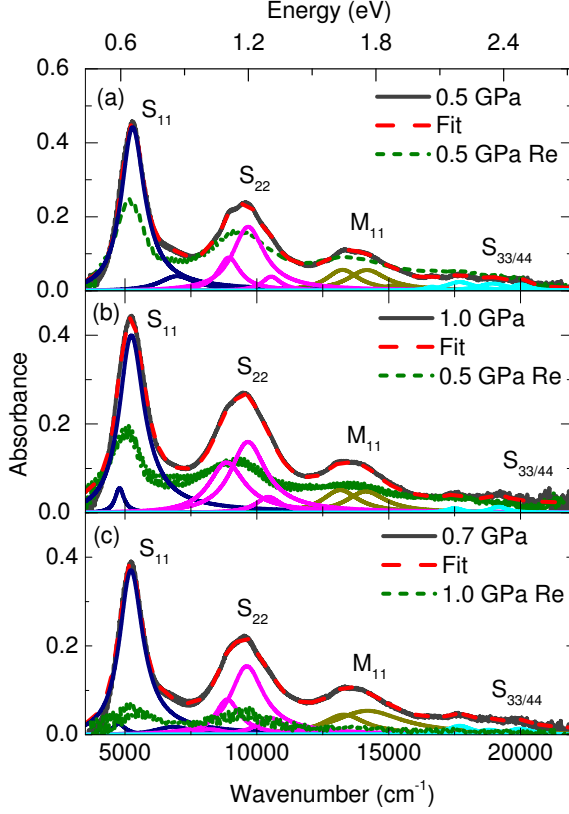
Figure 5.1: Optical absorbance spectrum at the lowest pressure during pressure increase together with the various Lorentzian contributions and the absorbance spectrum at the lowest pressure during pressure release, for the SWCNT film, using (a) nitrogen, (b) argon, and (c) alcohol-mixture as PTM in the NIR-VIS range. The labels S_{ii} and M_{ii} denote the *ith* optical transition in semiconducting and metallic tubes, respectively.

and two strong contributions for S_{22} and M_{11} bands, which are marked by $S_{22}(1)$, $S_{22}(2)$ and by $M_{11}(1)$, $M_{11}(2)$, respectively. The effect of different PTM on the optical absorbance spectra of the SWCNTs at the lowest pressure values is not clear since the values of the applied pressure is low but one can observe that the lowest pressure value in the case of nitrogen (0.5 GPa) is lower compared to argon and alcohol-mixture as PTM (1.0 and 0.7 GPa, respectively). This could be attributed to the high compressibility of liquid nitrogen compared to liquid argon and alcohol-mixture [163, 164].

Figure 5.2 show the background-subtracted absorbance spectra as a function of pressure for SWCNTs using (a) nitrogen, (b) argon, and (c) alcohol-mixture as PTM for selected pressures up to ≈ 20 GPa. One can observe that with increasing pressure all absorption bands are red-shifted, broadened, and lost spectral weight. When nitrogen is being used as PTM, the optical transitions S_{11}, S_{22}, and M_{11} are resolvable up to the highest applied pressure (16.8 GPa). In the case of
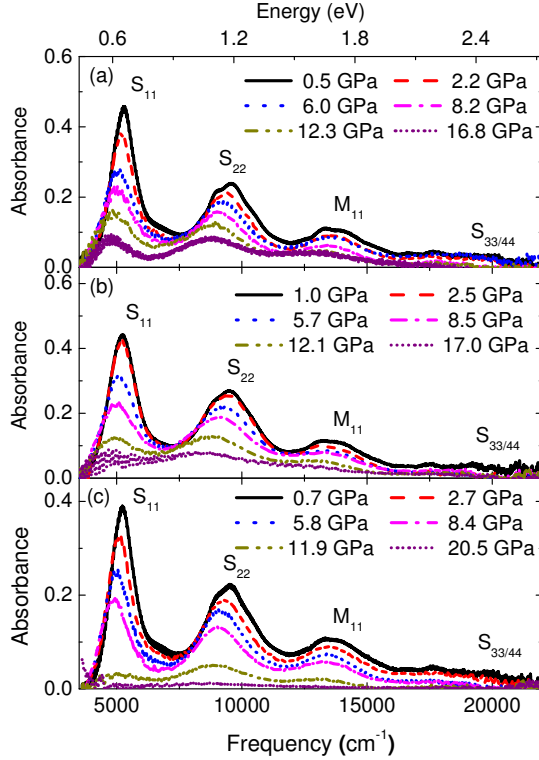
Figure 5.2: Background-subtracted absorbance spectra of SWCNTs as a function of pressure, using (a) nitrogen, (b) argon, and (c) alcohol-mixture as PTM.

argon as PTM, all optical transitions are resolvable only up to ≈ 12 GPa. For pressures above 12 GPa all optical transitions become very broad [see Figure 5.2(b)]. Furthermore, all optical transitions are resolvable only up to ≈ 10 GPa in the case of alcohol-mixture as PTM and above 10 GPa all absorption bands are completely smeared out [see Figure 5.2(c)].

The red-shift of the optical absorption peaks with applying pressure is in a good agreement with the previous optical pressure-dependent studies on SWC-NTs [165–169]. The red-shift of the absorption bands was attributed to the intertube interactions and/or σ^*-π^* hybridization and symmetry breaking [165, 166, 170, 171]. However, a high pressure optical spectroscopy study by Wu *et al.* [166] on debundled SWCNTs showed that the pressure coefficient of the optical absorption bands depends on the nanotubes chiralities, meaning that the red-shifts of the absorptions bands are intrinsic property of the nanotubes and the intertube interactions do not play a significant role on the pressure induced effects. Deacon *et al.* [172] suggested that the nanotubes surrounding surfactant

induces the red-shift. As the pressure increases the dielectric constant of the surrounding surfactant medium increases, leading to a decrease of the total coulomb interaction. Later from experimental optical spectroscopy results using solid CsI as PTM, the red-shift was also observed [111, 165, 168, 173]. The behaviour of the Raman active G-mode was nearly the same with using alcohol-mixture, argon, and even without PTM [174]. This suggesting that the effect of the surrounding surfactant medium can be excluded.

Charlier *et al*. [170] showed that the deformed or polygonized SWCNTs will lose its symmetry and the out-of-plane bonds along the edges of the deformed tubes will lose some of its sp^2 character and gain some sp^3 hybridization or what is called σ^*-π^* hybridization. The σ^*-π^* hybridization induces changes in the nanotubes optical properties: (i) the absorption peaks shift to lower energies, which signals the movement of the bands towards the fermi level. (ii) the absorption bands broaden due to the splitting of the bands. Several studies have revealed that the optical properties of the deformed tubes depend on the nanotube chirality. Where, the σ^*-π^* hybridization strongly affect the electronic properties of semiconducting and metallic zigzag SWCNTs. In case of the undeformed semiconducting (10,0) SWCNTs, the wavefunction is equally distributed inside and outside the nanotubes, leading to a state of pure π^* antibonding bands. In contrast, in the deformed (10,0) SWCNTs, the wavefunction is anisotropic and the σ^*-π^* hybridization is expected, leading to a decrease in the optical gap. For the metallic (12,0) and (18,0) SWCNTs, at lower applied pressure the hybridization induces both curvature and symmetry breaking, leading to a gap opening (semiconductor behaviour), with further pressure increasing the gap may be closed and the valence and conduction bands intercross each others [170, 171]. Recently, an in-situ atomic force microscopy coupled to confocal Raman spectroscopy study on the effect of pressure on both bundled and isolated SWCNTs showed that due to the symmetry breaking the intensity of G-mode decreased significantly with applying pressure [175]. Accordingly, the red-shift and the broadening of the optical absorption bands under pressure can be attributed to the pressure-induced deformation of the nanotubes, causing σ^*-π^* hybridization and changing the symmetry of the nanotubes.

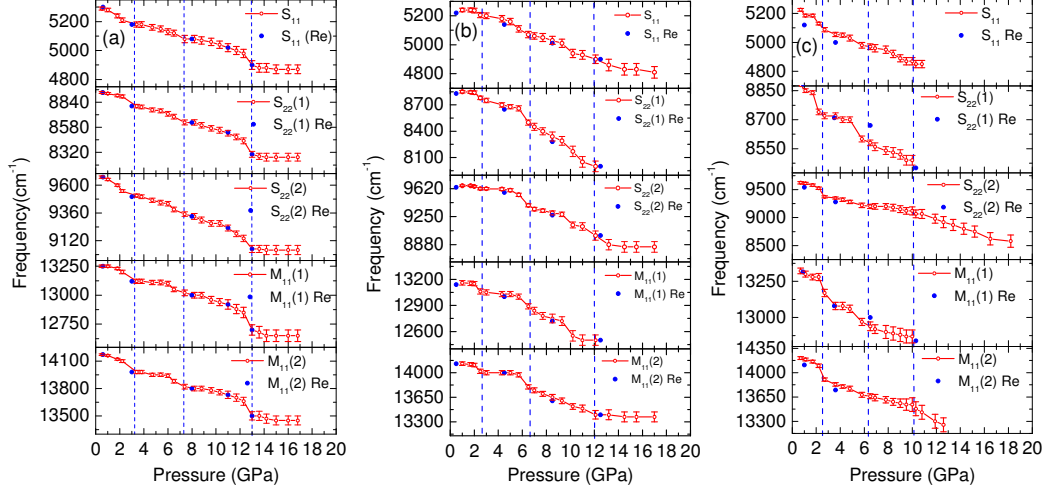The pressure-induced effects on the absorption bands of the SWCNTs film

Figure 5.3: Pressure dependence of the optical transition energies obtained from the absorbance spectra for SWCNTs, using (a) nitrogen, (b) argon, and (c) alcohol-mixture as PTM.

are shown in Figure 5.3, where the so-obtained energies of the Lorentz functions describing the absorption bands are plotted as a function of pressure, for (a) nitrogen, (b) argon, and (c) alcohol-mixture as PTM.

One can observe that with increasing pressure, the absorption bands are shifted to lower energies up certain critical values: $P_{c1} \approx 2\text{-}3$, $P_{c2} \approx 6.5\text{-}7.5$, and $P_{c3} \approx 10\text{-}13$ GPa, depending on the pressure transmitting medium. In the case of nitrogen, the values of P_{c1}, P_{c2}, and P_{c3} are higher than the corresponding values in the case of argon and alcohol-mixture as PTM. For alcohol-mixture, above 10 GPa drastic changes are observed, where most of the Lorentz contributions are disappeared. This could be attributed to the solidification of the alcohol-mixture above 10 GPa. Therefore, the values of the critical pressure depend on the degree of hydrostaticity of the the PTM used. For a quantitative analysis of the pressure-induced red-shifts of the absorption bands, Figure 5.4 (a) depict the relative energy shifts of the Lorentz contributions as a function of pressure for SWCNTs using nitrogen as PTM. The shift was calculated as the difference between the absorption frequency of the contribution ν_{pi} at a pressure pi, and the absorption frequency ν_{p1} at the lowest pressure value $p1$. The vertical dashed, blue lines mark the critical pressures. One can observe three anomalies
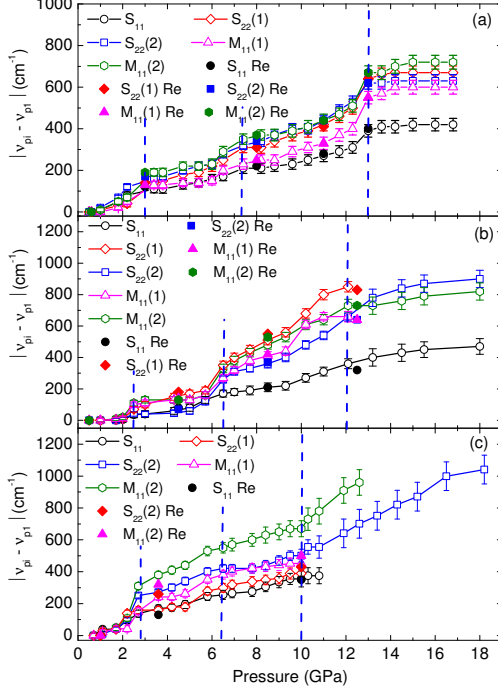
Figure 5.4: Relative energy shift of the optical transitions as a function of pressure in SWCNTs, using (a) nitrogen, (b) argon, and (c) alcohol-mixture as PTM. The shift was calculated as the difference between the absorption frequency of the contribution ν_{pi} at a pressure pi, and the absorption frequency ν_{p1} at the lowest pressure value $p1$. All the contributions during pressure release are marked as S_{ii} (Re) and M_{ii} (Re) for both semiconducting and metallic tubes, respectively. The vertical dashed, blue lines mark the critical pressures as discussed in the text.

in the relative pressure-induced shifts at $P_{c1} \approx 3$ GPa, $P_{c2} \approx 7$ GPa, and $P_{c3} \approx 13$ GPa, followed by a plateau.

Based on theoretical calculations [78, 176, 177] it has been shown that for SWCNTs with diameters larger than 1.7 nm the highly symmetric circular shape of the nanotubes spontaneously deforms to hexagonal shape. In this case the circular to hexagonal shape transformation is energetically favourable and occurs spontaneously even without applying external pressure. This was attributed to the attractive intertube van der Waals interactions. For SWCNTs with diameters less than 1.7 nm, the spontaneous circular to hexagonal deformation is not expected because the hexagonal shape has six corners where the bonds are buckled, therefore the intertube van der Waals interactions become serious disadvantage in terms of energy and a serious repulsion forces will arise. Accordingly, with applying external pressure on the circular SWCNTs with diameters less than 1.7 nm, the nanotubes should transform to more flexible shape than the hexagonal, which is the oval shape, to reduce the repulsion forces. In this case the transformation from the circular to the oval shape will occur easily by the the C-C bonds buck-
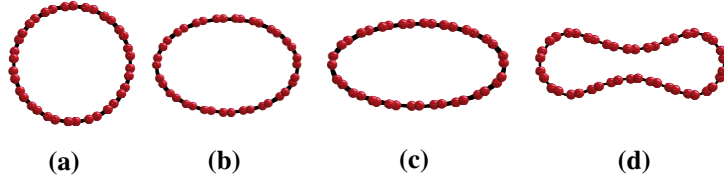
Figure 5.5: Proposed sequence of structural deformation of SWCNTs.

ling without any significant reduction of the C-C bond length [78]. Therefore, according to the above discussion and to earlier experimental results and theoretical predictions [78, 85, 167, 178–184], the anomaly at P_{c1} is interpreted as a structural phase transition from circular to oval shape. The anomaly at P_{c2} signals a more drastic change in the tubes' cross section from oval to race-track or peanut-type shape [79, 174, 185].

According to Yao *et al.* [174, 186], upon further pressure increase after the P_{c2}, a more flattened shape is expected. This flat shape can be considered as two graphene sheets connected with two caps at the ends. Now the conjugated π-bonds between the carbon atoms is more effective, where the surfaces of the two graphene sheets are slightly deformed due to the strong intertube repulsion. There is a limit to the compressibility of the nanotubes, when the distance between the two graphene sheet is 3.8 Å, which is comparable to the distance between the two graphite layers 3.35Å. At this point the C-C bonds become hard to compress and then a plateau in the pressure deformations is expected. Further compression is also possible but it will reach the stiff limit of the van der Waals interactions between the two graphene layers. In this case, the two caps at the ends of the two graphene layers will destroyed due to the excessive bonds buckling [78]. Accordingly, the plateau with an onset at $P_{c3} \approx 13$ GPa indicates a saturation of the pressure-induced deformation and hybridization effects above this pressure and the behaviour of the SWCNTs above 13 GPa can be interpreted in terms of the collapse of the tubes [80, 185]. The proposed sequence of structural deformations in SWCNTs is illustrated in Figure 5.5 (a) to (d).

To clarify the influence of the PTM on the stability of SWCNTs, Figure 5.4 (b) and (c) depicts the relative pressure-induced energy shifts of the Lorentz contributions, using argon and alcohol-mixture as PTM, respectively. In the case of

argon, the anomalies in the pressure-induced shifts are lowered to $P_{c1} \approx 2.5$ GPa, $P_{c2} \approx 6.5$ GPa, and $P_{c3} \approx 12$ GPa. Above P_{c3} all the optical transitions S_{11}, S_{22}, and M_{11} become very broad and each can be fitted with one Lorentzian contribution. Also the relative energy shifts are higher than the corresponding shifts, when nitrogen is being used as PTM. The broadening of the absorption bands and the lower critical pressures are due to the lower hydrostaticity level of argon compared to nitrogen as PTM [112]. Also, in the case of alcohol-mixture, the anomalies in the pressure-induced shifts are lowered to $P_{c1} \approx 2.5$ GPa and $P_{c2} \approx$ 6.5 GPa. Above ≈ 10 GPa, all the absorption bands are smeared out except the S_{22} (2) and M_{11} (2) optical transitions. Both transitions are highly red-shifted with a very large error bar because of the broadening. Alcohol-mixture is a hydrostatic PTM below 10 GPa but becomes quasi-hydrostatic above 10 GPa due to solidification [112]. Therefore, above 10 GPa the SWCNTs are completely collapsed in the case of alcohol-mixture as PTM. Interestingly, the SWCNTs filling with nitrogen, argon, or alcohol-mixture does not prevent the pressure-induced anomalies in the electronic transitions due to tubular deformation. It has been demonstrated previously that fluids, nitrogen or argon as PTM can intercalate inside the SWCNTs [87, 187–189], introducing a steric barrier which is responsible for the SWCNTs stabilization against the applied pressure. In contradiction to earlier reports [187, 190] this kind of stabilization was not observed in our data.

Figures 5.3 and 5.4 show the reversibility of the pressure-induced structural changes for SWCNTs using (a) nitrogen, (b) argon, and (c) alcohol-mixture as PTM. The pressure-induced frequency shifts of the optical transitions are reversible regarding their frequency position upon pressure release from the highest applied pressure (18-20 GPa). However, one notices a loss in the intensity of the original absorbance value, namely, up to ≈ 50-60% in the case of nitrogen and argon and $\approx 85\%$ in the case of alcohol mixture [see Figure 5.1]. The irreversible changes indicate that a fraction nanotubes has been permanently damaged under pressure. In the case of alcohol mixture the greater damage of tubes is due to the non-hydrostaticity of the alcohol mixture above 10 GPa [112]. It is known that carbon nanotubes are very stiff material in its axial direction but soft in its radial direction. Therefore, when the nanotubes are subjected to a moderately high pressure, the radial deformation dominates. Under high pressure above the

plateau of the G-mode (at about 11 GPa), the pressure dependence of the G-mode was close to that of the graphite under high pressure. This means that further increase of pressure after the collapse pressure, the nanotubes will transform to a narrow strip with double layer graphene structure. Therefore, van der Waals interaction is expected between the collapsed walls of the nanotube and in this case the collapsed nanotube resembles the graphite in terms of density and hybridization [174].

Figure 5.6 shows the absorbance spectra of the SWCNT film for selected pressures up to 13 GPa in the MIR and FIR frequency ranges (200-7000 cm^{-1}), using nitrogen as PTM. Since all the carbon nanotubes free-standing films prepared in the present work do not have the same thickness, a quantitative analysis can not be carried out accurately in this region. Therefore, only the effect of nitrogen as PTM on the absorption behaviour of the SWCNTs will be shown. From Figure 5.6, one can observe clearly the S$_{11}$ absorption peak for all the pressure values up to 13 GPa. The behaviour of this band under pressure was discussed in details under last paragraphs. The inset of Figure 5.6 shows only the FIR region (200-700 cm^{-1}). One can observe wiggles in the absorbance spectra for all the pressure values. These wiggles are Fabry Perot interference fringes due to the multiple reflection between the sample and the diamond anvil surface. The appearance of such wiggles can be explained as follows: the nitrogen filling was done by immersing the CryoDAC Mega DAC at room temperature directly into the cryogenic liquid nitrogen, so when the nitrogen enters the sample chamber it will start to boil due to the temperature difference between the gasket and the nitrogen. Due to the large sample chamber diameter $\approx 250\mu$m and the small thickness of the SWCNTs film (view hundred nanometer), the liquid nitrogen will lift the SWCNTs film up leaving a gap between the film and the diamond anvil surface. The presence of the such a gap and with the low energy of the IR beam will enhance the formation of these wiggles. Therefore, all the absorbance data in the FIR have been smoothed using a 100-points adjacent averaging function of Origin Pro 8.6 software. After that the FIR data were merged with the MIR dat as shown in Figure 5.6.

From Figure 5.6, one can observe that in the FIR region the absorbance level decreases monotonically with increasing pressure and at high pressure val-
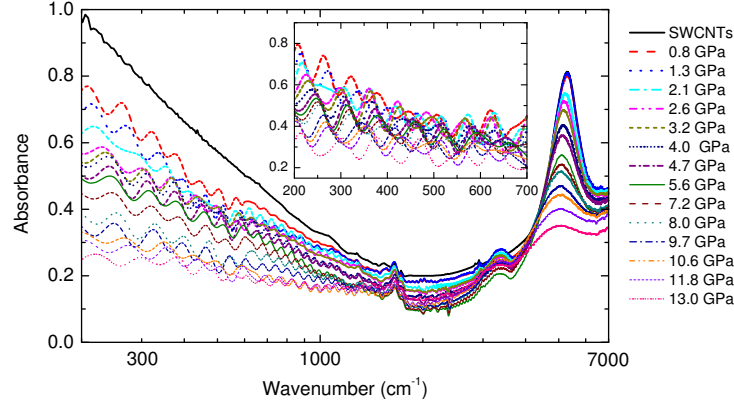
Figure 5.6: Absorbance spectra of the SWCNTs film for selected pressures up to 13 GPa over a broad frequency range (200-7000 cm^{-1}) in MIR-MIR region. The inset shows only the data in the FIR region without smoothing.

ues it looks flat. Prior studies have noted the same behaviour but for covalently-functionalized SWCNTs [162, 191], where the covalent bonds destroy the SWCNTs electronic band structure. The destruction of the electronic band structure is due to the transformations of the π-bonds to covalent bonds or saturated C-C bonds, so the oscillations strength will rapidly lost from the FIR absorption level. A theoretical calculation by Bu *et al.* [192], predicted that with increasing the deformations in the SWCNTs, the localization length of the carriers will decrease, leading to a decrease in the conductivity. According to the above discussion and previous experimental studies [167, 173], the monotonic decrease of the absorbance level in the FIR can be explained as follows: equivalent to the nanotubes covalent functionalization is the symmetry breaking and the σ^*-π^* hybridization with pressure increasing which leads to a destruction of the SWCNTs' electronic band structure. Also, increasing pressure will decrease the localization length of the carriers, leading to a decrease in the conductivity level of the SWCNTs.

To support this idea, Figure 5.7 (a) shows the normalized spectral weight of S_{11}, S_{22}, and FIR absorption bands for SWCNTs as a function of pressure using nitrogen as a PTM. One notices that the spectral weights of the S_{11} and S_{22} absorption bands show three anomalies at $P_{c1} \approx 3.0$ GPa, $P_{c2} \approx 8$ GPa, and $P_{c3} \approx 13$ GPa. Theses values are consistent with those calculated from the relative pressure-induced energy shifts [see Figure 5.4 (a)]. Also, the spectral weight of
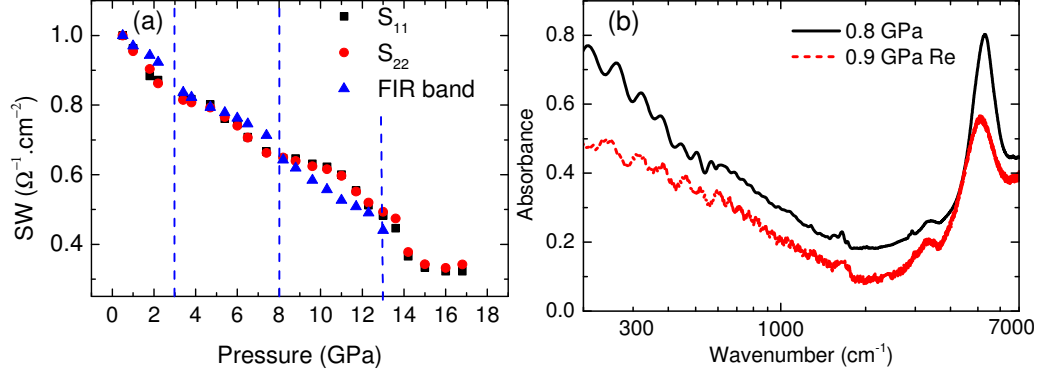
104

Figure 5.7: (a) Spectral weight of S_{11}, S_{22}, and FIR absorption bands for SWCNTs as a function of pressure using nitrogen as a pressure transmitting medium. (b) Absorbance spectra of the SWCNTs film at the lowest pressure during pressure increase together with the lowest pressure during pressure release in FIR-MIR region.

the FIR band shows two anomalies at $P_{c1} \approx 3.0$ GPa and $P_{c2} \approx 8$ GPa. We can not observe the anomaly at $P_{c3} \approx 14$ GPa because the maximum pressure we could achieve using the CryoDAC-Mega in FIR region is 13 GPa. The consistency between the S_{11} and S_{22} and FIR absorption bands anomalies indicates that the decrease of the absorbance level in the FIR region is related to destruction of the SWCNTs' electronic band structure.

Figure 5.7 (b) show the reversibility of the pressure-induced structural changes for SWCNTs in the FIR region using nitrogen as PTM. One notices a loss in the intensity of the original absorbance value, namely, up to $\approx 40\%$. This value is higher than corresponding loss calculated from the optical measurements in the NIR-VIS region (≈ 50-60%) [see Figure 5.1 (a)]. This could attributed to the lower applied pressure value (≈ 13 GPa) in the FIR region compared to ≈ 18 GPa in the case of optical measurements. Therefore, the permanent damage of the nanotubes under pressure application is less compared to the optical measurements.

5.2 DWCNTs under Pressure

The mechanical stability of the SWCNTs by filling the tubes with molecules or with inner tubes is an important issue. High-pressure Raman measurements

showed that filling of the SWCNTs with inner tube stabilizes the outer tubes; this kind of filling was considered as a case of homogenous filling. In this section, the effect of filling the SWCNTs inner wall on the their stability will be discussed. Two different types of DWCNTs will be studied: DWCNTs/C$_{60}$ and DWCNTs/C$_{70}$.

5.2.1   DWCNTs/C$_{60}$

Figure 5.8 shows the background-subtracted absorbance spectra as a function of pressure for DWCNTs/C$_{60}$ film at the lowest pressure together with the total fitting curve and the Lorentz contributions, using (a) nitrogen, (b) argon, and (c) alcohol-mixture as PTM. The absorption bands at the lowest pressure are broadened and the fine-structure due to different tube diameters is smeared out, as compared to the free-standing DWCNTs/C$_{60}$ film and to the SWCNTs film at lowest pressure [see Figures 4.22 (c) and 5.1, respectively] and only one Lorentz contribution for the S$_{11}$, S$_{22}$, and M$_{11}$ absorption bands is needed to obtain a good fit for the spectra.

Figure 5.9 shows the background-subtracted absorbance spectra as a function of pressure for DWCNTs/C$_{60}$ using (a) nitrogen, (b) argon, and (c) alcohol-mixture as PTM for selected pressures up to $\approx$ 20 GPa. One can observe that with increasing pressure all absorption bands are red-shifted, broadened, and lost spectral weight. When nitrogen is being used as PTM, all optical transitions S$_{11}$, S$_{22}$, and M$_{11}$ are resolvable up to the highest applied pressure. In the case of argon as PTM, all optical transitions are resolvable up to $\approx$ 12 GPa only but for pressures above 12 GPa the optical transitions become very broad. Furthermore, all optical transitions are resolvable only up to $\approx$ 10 GPa in the case of alcohol-mixture as PTM and above 10 GPa all the absorption bands are completely smeared out.

The pressure-induced effects on the absorptions bands of the DWCNTs/C$_{60}$ film are shown in Figure 5.10, where the so-obtained energies of the Lorentz functions describing the absorption bands are plotted as a function of pressure, for (a) nitrogen, (b) argon, and (c) alcohol-mixture as PTM. With increasing the pressure, the absorption bands are slightly shifted to lower energies up certain
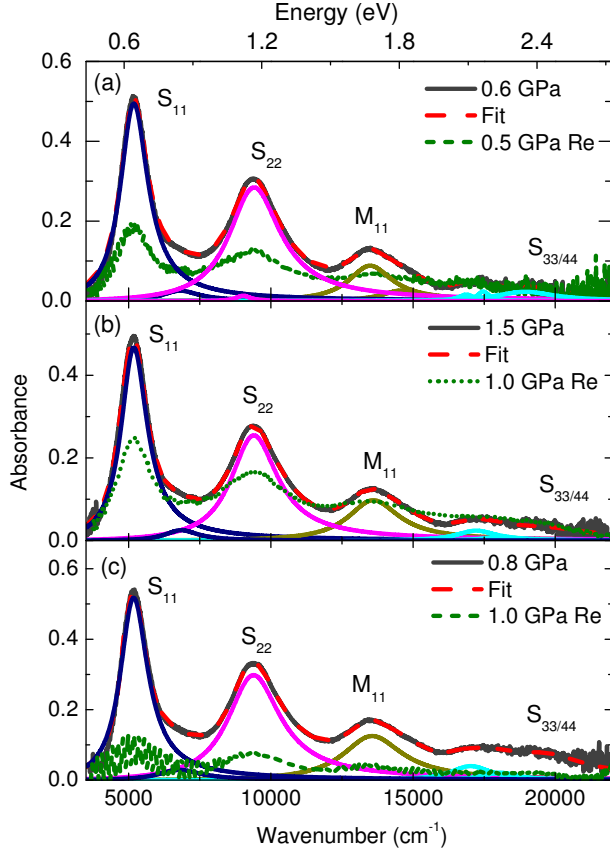
Figure 5.8: Optical absorbance spectrum at the lowest pressure during pressure increase together with the various Lorentzian contributions and the absorbance spectrum at the lowest pressure during pressure release, for the DWCNT/C$_{60}$ film, using (a) nitrogen, (b) argon and (c) alcohol-mixture as PTM in the NIR-VIS range. The labels S$_{ii}$ and M$_{ii}$ denote the *ith* optical transition in semiconducting and metallic tubes, respectively.

critical value p$_d$ ≈ 10-12 GPa, depending on the pressure transmitting medium. The red-shifts are very small compared to the empty SWCNTs [see Figure 5.3]. For alcohol-mixture, the value of p$_d$ is ≈ 10 GPa. Above 10 GPa a drastic changes are observed, where the S$_{11}$ and M$_{11}$ absorption peaks completely disappeared. This could be attributed to the solidification of the alcohol-mixture above 10 GPa. For a quantitative analysis of the pressure-induced red-shifts of the absorption bands, Figure 5.11 (a) shows the relative energy shifts of the Lorentz contributions as a function of pressure for DWCNTs/C$_{60}$ using nitrogen as PTM. Compared to SWCNTs [Figure 5.4], one notices that the red-shift of the absorption bands is very small, with a linear pressure coefficient in the range ≈ 9-15 cm^{-1}/GPa [the linear fit is shown in Appendix A Figure 1]. Above ≈ 12 GPa the relative energy shifts of the absorption bands steeply increase and seem to saturated. This behavior signals strong pressure-induced alterations in the electronic properties of the outer tube at a critical pressure P$_d$≈ 12 GPa related to tubular deformation.
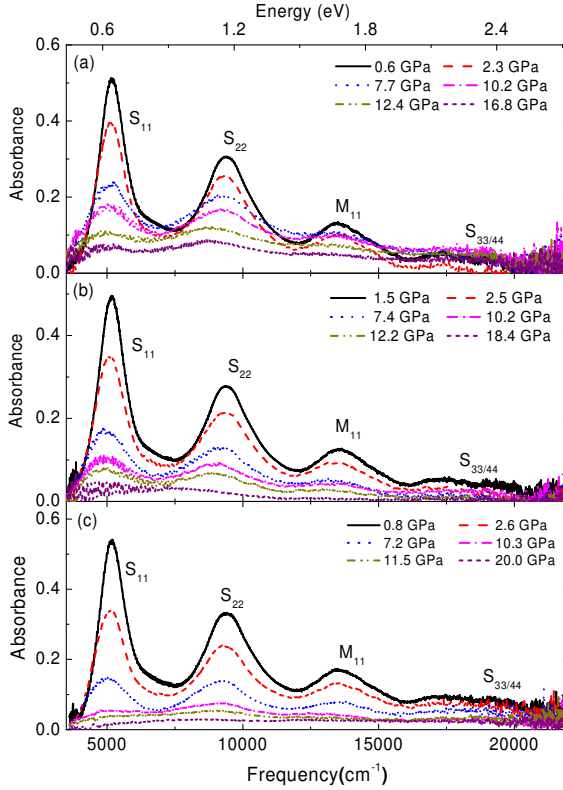
Figure 5.9: Background-subtracted absorbance spectra of DWCNTs/C$_{60}$ as a function of pressure, using (a) nitrogen, (b) argon, and (c) alcohol-mixture as PTM.

It has been demonstrated previously by high-pressure Raman spectroscopy studies on DWCNTs [193–195], that the inner wall increases the mechanical stability of the outer tube upon pressure application. Where, the pressure slopes of the RBM and the G-mode for the outer tubes were decreased upon filling with inner wall. Therefore, the small red-shift of the absorption bands could be explained in terms of the reduction of the σ^*-π^* hybridization and symmetry breaking effects in the outer tubes of the DWCNTs. This finding signals the mechanical stabilization of the outer tube by the inner tube [185].

The effect of filling of the SWCNTs with inner tube on the structural stability has been discussed in many experimental and theoretical studies [80, 83–86]. Aguiar *et al.* [80] have examined the collapse of the highly purified DWCNTs (d$_{inner} \approx 0.85$ nm, d$_{outer} \approx 1.55$ nm) produced by the CVD method. They found that the collapse of the DWCNTs is two-steps process: the onset of the collapse of the outer tube is ≈ 21 GPa, which is higher than the corresponding empty SWCNTs (≈ 9 GPa), showing that the inner wall supports the outer one. The
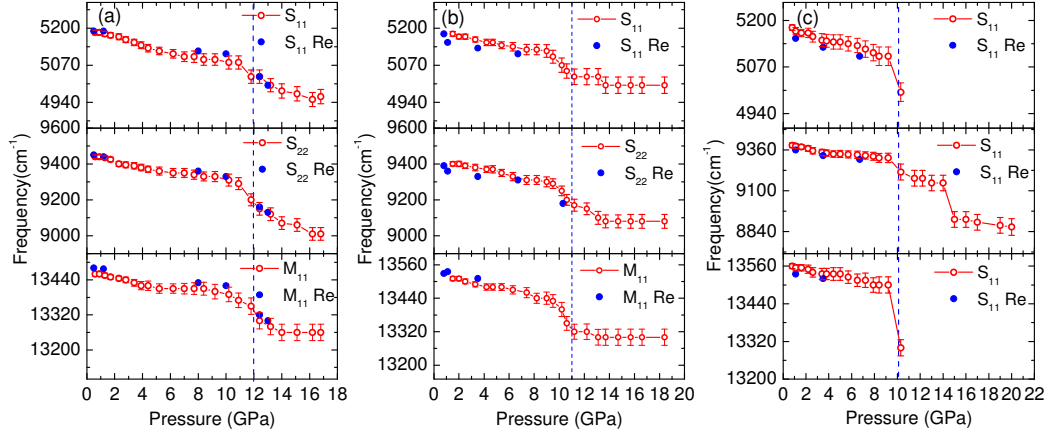
Figure 5.10: Pressure dependence of the optical transition energies obtained from the absorbance spectra for DWCNTs/C$_{60}$ using (a) nitrogen, (b) argon, and (c) alcohol-mixture as PTM.

collapse of the outer tube followed by the collapse of the inner tube at ≈ 25 GPa. The expected collapse pressure of the 0.85 nm SWCNTs was estimated to be at around 54 GPa but the collapse of the outer tube at ≈ 21 GPa add an additional pressure on the inner tube, leading to lower collapse pressure.

In a more recent high pressure resonance Raman scattering study of Aguiar *et al.* [72], they compared the mechanical stability of three different kinds of DWCNTs: bromine-intercalated DWCNTs grown by CVD method, C$_{60}$-peapods derived DWCNTs, and pristine CVD grown DWCNTs. For the bromine -intercalated DWCNTs, the collapse pressure was lowered to 13 GPa compared to the pristine CVD grown DWCNTs (≈ 21 GPa as discussed in the previous work of Aguiar *et al.* [80]). The lower collapse pressure was attributed to the rearrangement of the Br atoms between the interstitial channels of the DWC-NTs bundles which could induce uniaxial stress in the radial direction of the DWCNTs, thus leading to lower collapse pressure. In the case of C$_{60}$-peapods-derived DWCNTs, the collapse pressure was found to be 12 GPa, lower than the bromine-intercalated DWCNTs grown by CVD method and pristine CVD grown DWCNTs. Here, the lower collapse pressure was explained as follows: the inner tubes of the C$_{60}$-peapods-derived DWCNTs were grown by the heat treat-
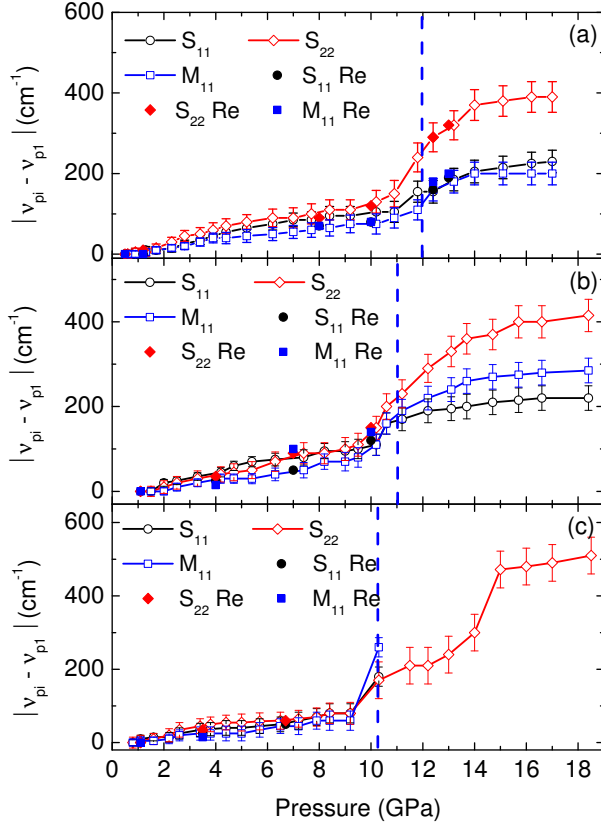
Figure 5.11: Relative energy shift of the optical transitions as a function of pressure in DWCNTs/C$_{60}$ using (a) nitrogen, (b) argon, and (c) alcohol-mixture as PTM. The shift was calculated as the difference between the absorption frequency of the contribution ν_{pi} at a pressure pi, and the absorption frequency ν_{p1} at the lowest pressure value $p1$. All the contributions during pressure release are marked as S$_{ii}$ (Re) and M$_{ii}$ (Re) for both semiconducting and metallic tubes, respectively. The vertical dashed, blue lines mark the critical pressures as discussed in the text.

ment of the fullerene molecules inside the SWCNTs. This process could lead to the formation of short inner tubes inside the SWCNTs. Also, a multiple inter-atube junctions between the inner tubes are expected. In this case, the formed DWCNTs are considered to be inhomogeneously filled and contain many defects, which lead to lower collapse pressure. On the other hand, in case of pristine CVD grown DWCNTs, the inner and the outer tubes were grown simultaneously over the same catalyst and at the same temperature. Therefore, the mechanical coupling between the inner and the outer tubes is satisfied. Thus in this case the inner tubes are considered to be more homogeneous and contain less defect compared to the C$_{60}$-peapods-derived DWCNTs.

Yang *et al.* [84], proposed the structural change of DWCNTs bundles under hydrostatic pressure. For small diameter (5,5)@(10,10) DWCNTs bundles (d$_{inner}$ $\approx$ 0.68 nm, d$_{outer}$ $\approx$ 1.37 nm), a small discontinues volume change at $\sim$ 18 GPa

was observed followed by a cross-section deformation to two deformed hexagons. In this case, the (5,5) inner SWCNT supports the outer (10,10) SWCNT up to $\approx$ 18 GPa. The intermediate (11,2)@(12,12) DWCNTs bundles (d$_{inner}$ $\approx$ 0.96 nm, d$_{outer}$ $\approx$ 1.65 nm) undergo one structural phase transition and collapse at P$_d$ = 11.5 GPa. On the other hand, the large tube diameter (10,10)@(15,15) (d$_{inner}$ $\approx$ 1.37 nm, d$_{outer}$ $\approx$ 2.0 nm) DWCNTs bundles the tubes go through one structural phase transition at $\approx$ 4.68 GPa, where the nanotubes collapsed completely. Because of the similar diameters, the prepared DWCNTs/C$_{60}$ in the present work are expected to show similar effects under pressure like the (5,5)@(10,10)DWC-NTs, but with a somewhat smaller value of the critical pressure.

Gadagkar *et al.* [85] have shown that the collapse pressure of the DWCNTs is unique and its value equals the sum of the individual collapse pressure values of the inner and the outer tubes. They found that the collapse pressure is proportional to $1/R_{eff}^3$, where R_{eff} is the average value of the inner and the outer tube diameters or what is called effective radius. The effective radius R_{eff} is defined as

$$1/R_{eff}^3 = (1/n)\sum_{i=1}^{n}(1/R_i^3) \tag{5.1}$$

with n=2 for DWCNTs. From the calculated diameters for the DWCNTs/C$_{60}$ bundles from the HRTEM data [see section 4.2.1] and from Raman data [see section 4.2.2.2], an average inner and outer nanotubes diameters of d$_{inner}$ $\approx$ 0.80 nm and d$_{outer}$ $\approx$ 1.45 nm, respectively were estimated. Based on Equation 5.1, the effective radius for DWCNTs/C$_{60}$ bundles was estimated to be R_{eff} $\approx$ 0.48 nm and a critical pressure value of P$_d$ $\approx$ 13 GPa was calculated according to Ref. [85]. Thus, the finding of a critical pressure P$_d$ $\approx$ 12 GPa in the present work is in very good agreement with theoretical predictions for the onset of the deformations of the tube cross-sections in DWCNTs bundles and also with the experimental results of the C$_{60}$-peapods-derived DWCNTs [72]. Accordingly, the deformation of the DWCNTs/C$_{60}$ bundles can be explained in terms of a small discontinuous volume change accompanied by a cross sections' change to two deformed hexagons. The proposed sequence of structural deformations in DWCNTs is illustrated in Figure 5.12 (a) to (b).

Figure 5.11 (b) and (c) depict the relative pressure-induced energy shifts of
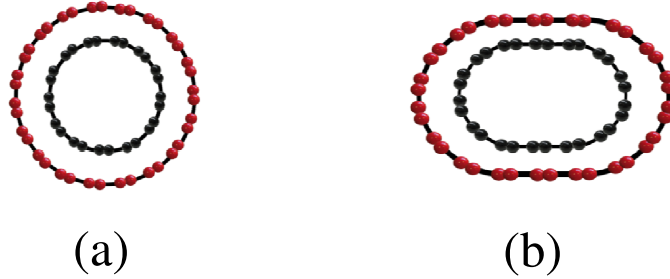
Figure 5.12: Proposed sequence of structural deformation of DWCNTs/C$_{60}$.

the Lorentz contributions, using argon and alcohol-mixture as PTM, respectively. In the case of argon, the critical pressure P$_d$ is lowered to $\approx$ 11 GPa. Above P$_d$ the relative energy shifts are slightly higher than the corresponding shifts, when nitrogen is being used as PTM. This could be attributed to the lower hydrostaticity level of argon compared to nitrogen as PTM [112]. Furthermore, in the case of alcohol-mixture, all absorption bands are completely smeared out above 10 GPa. Above 10 GPa the DWCNTs bundles might be collapsed due to the solidification of alcohol-mixture [112]. It is important to note that according to these results, the fluid PTM does not prevent the pressure-induced anomalies in the electronic transitions due to tubular deformation, in contradiction to earlier reports [187, 190].

The reversibility of the pressure-induced structural changes in DWCNT/C$_{60}$ bundles from the high applied pressure (18-20 GPa) using nitrogen, argon, alcohol-mixture as PTM is shown in Figures 5.10 and 5.11. One notices that the pressure-induced frequency shifts of the optical transitions are reversible regarding their frequency position upon pressure release. However, a loss in intensity of the original absorbance value, namely, up to $\approx$ 60% in the case of nitrogen and argon and $\approx$ 85% in the case of alcohol mixture [see Figure 5.8] is noticed. In the case of alcohol mixture the greater damage of tubes is due to the non-hydrostaticity of the alcohol mixture above 10 GPa [112].

5.2.2 DWCNTs/C$_{70}$

In this subsection the results of the high pressure optical spectroscopy on DWCNT/C$_{70}$ are presented. The effect of a different inner tubes diameters distribution on the stability of the nanotubes will be discussed and the results will be compared to those of the DWCNT/C$_{60}$. Here, only the results of nitrogen and argon as PTM will be shown because alcohol-mixture is not hydrostatic PTM above 10 GPa.

Figure 5.13 shows the background-subtracted absorbance spectra as a function of pressure for DWCNTs/C$_{70}$ film at the lowest pressure together with the total fitting curve and the Lorentz contributions, using (a) nitrogen and (b) argon as PTM. One can observe in the region between 1 and 1.5 eV the four pronounced contributions from the S$_{22}$ optical transitions of the outer tubes and S$_{11}$ optical transitions of the inner tubes which have been observed in the case of the DWCNTs/C$_{70}$ free-standing film. Also the band centred at 16920 cm^{-1} (≈ 2.1 eV) which was assigned to the S$_{22}$ optical transitions of the inner tubes still obvious. The appearance of new contributions from the inner tubes in the case of DWCNTs/C$_{70}$ compared to the DWCNTs/C$_{60}$ was attributed to the different inner tubes diameters and chiralities distribution in the case of DWCNTs/C$_{70}$ [as discussed in the subsection 4.2.3.2].

Figure 5.14 shows the background-subtracted absorbance spectra as a function of pressure for the DWCNTs/C$_{70}$ using (a) nitrogen and (b) argon as PTM for selected pressures up to ≈ 18 GPa. With increasing pressure all absorption bands are red-shifted, broadened, and lost spectral weight. The fine structure of the absorptions band between 1 and 1.5 eV from the S$_{22}$ optical transitions of the outer tubes and S$_{11}$ optical transitions of the inner tubes and the band centred at ≈ 2.1 eV from the S$_{22}$ optical transitions of the inner tubes are resolvable up to ≈ 12 GPa and ≈ 10 GPa in the case of nitrogen and argon data, respectively. Above these values all the absorption bands are broadened and most of them smeared out.

For a quantitative analysis of the pressure-induced red-shifts of the absorption bands, Figure 5.15 (a) depict the relative energy shifts of the Lorentz contributions as a function of pressure for DWCNTs/C$_{70}$ using nitrogen as PTM. One
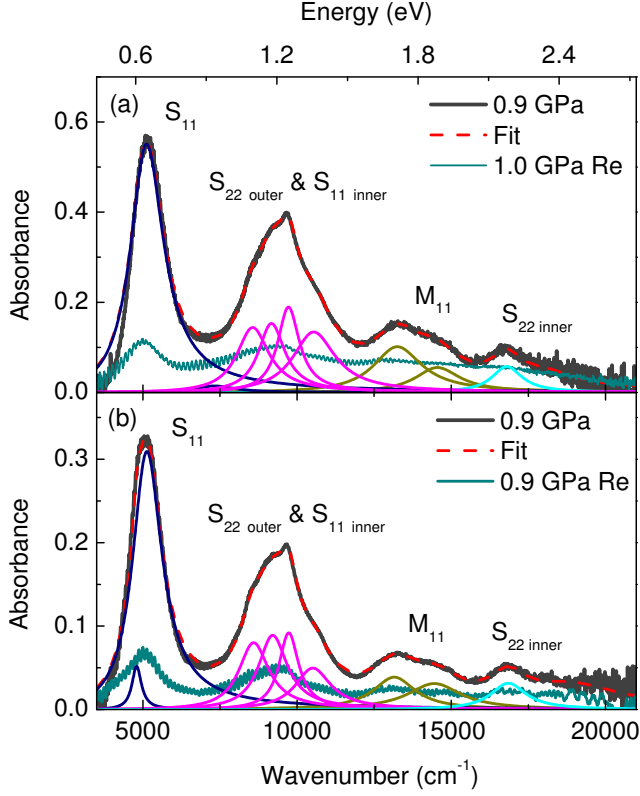
Figure 5.13: Optical absorbance spectrum at the lowest pressure during pressure increase together with the various Lorentzian contributions and the absorbance spectrum at the lowest pressure during pressure release, for the DWCNT/C$_{70}$ film, using (a) nitrogen and (b) argon as PTM in the NIR-VIS range. The labels S$_{ii}$ and M$_{ii}$ denote the *ith* optical transition in semiconducting and metallic tubes, respectively.

notices that the red-shift of the absorption bands is small, with a linear pressure coefficient in the range $\approx$ 15-30 cm^1/GPa [the linear fit is shown in Appendix A Figure 2]. But these values are higher than that of the pressure coefficient values in the case of DWCNTs/C$_{60}$ ($\approx$ 9-15 cm^{-1}/GPa). Above $\approx$ 9 GPa the relative energy shifts of the absorption bands steeply increase and above 14 GPa only the S$_{11}$, S$_{22}$ (1), and S$_{22}$ (3) are resolvable. This behavior signals strong pressure-induced alterations in the electronic properties of the nanotubes at a critical pressure 9 GPa related to tubular deformation. According to the discussion in the subsection 5.2.1, the small red-shift of the absorption bands was explained in terms of the reduction of the σ^*-π^* hybridization and symmetry breaking effects in the outer tubes of the DWCNTs. This behaviour signals the stabilization of the outer tube by the inner tube [185]. Accordingly, the stabilization of the outer tube from the inner tube in the case of DWCNTs/C$_{70}$ is less compared to that in the case of DWCNTs/C$_{60}$. This could be attributed to the larger inner and outer
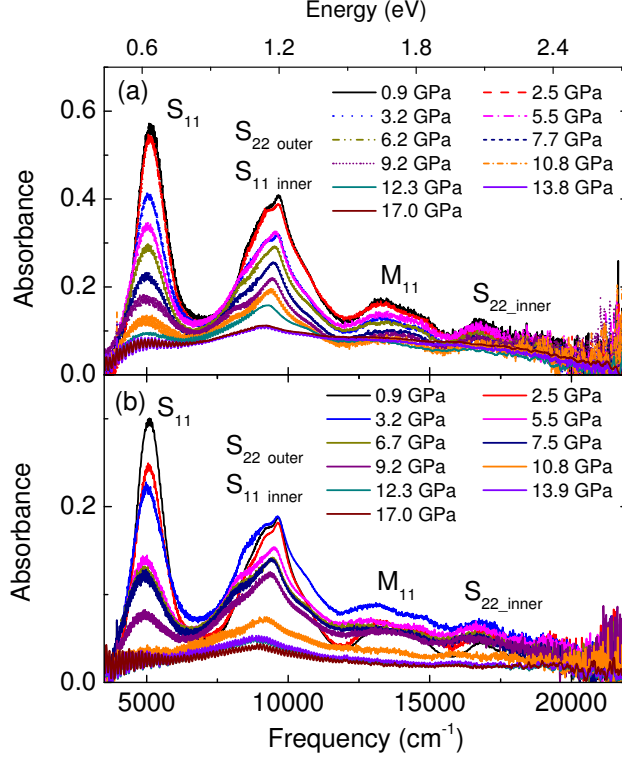
Figure 5.14: Background-subtracted absorbance spectra of DWCNTs/C_{70} as a function of pressure, using (a) nitrogen and (b) argon as PTM.

tubes diameters in the DWCNTs/C_{70} compared to the DWCNTs/C_{60} bundles.

As discussed in the subsection 4.2.1, the filling ratio of the DWCNTs/C_{70} is $\approx$ $\geqslant 90\%$ compared to $\approx$ $\geqslant 95\%$ for the DWCNTs/C_{60}. Also, it has been observed from the HRTEM images, that the DWCNTs/C_{70} bundles contain many short inner tubes which considered as defect according to Aguiar *et al.* [72] [for more HRTEM images for both DWCNTs/C_{60} and DWCNTs/C_{70} bundles defects see Appendix A Figures 3 and 4, respectively]. Aguiar *et al.* [72] have proved that as the number of defects increases in the case of fullerene-derived DWCNTs, the collapse pressure decreases. Also, as the effective tubes diameters increases the collapse pressure decreases [84, 85]. Accordingly, the collapse pressure in the case of the DWCNTs/C_{70} bundles is expected to be lower than the corresponding value in the case of DWCNTs/C_{60} bundles. Similar to the DWCNTs/C_{60}, at 9 GPa, the DWCNTs/C_{70} will deform to the two hexagons.

From the calculated diameters for the DWCNTs/C_{70} bundles from the HRTEM images [see section 4.2.1] and from Raman results [see section 4.2.2.2], an average
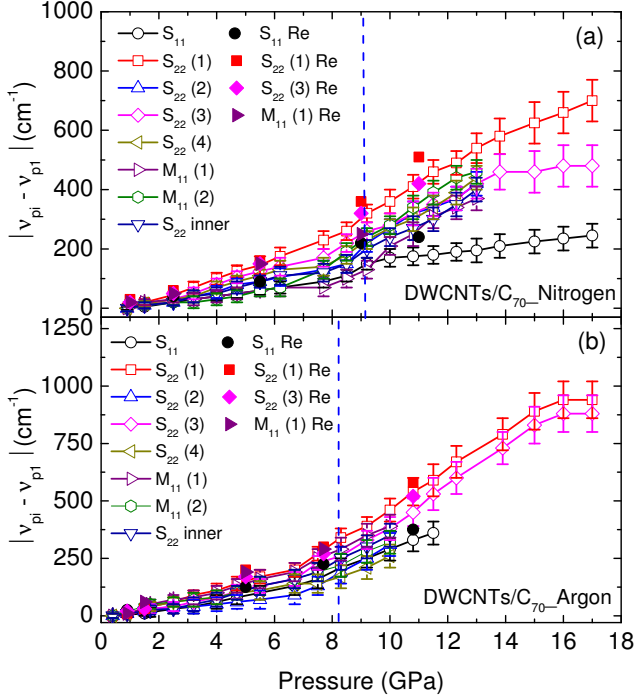
Figure 5.15: Relative energy shift of the optical transitions as a function of pressure in DWCNTs/C$_{70}$ using (a) nitrogen and (b) argon as PTM. The shift was calculated as the difference between the absorption frequency of the contribution ν_{pi} at a pressure pi, and the absorption frequency ν_{p1} at the lowest pressure value $p1$. All the contributions during pressure release are marked as S$_{ii}$ (Re) and M$_{ii}$ (Re) for both semiconducting and metallic tubes, respectively. The vertical dashed, blue lines mark the critical pressures as discussed in the text.

inner and outer nanotubes diameters of d$_{inner} \approx 0.85$ nm and d$_{outer} \approx 1.5$ nm, respectively were estimated. Based on Equation 5.1, the effective radius of the DWCNTs/C$_{70}$ bundles was estimated to be $R_{eff} \approx 0.51$ nm and a critical pressure value of P$_d \approx 11$ GPa was calculated according to Ref. [85]. Thus, the finding of a critical pressure P$_d \approx 9$ GPa in the present work is in a good agreement with theoretical predictions for the onset of the deformations of the tube cross-sections in DWCNTs/C$_{70}$ bundles.

Figure 5.15 (b) depict the relative pressure-induced energy shifts of the Lorentz contributions, using argon as PTM. One can observe that, the critical pressure P$_d\approx$ is lowered to 8 GPa and the red-shifts of the absorption bands is slightly higher than the corresponding values when nitrogen is being used as PTM [see Figure 5.15 (a)]. This could be attributed to the lower hydrostaticity of argon compared to nitrogen as PTM [112].

Figure 5.15 shows the reversibility of the pressure-induced structural changes from the highest applied pressure (≈ 18 GPa) for DWCNT/C$_{70}$ using (a) nitrogen and (b) argon as PTM. The pressure-induced frequency shifts of the optical tran-

sitions are reversible regarding to their frequency position upon pressure release. However, one notices a loss in intensity of the original absorbance value, namely, up to $\approx 80\%$ in the case of nitrogen and argon as PTM [see Figure 5.13]. This value is higher than that obtained for the DWCNT/C$_{60}$ ($\approx 60\%$), indicating the great damage of the DWCNT/C$_{70}$ bundles upon pressure application. This could be due to the lower collapse pressure in the case of DWCNT/C$_{70}$ bundles.

5.3 Peapods under Pressure

In this section the effect of the C$_{60}$ and C$_{70}$ molecules filling on the mechanical stability of the SWCNTs will be discussed.

5.3.1 C$_{60}$-Peapods

Figure 5.16 shows the background-subtracted absorbance spectra as a function of pressure of the C$_{60}$-peapods using (a) nitrogen and (b) argon as PTM for selected pressures up to ≈ 18 GPa. From Figure 5.16, one notices a red-shift of all absorption bands under pressure application. This red-shift is consistent with the earlier observations [167, 168, 185] and it was ascribed to the σ^*-π^* hybridization and symmetry breaking [113, 170, 171]. Besides the red-shift, the absorption bands broaden and lose spectral weight with increasing pressure. In case of the nitrogen data all optical transitions S$_{11}$, S$_{22}$, and M$_{11}$ are resolvable up to the highest applied pressure [see 5.16 (a)]. On the other hand, in case of the argon data all optical transitions are resolvable up to ≈ 12 GPa. Higher than 12 GPa, the optical transitions became very broad specially M$_{11}$ [see Figure 5.16 (b)].

Surprisingly, all the previous high pressure studies on the SWCNTs filled with C$_{60}$, [89, 133, 196–198] investigated only the polymerization and the rotational dynamics of the confined C$_{60}$ molecules inside SWCNTs under high pressure and temperature. Also, the stability of fullerene peapods against hydrostatic pressure has been mainly addressed by experimental techniques which monitor the vibrational properties, like Raman spectroscopy. Only one work was found in the literature on the question of the stability of the C$_{60}$-peapods high pressure up
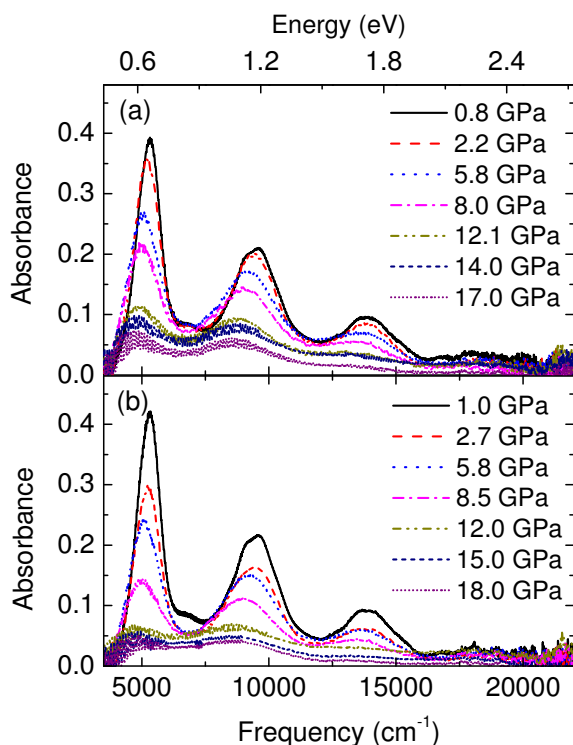
Figure 5.16: Background-subtracted absorbance spectra of C_{60}-peapods as a function of pressure, using (a) nitrogen and (b) argon as PTM.

to 8 GPa using optical spectroscopy [169]. The effect of pressure on the electronic properties of C_{60} peapods was found to be similar to those of the empty SWCNTs. The authors attributed that similarity to the low filling ratio of the peapods.

To clarify the effect of the C_{60} molecules filling on the mechanical stability of the SWCNTs, Figure 5.17(a) shows the relative pressure-induced shifts for the C_{60} peapods under pressure using nitrogen as PTM. First, one notices two anomalies in the pressure-induced shifts at $P_{c1} \approx 6.5$ GPa and $P_{c2} \approx 13$ GPa, followed by a plateau. The plateau with the onset at $P_{c2} \approx 13$ GPa indicates a saturation of the pressure induced deformation and hybridization above this pressure. In general, the relative energy shifts in the case of C_{60}-peapods are quite large compared to the empty SWCNTs [see Figure 5.4 (a)]. This could be explained as follows: it was observed that the centre-to-centre distance between the fullerene molecules in the case of C_{60} peapods decreases with increasing pressure from 0.956 nm to 0.855 nm at 10 GPa [196], forming a closely-packed chains inside the SWCNTs cavity [65, 89]. Also, the C_{60} molecules are known to be very hard molecules, with high bulk modulus [199]. For these reasons, the symmetry breaking in the
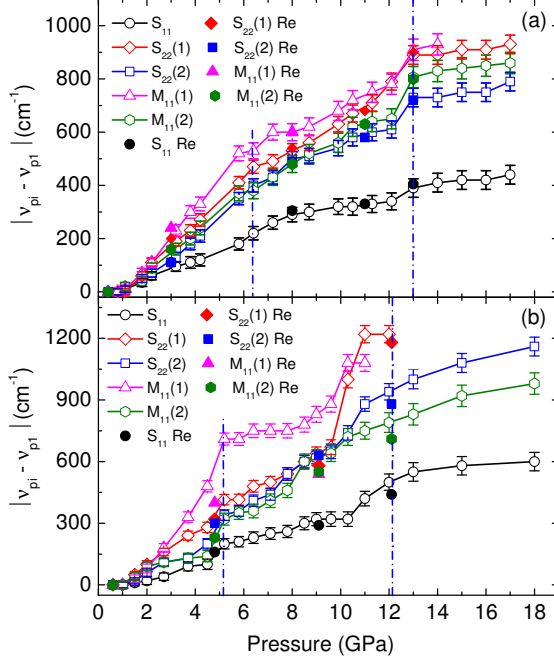
Figure 5.17: Relative energy shift of the optical transitions as a function of pressure in C$_{60}$-peapods using (a) nitrogen and (b) argon as PTM. The shift was calculated as the difference between the absorption frequency of the contribution ν_{pi} at a pressure pi, and the absorption frequency ν_{p1} at the lowest pressure value $p1$. All the contributions during pressure release are marked as S$_{ii}$ (Re) and M$_{ii}$ (Re) for both semiconducting and metallic tubes, respectively. The vertical dashed, blue lines mark the critical pressures as discussed in the text.

outer tubes will be enhanced with increasing pressure and hence large relative pressure induced shifts are expected.

Compared to the empty SWCNTs [see Figure 5.4 (a)], the first structural anomaly is shifted from ≈ 3 GPa to ≈ 6.5 GPa. This behaviour signals the stabilization of the SWCNTs outer wall by the inner fullerene molecules. This finding is in contrast to the expected behaviour of the SWCNTs filled with C$_{70}$ molecules [79, 80, 133]. As mentioned in the literature, that filling of the SWCNTs with C$_{70}$ molecules is considered as a case of inhomogeneous filling and destabilizes the SWCNTs. The destabilization of the nanotubes was attributed to the inhomogeneous interaction, non-covalent van der Waals forces, between the nanotubes wall and the inner molecules, which can lead to the tube mechanical instability at low pressure ≈ 1.1-3.5 GPa [79, 80]. The destabilization of the C$_{70}$ peapods at low pressure could be due to the flipping of the C$_{70}$ molecules from the transverse to the longitudinal position at 1.5 GPa [133]. In the case of C$_{60}$-peapods, such kind of flipping is not expected due to the high symmetry of the C$_{60}$ molecules. Rafailov *et al.* [133] showed that due to the remarkable high elastic modulus of the SWCNTs in the radial direction ≈ 33 GPa [200] and the high bulk modulus of the

encapsulated C$_{60}$ fullerene [199], the applied pressure up to at least 5 GPa is carried predominately by the SWCNTs and then transferred to the the encapsulated C$_{60}$ molecules. Also, a high pressure X-Ray study on the C$_{60}$-peapods by Chorro *et al.* [197] predicted the transformation of the outer walls from the circular to the oval structure at $\approx$ 4 GPa. Accordingly, the anomaly at P$_{c1}$≈6.5 GPa could be attributed to a structural phase transformation from circular to oval shape. Above P$_{c1}$≈6.5 GPa a more drastic ovalization of the outer tubes is expected. Here, the flat or peanut structure is excluded due steric reasons [79]. It is known that intercalated C$_{60}$ fullerene molecules still have high bulk modulus and can be considered as non-deformable molecules [199]. Therefore, the C$_{60}$-peapods at high pressure may be transformed to the oval rather than the flat shape [79].

Recently, a theoretical calculation by Pugno *et al.* [201, 202] estimated the critical deformation pressure of the empty SWCNTs and peapods. The calculations proved such kind of stabilization in the case of the peapods. For the empty SWCNTs the critical pressure P$_c$ defined as

$$P_c = \frac{3N^\alpha D}{R^3} - \frac{\gamma}{R} \tag{5.2}$$

where N is the number of walls, α is constant and in the case of independent tubes $\alpha = 1$, D is the stiffness of graphene and equal to $\approx$ 0.21 nN nm (according to the *ab initio* energy calculations in Ref. [203]), and γ is the surface tension of the nanotubes. The second term is the pressure imposed by the surrounding tubes and the pressure medium, this term is significant only at the nanoscale level. In the case of SWCNTs, with N = 1, R = 0.7 nm, and D = 0.21 nN nm, the expected deformation pressure is $\approx$ 1.8 GPa (neglecting the effect of the surrounding tubes and the PTM). This critical pressure is slightly lower than typical values from earlier theoretical predictions and experimental results [78, 85, 111, 167, 178–184].

In case of the peapods, the critical pressure P$_c$ defined as

$$P_c = \frac{\pi^2 N^\alpha D}{R^3} f - \frac{\gamma}{R} \tag{5.3}$$

where f is the filling ratio of the nanotubes. In the present work, the filling ratio f is close to 1, therefore the expected critical pressure P$_c$ for the peapods is
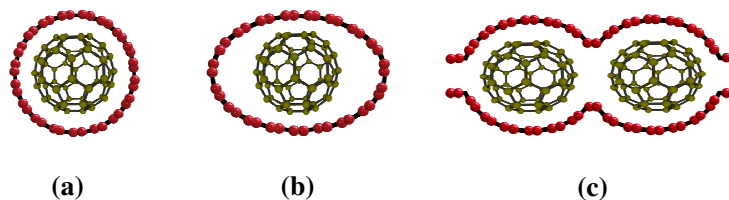
Figure 5.18: Proposed sequence of structural deformation of C$_{70}$-peapods.

6.8 GPa. This value is very close to the experimental value of ≈ 6.5 in case of the nitrogen as a PTM. According to the above discussion, the proposed sequence of the structural deformations in the C$_{60}$-peapods is illustrated in Figure 5.18 (a) to (c).

Figure 5.17 (b) shows the relative pressure-induced redshifts for the C$_{60}$ peapods using argon as PTM. Compared to the nitrogen data [see Figure 5.17 (a)], the anomalies in the pressure-induced shifts are lowered to P$_{c1} \approx$ 5.5 GPa, P$_{c2} \approx$ 12 GPa. Above P$_{c2}$ all the optical transitions S$_{11}$, S$_{22}$, and M$_{11}$ become very broad and can be fitted with one Lorentzian contribution. Also the relative energy shifts are higher than the corresponding shifts, when nitrogen is being used as PTM. The broadening of the absorption bands and the lower relative energy shifts are due to the less-hydrostaticity of the argon compared to nitrogen as pressure transmitting medium [112].

5.3.2 C$_{70}$-Peapods

Figure 5.19 shows the background-subtracted absorbance spectra as a function of pressure for the C$_{70}$-peapods using (a) nitrogen and (b) argon as PTM for selected pressures up to ≈ 18 GPa. One notices a red-shift of all absorption bands under pressure application. This red-shift is ascribed to the σ^*-π^* hybridization and symmetry breaking [113, 170, 171]. Besides the red-shift, the absorption bands are broadened and lost spectral weight with increasing pressure. In the case of nitrogen data all optical transitions S$_{11}$ and S$_{22}$ are resolvable up to ≈ 14 GPa, above this value the M$_{11}$ optical transition is smeared out [see Figure 5.16 (a)]. On the other hand, in the case of argon data, all optical transitions are resolvable up to ≈ 12 GPa. Higher than 12 GPa, the S$_{22}$ optical transition become very
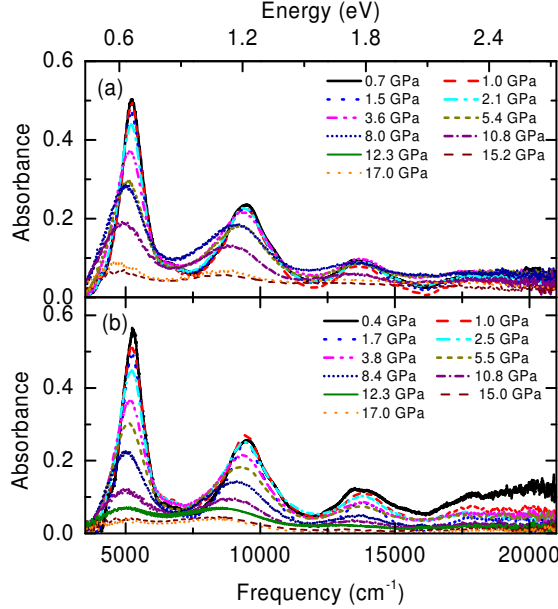
Figure 5.19: Background-subtracted absorbance spectra of C$_{70}$-peapods as a function of pressure, using (a) nitrogen and (b) argon as PTM.

broad and the M$_{11}$ optical transition is smeared out [see Figure 5.19 (b)].

Figure 5.20 (a) shows the relative pressure-induced shifts for the C$_{70}$ peapods under pressure using nitrogen as PTM. One can observe that with increasing pressure, the absorption bands are shifted to lower energies up to certain critical values: P$_{c1}$ ≈ 2 GPa, P$_{c2}$ ≈ 7 GPa, and P$_{c3}$ ≈ 13 GPa, followed by a plateau. Figure 5.20 (c) show only the S$_{11}$ (1) and M$_{11}$ (1) absorption bands to clarify the anomalies positions. The plateau with the onset at P$_{c2}$≈ 13 GPa indicates a saturation of the pressure induced deformation and hybridization above this pressure as discuss before. In general, the relative energy shifts in the case of C$_{70}$-peapods are quite large compared to the empty SWCNTs [see Figure 5.4 (a)]. This behaviour was explained in the subsection 5.3.1.

Compared to the empty SWCNTs [see Figure 5.4 (a)], the first structural anomaly is shifted from ≈ 3 GPa to ≈ 2 GPa. This behaviour signals the destabilization of the nanotubes by the C$_{70}$ fullerene molecules filling. This finding is consistent with the previous Raman studies [79, 80], where they have demonstrated that the filling of SWCNTs with C$_{70}$ molecules is considered as a case of inhomogeneous filling and destabilizes the nanotubes. A high pressure Raman study on C$_{70}$-peapods by Rafailov *et al.* [133], demonstrated that at ≈ 1.5 GPa the C$_{70}$ molecules flipped from the transverse to the longitudinal position. As

discussed in the subsection 4.2.3.2, that a large fraction of the ellipsoidal C_{70} molecules are arranged inside the SWCNTs in the transverse position (with the 0.792 nm axis). Accordingly, the anomaly at $P_{c1} \approx 2$ GPa is attributed to the flipping of the C_{70} fullerene molecules from the transverse to the longitudinal position, leading to a structural phase transformation from the circular to the oval structure. The anomaly at $P_{c2} \approx 7.0$ GPa signals a more drastic change in the tubes' cross section [79, 174, 185]. Above P_{c2} the red-shifts of all the optical absorption bands are increased, this could be attributed to to the inhomogeneous interaction, non-covalent van der Waals forces, between the nanotubes walls and the inner molecules. Here, also the flat or peanut structure is excluded due steric reasons [79].

Figure 5.20 (b) shows the relative pressure-induced redshifts for the C_{70} peapods using argon as PTM. Figure 5.20 (d) shows only the S_{11} (1) and M_{11} (1) absorption bands to clarify the anomalies positions. Compared to the nitrogen data [see Figure 5.20 (a)], the anomalies in the pressure-induced shifts are lowered to $P_{c1} \approx 1.5$ GPa, $P_{c2} \approx 6$ GPa. This could be attributed to less-hydrostaticity of the argon compared to nitrogen as pressure transmitting medium [112].

Regarding the reversibility of the pressure-induced structural changes for both C_{60}- and C_{60}-peapods, the pressure-induced frequency shifts of the optical transitions are reversible upon pressure release from the highest applied pressure (≈ 18 GPa) [see Figures 5.17 and 5.20]. But about $\sim 50\%$ of the original absorbance value for C_{60}- and C_{60}-peapods is lost. This is illustrated in Appendix A Figure 5 (a) and (b), where the absorbance spectra at the lowest pressure during pressure release are included. The irreversible changes indicate that a fraction of the tubes has been permanently damaged during pressure loading.

In Appendix A, Figures 6 and 7 show the behaviour of DWCNT/C_{60}, DWCNT/C_{70}, C_{60} peapods, and C_{70} peapods bundles under pressure in the MIR-FIR region. Since all the carbon nanotubes free-standing films prepared in the present work do not have the same thickness, a quantitative analysis can not be carried out accurately in this region. In general one can observe that the intensity of the absorbance data decreases with increasing pressure as in the case of empty SWCNTs. The interpretation of this behaviour was discussed in detail in subsection 5.1.
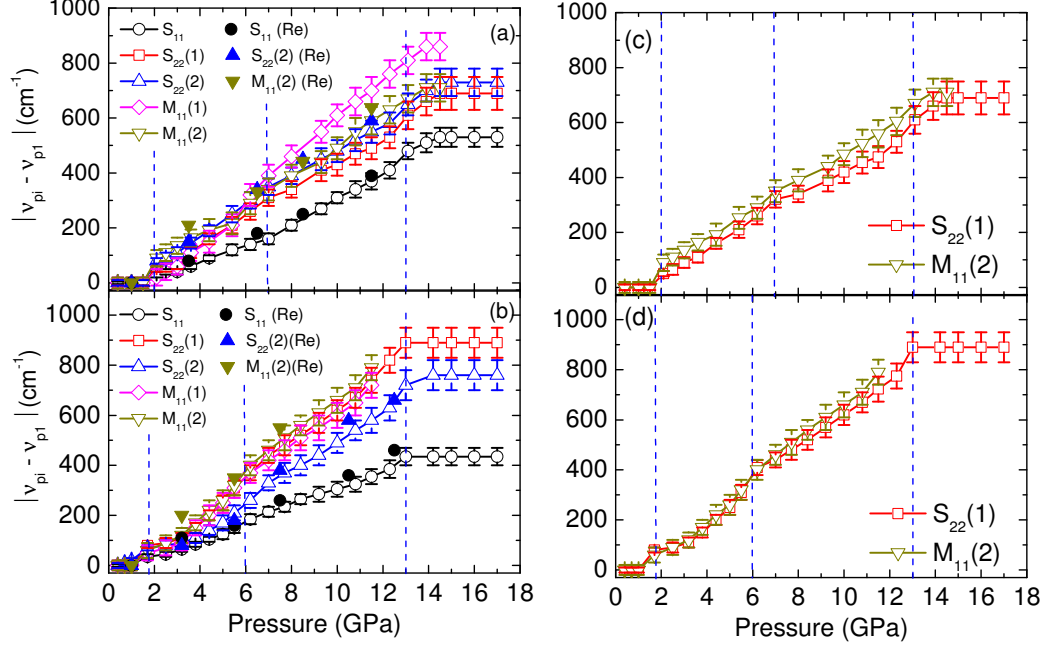
Figure 5.20: Relative energy shift of the optical transitions as a function of pressure in C_{70}-peapods using (a) nitrogen and (b) argon as PTM. The shift was calculated as the difference between the absorption frequency of the contribution ν_{pi} at a pressure pi, and the absorption frequency ν_{p1} at the lowest pressure value $p1$. (c) and (d) show only the S_{11} (1) and M_{11} (1) absorption bands in the case of nitrogen and argon data, respectively, to clarify the anomalies positions. All the contributions during pressure release are marked as S_{ii} (Re) and M_{ii} (Re) for both semiconducting and metallic tubes, respectively. The vertical dashed, blue lines mark the critical pressures as discussed in the text.

5.4 I-SWCNTs under Pressure

Figure 5.21 shows the background-subtracted absorbance spectra as a function of pressure of the I-SWCNTs using nitrogen as PTM for selected pressures up to $\approx$ 17 GPa. One notices a red-shift of all the absorption bands under pressure application. As discussed previously, the red-shift is consistent with earlier observations and ascribed to σ^*-π^* hybridization and symmetry breaking [113, 170, 171]. Besides the red-shift, the absorption bands broaden and lose spectral weight with increasing pressure and all optical transitions S_{11}, S_{22} and M_{11} are resolvable up to the highest applied pressure.

Figure 5.22 shows the relative pressure-induced shifts for the I-SWCNTs film
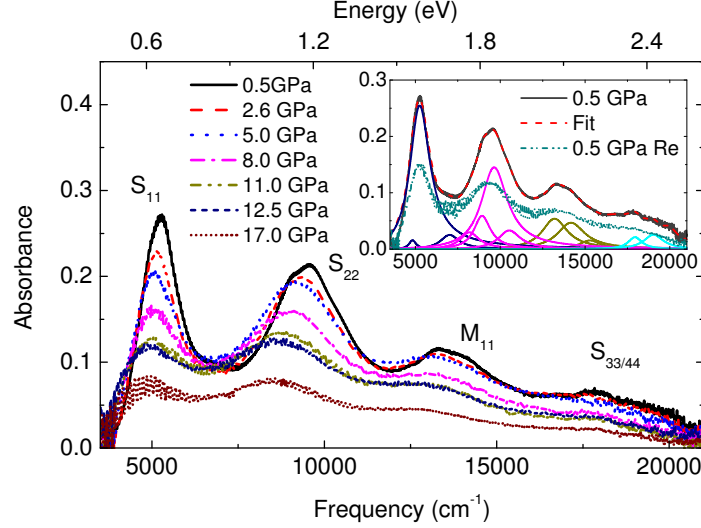
Figure 5.21: Background-subtracted absorbance spectra of I-SWCNTs as a function of pressure, using nitrogen as PTM. The inset shows the back-ground absorbance spectrum at the lowest pressure during pressure increase together with the various Lorentzian contributions and the absorbance spectrum at the lowest pressure during pressure release.

under pressure. The red-shifts of the absorption bands are smaller than that for the SWCNTs filled with C_{60} and C_{70} molecules but the values are comparable to the DWCNTs/C_{70}. The linear pressure coefficient is in the range $\approx$ 30-50 cm^{-1}/GPa [the linear fit is shown in Appendix A Figure 8]. Above $\approx$ 10 GPa the relative energy shifts of the absorption bands steeply increase and seem to saturated. This behavior signals strong pressure-induced alterations in the electronic properties of the outer tube above the critical pressure $P_d \approx$ 10 GPa related to tubular deformation.

The appearance of only one anomaly at $\approx$ 10 GPa signals the stabilization of the nanotubes outer walls by the encapsulated iodine atoms. This finding is in contrast to the expected behaviour of the I-SWCNTs by Alvarez *et al.* [88]. They found that the iodine filling reduces the G-mode collapse pressure value from 10-15 GPa depending on the SWCNTs samples inhomogeneities or different experimental techniques to 7-9 GPa depending on the iodine filling ratio.

Previous high pressure Raman study by Venkateswaran *et al.* [204] on I-SWCNTs bundles, showed that iodine atoms can reside not only inside the SWCNTs but also intercalate between the SWCNTs bundles pores. At ambient con-
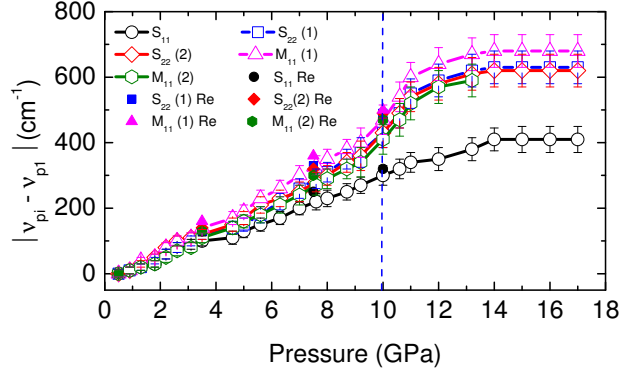
5. I-SWCNTs under Pressure

Figure 5.22: Relative energy shift of the optical transitions as a function of pressure in I-SWCNTs using nitrogen as PTM. All the contributions during pressure release are marked as S_{ii} (Re) and M_{ii} (Re) for both semiconducting and metallic tubes, respectively. The vertical dashed, blue line marks the critical pressure as discussed in the text.

ditions, the average diameter of the pores between the nanotubes bundles is $\approx$ 0.3 nm which is enough to accommodate the short I_3^- polyiodide chains, where the long I_5^- or I_7^- polyiodide chains can reside inside the SWCNTs cavity. Aguiar *et al.* [72] showed that in the case of DWCNTs doped with Br atoms, the lower collapse pressure was attributed to the rearrangement of the Br atoms between the interstitial channels of the DWCNTs bundles which could induced uniaxial stress in the radial direction of the DWCNTs, thus leading to lower collapse pressure.

But in the present work after the preparation of the I-SWCNTs film [see subsection 4.1.2.2 and 3.4] the free-standing film was immersed in an ethanol path for 30 mins to remove any excess adsorbed iodine atoms. Therefore, after the purification steps it is believed that only iodine atoms are reside in the SWCNTs cavity. This means the destabilization effect of intercalated iodine atoms according to Ref.[72] can be excluded.

A HRTEM study on the I-SWCNTs by Guan *et al.* [119] has shown that the 1.4 nm SWCNTs can accommodate three helical chains from the negatively charged iodine atoms. Also, the study showed that due the filling with the negatively charged iodine helical chains, the diameter of the nanotubes increased due to the repulsion between the iodine chains. The same behaviour was also observed by a HRTEM study on the SWCNTs filled with helical one-dimensional
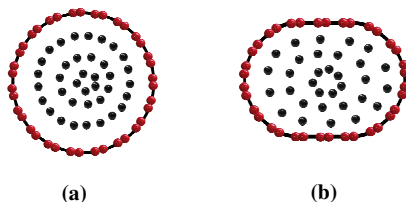
(a)   (b)

Figure 5.23: Proposed sequence of structural deformation of I-SWCNTs.

cobalt diiodide by Philp *et al.* [205]. A theoretical study by Shanavas *et al.* [87] on the stability of the nanotubes encapsulating argon atoms, demonstrated that as the argon atoms density increases $\geqslant 60$ atoms/tube, the interactions between the argon atoms and the SWCNT wall will be repulsive adding an outward force against the applied external pressure, thus leading to stabilization of the tubes against the applied pressure. The study showed that, under high pressure the nanotube deformed to two deformed hexagons as the case of DWCNTs. Accordingly, the stabilization of the SWCNTs by the iodine filling in the present work can be explained as follows: since the average diameter of the SWCNTs in the present work is ≈ 1.4 nm, therefore the SWCNTs will be filled with three negatively charged iodine helical chains (according to Ref. [87]). The repulsive forces between the iodine chains will exert an outward force on the SWCNT, supporting the SWCNTs against the applied pressure, leading to a stabilization of the nanotubes. The proposed deformation scheme in the case of I-SWCNTs is shown in Figure 5.23 based on the theoretical prediction of Ref. [87].

Figure 5.24 shows the absorbance spectra of the I-SWCNT film for selected pressures up to 13 GPa in the MIR and FIR frequency ranges (200-7000 cm^{-1}). One can observe that the absorbance level decreases monotonically with increasing pressure. This behaviour was explained previously and attributed to an increase in the symmetry breaking and σ^*-π^* hybridization with applying pressure, leading to a destruction of the SWCNTs' electronic band structure and consequently a decrease in the conductivity level of the SWCNTs. But in the case of I-SWCNTs compared to the SWCNTs, one can observe that the absorbance level in the FIR even at the highest applied pressure ≈ 13 GPa is still high compared to the same pressure value in the case of empty SWCNTs which looks flat [see Figure 5.6]. According to Alvarez *et al.* [88], as the pressure increases the intermolecular
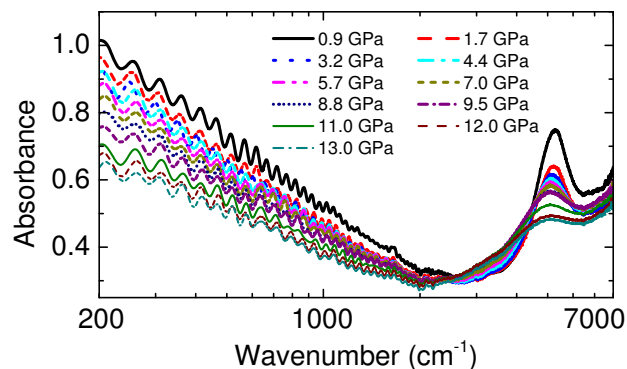
Figure 5.24: Absorbance spectra of the I-SWCNTs film for selected pressures up to 13 GPa over a broad frequency range (200-7000 cm^{-1}) in MIR-MIR region.

interaction between the polyiodide chains becomes more important, leading to a charge delocalization outside the polyiodide chains. This behaviour was also observed in iodine single crystal [206, 207] and ascribed to the metallization transition under pressure. This means that the loss of the absorption intensity due to the destruction of the SWCNTs band structure will be compensated by the metallization of the iodine chains under pressure.
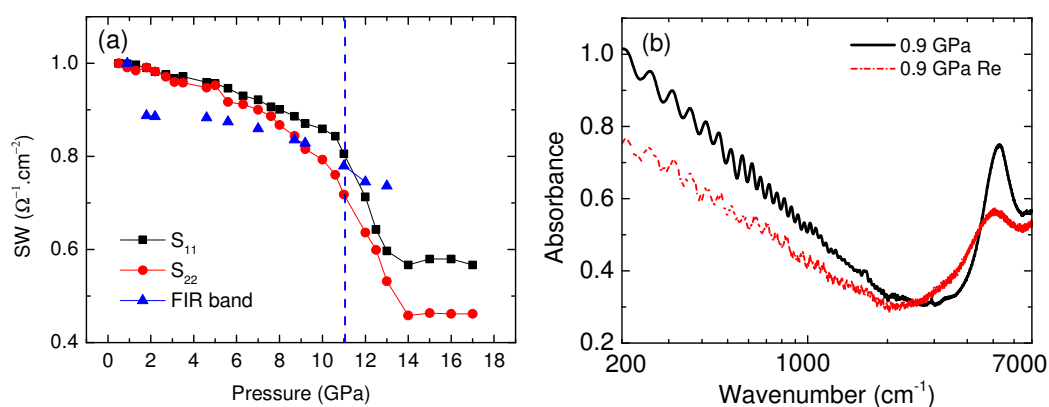

Figure 5.25: (a) Spectral weight of S$_{11}$, S$_{22}$, and FIR absorption bands for I-SWCNTs as a function of pressure using nitrogen as a pressure transmitting medium. (b) Absorbance spectra of the SWCNTs film at the lowest pressure during pressure increase together with the lowest pressure during pressure release in MIR-MIR region.

Figure 5.25 (a) shows the normalized spectral weight of the S$_{11}$, S$_{22}$, and FIR

absorption bands for I-SWCNTs as a function of pressure using nitrogen as a PTM. One can observe that the spectral weights of the S_{11} and S_{22} absorption bands show only anomaly in the dimensionality of the system at $P_{c1} \approx 11.0$ GPa. This values is consistent with the calculated value from the relative pressure-induced energy shifts (≈ 10 GPa) [see Figure 5.22]. The spectral weight of the FIR band does not show any clear anomaly with pressure. Also, the normalized spectral weight is relatively low compared to both S_{11}, S_{22} absorption bands. This behaviour confirms our results, that with applying pressure the charge delocalization outside the polyiodide chains will compensate the loss of the spectral weight due to the destruction of the nanotubes band structure and hence increases the conductivity level in the FIR region.

Figure 5.25 (b) shows the reversibility of the pressure-induced structural changes for I-SWCNTs in the FIR region. One notices a loss in the intensity of the original absorbance value up to $\approx 40\%$. This value is higher than corresponding loss calculated from the optical measurements in the NIR-VIS region ($\approx 50\%$) [see the inset of Figure 5.21]. As we discussed before in the case of SWCNTs this could attributed to the lower applied pressure value (≈ 13 GPa) in the FIR measurements compared to ≈ 18 GPa in the case of optical measurements.

5.5   Summary

Pressure-dependent absorption measurements on SWCNTs, C_{60}, C_{70} peapods, DWCNTs/C_{60}, DWCNTs/C_{70}, and I-SWCNTs films were performed over a broad energy range from FIR to VIS range up to 20 GPa. With increasing pressure all absorption bands red-shift, broaden, and lost spectral weight. This behaviour is most likely due to the symmetry breaking and σ^*-π^* hybridization with applying pressure. In the case of SWCNTs under pressure using nitrogen as PTM, the relative pressure-induced shifts show three anomalies at $P_{c1} \approx 3$ GPa, $P_{c2} \approx 7$ GPa, and $P_{c3} \approx 13$ GPa, followed by a plateau. The critical pressures at which the anomalies occur are in agreement with that expected according to theoretical experimental results. The anomaly at P_{c1} is due to a structural phase transition from the circular to an oval shape. The anomaly at P_{c2} signals a more drastic change in the tubes' cross section from oval to race-track or peanut-type shape.

The anomaly at $P_{c3} \approx$ 13 GPa is due to the collapse of the nanotubes. The plateau above 13 GPa indicates a saturation of the pressure-induced deformation and hybridization effects above this pressure.

Compared to empty SWCNTs, the pressure-induced shifts of the absorption bands in DWCNTs/C_{60} are smaller and follow an approximately linear behavior with a pressure coefficient in the range $\approx$ 9-15 cm^1/GPa. The reduced redshift indicates that the outer tube is stabilized by the inner tube regarding its electronic properties. The anomaly in the pressure-induced shift at $\approx$ 12 GPa signals the onset of deformation of the outer tubes, where a small discontinuous volume change occurs, accompanied by a cross sections' change to two deformed hexagons. The finding of a critical pressure $P_d \approx$ 12 GPa in the present work is in a good agreement with theoretical predictions for the onset of the deformations of the tube cross-sections in DWCNTs bundles and also with the experimental results of the C_{60}-peapods-derived DWCNTs.

In the case of DWCNTs/C_{70}, the pressure-induced shifts of the absorption bands are higher than those of the DWCNTs/C_{60}, with a linear pressure coefficient in the range $\approx$ 15-30 cm^1/GPa below 9 GPa. The anomaly in the pressure-induced shift was lowered to 9 GPa compared to 12 GPa in the case of DWCNTs/C_{60}. This behaviour signals that the stabilization of the outer tube by the inner tube is lower compared to the DWCNTs/C_{60}.

Compared to the empty SWCNTs, the filling with C_{60} molecules in the case of C_{60} peapods shifts the first structural anomaly at $\approx$ 3 GPa to $\approx$ 6.5 GPa. This behaviour signals the stabilization of the outer tube by the inner fullerene molecules. This value is in a good agreement with the theoretical prediction. At $P_{c2} \approx$ 13 GPa a more drastic ovalization of the outer tubes occurs but the flat or peanut structure is excluded due steric reasons because of the high bulk modulus of the C_{60} molecules. On the other hand, filling the tubes with C_{70} molecules destabilizes the outer tube due the flipping of the C_{70} molecules from the transverse to the longitudinal arrangement, leading to a structural phase transformation from the circular to an oval structure at $\approx$2 GPa. Here, also the flat or peanut structure deformation is excluded. This is in a good agreement with Raman results.

Interestingly, the iodine filling in the case of I-SWCNTs shows a stabilization

for the outer tubes up to 10 GPa in contrast with the previously published Raman results. This behaviour was attributed to the repulsion forces between the negatively charged polyiodide chains, exerting an outward force on the SWCNT, leading to a stabilization of the nanotubes.

The results show a comparison on the effect of different PTM on the stability of the nanotubes under investigation. Nitrogen shows a better hydrostaticity compared to argon and alcohol-mixture as PTM. In the case of argon, the relative energy shifts are higher than the corresponding shifts, when nitrogen is being used as PTM. Alcohol-mixture is a hydrostatic PTM below 10 GPa but becomes quasi-hydrostatic above 10 GPa due to solidification. Therefore, above 10 GPa nanotubes are completely collapsed due to the solidification. Interestingly, the SWCNTs filling with nitrogen, argon, or alcohol-mixture does not prevent the pressure-induced anomalies in the electronic transitions due to tubular deformation in contradiction to earlier Raman results. For all samples under investigation, the pressure-induced alterations of the absorption bands are reversible regarding their frequency position, but not completely reversible regarding their intensity, indicating that a fraction of the tubes has been permanently damaged under high pressure.

In the low energy range from 200-700 cm^{-1} SWCNTs, the absorbance level decreases with increasing pressure and at high pressure values it looks flat. the decrease of the absorbance level in the FIR is due to (i) the destruction of the nanotub' electronic band structure and/or (ii) a decrease of the the localization length of the carriers, leading to a decrease in the conductivity level of the nanotubes. In the case of I-SWCNTs, the loss of the absorption intensity due to the destruction of the SWCNTs band structure is compensated by the metallization of the iodine chains under pressure.

Chapter 6

Conclusions and outlook

As a part of this project, the preparation of high-yield C_{60}, C_{60} peapods, DWC-NTs derived from the peapods, and iodine-fillled SWCNTs atoms was performed. The prepared samples were characterized by HRTEM, Raman, and optical spectroscopy. The effects of the interaction between the fillers (fullerene molecules, inner wall, and iodine atoms) and the SWCNT on the electronic and vibrational properties were discussed. Pressure-dependent optical spectroscopy and infrared measurements on the stability of SWCNTs, C_{60}, C_{70} peapods, DWCNTs/C_{60}, DWCNTs/C_{70}, and I-SWCNTs films were performed over a broad energy range from FIR to VIS range up to $\approx$ 20 GPa. Also, the effect of the different PTM on the stability of the nanotubes under investigation were discussed.

HRTEM images showed that DWCNTs/C_{60} and DWCNTs/C_{70} were prepared from the highly filled C_{60} ($\geqslant$ 95%) and C_{70} ($\geqslant$ 90%) peapods, respectively. From the HRTEM images, the average outer tubes diameters were found to be 1.5 and 1.6 nm in the case of DWCNTs/C_{60} and DWCNTs/C_{70}, respectively.

In the case of C_{60}-peapods, the charge transfer between the C_{60}-molecules and the tube wall causes a softening of the C-C bonds in the nanotube, shifting the RBMs to lower frequencies. On the other hand, the RBMs in the case of C_{70}-peapods are not affected by the filling with C_{70} molecules. In the case of I-SWCNTs the formation of I_n^- polyiodide chains inside the SWCNTs was found. Compared to the SWCNTs, the RBMs in the case of DWCNTs/C_{60} and DWCNTs/C_{70} were shifted to lower frequencies due to the tubes fattening during the heat treatment.

Filling the tubes with C_{60} molecules shifts the G-modes to higher energies due to the radial overlapping between the fullerene molecules and the tubes, while in the case of C_{70}-peapods the charge transfer or the interaction between the C_{70} molecules and the outer tube seems to be too small to be observable in the Raman data. In contrast to the fullerene peapods, the G-lines in I-SWCNTs are upshifted by $\approx$ 9-18 cm^{-1} compared to the empty SWCNTs due to the electron transfer from the SWCNTs to the iodine. In the case of DWCNTs/C_{60}, and (c) DWCNTs/C_{70}, the charge transfer or the interaction between the inner and outer tubes seems to be too small to be observed in the Raman data.

In comparison with SWCNTs all the optical transitions are shifted to higher energies in the case of C_{60} peapods due to the reduction of the effective tube diameter, whereas no significant shifts were observed for the C_{70}-peapods. In the case of DWCNTs/C_{60} and DWCNTs/C_{70} all the optical transitions are shifted to lower energies due to the tubes fattening. The S_{11}/S_{22} spectral weight ratio in the case of I-SWCNTs is smaller than the empty SWCNTs due to the electrons removal from the valence band of the nanotube.

Pressure-dependent optical spectroscopy measurements on SWCNTs, C_{60}, C_{70} peapods, DWCNTs/C_{60}, DWCNTs/C_{70}, and I-SWCNTs film were performed over a broad energy range from FIR to VIS range up to 20 GPa. With increasing pressure all absorption bands red-shift, broaden, and lost spectral weight. This behaviour is most likely due to the symmetry breaking and σ^*-π^* hybridization with applying pressure. In the case of SWCNTs under pressure using nitrogen as PTM, the relative pressure-induced shifts show three anomalies at $P_{c1} \approx$ 3 GPa, $P_{c2} \approx$ 7 GPa, and $P_{c3} \approx$ 13 GPa, followed by a plateau. The anomaly at P_{c1} is due to a structural phase transition from the circular to an oval shape. The anomaly at P_{c2} signals a more drastic change in the tubes' cross section from oval to race-track or peanut-type shape. Where, the anomaly at $P_{c3} \approx$ 13 GPa is due to the collapse of the nanotubes. The plateau above 13 GPa indicates a saturation of the pressure-induced deformation and hybridization effects above this pressure.

Compared to empty SWCNTs, the pressure-induced shifts of the absorption bands in the DWCNTs/C_{60} are smaller indicating that the outer tube is stabilized by the inner tube regarding its electronic properties. The anomaly in the pressure-induced shift at $\approx$ 12 GPa signals the onset of deformation of the

outer tubes, where a small discontinuous volume change occurs, accompanied by a cross sections' change to two deformed hexagons. Whereas, in the case of DWCNTs/C_{70}, the stabilization of the outer tube by the inner tube is less compared to the DWCNTs/C_{60} and the anomaly in the pressure-induced shift is lowered to $\approx$ 10 GPa.

Compared to the empty SWCNTs, the filling with C_{60} molecules in the case of C_{60} peapods shifts the first structural anomaly at $\approx$ 3 GPa to $\approx$ 6.5 GPa. This behaviour signals the stabilization of the outer tube by the inner fullerene molecules. While, filling the tubes with C_{70} molecules destabilizes the outer tube due the flipping of the C_{70} molecules from the transverse to the longitudinal arrangement, leading to a structural phase transformation from the circular to an oval structure at $\approx$2 GPa.

Interestingly, the iodine filling in the case of I-SWCNTs shows a stabilization for the outer tubes up to 10 GPa. This behaviour is attributed to the repulsion forces between the negatively charged polyiodide chains, exerting an outward force on the SWCNT, leading to a stabilization of the nanotubes.

The results show a compassion on the effect of different PTM on the stability of the nanotubes under investigation. Nitrogen shows a better hydrostaticity compared to argon and alcohol-mixture as PTM. For all samples under investigation, the pressure-induced alterations of the absorption bands are reversible regarding their frequency position, but not completely reversible regarding their intensity, indicating that a fraction of the tubes has been permanently damaged under high pressure.

In the low energy range from 200-700 cm^{-1}, the absorbance level of the SWCNTs decreases with increasing pressure and at high pressure values it looks flat. The decrease of the absorbance level in the FIR is attributed to (i) the destruction of the nanotub' electronic band structure and/or (ii) a decrease of the the localization length of the carriers, leading to a decrease in the conductivity level of the nanotubes. In the case of I-SWCNTs, the lose of the absorption intensity due to the destruction of the SWCNTs band structure is compensated by the metallization of the iodine chains under pressure.

Thus, the pressure-induced phenomena in the electronic band structure of the SWCNTs filled with fullerene molecules, inner wall, and iodine atoms have been

extensively studied by optical properties of the samples under pressure.

Finally, I put some suggestions for the future work on carbon nanotubes under pressure:

- The purifying the SWCNTs film under high temperature and dynamic vacuum should remove all the chemical groups attached to the surface of the SWCNTs. This will enhance the visibility of the IR-active modes and enable us to study the behaviour of theses modes pressure.

- All the SWCNTs in the present work are a mixture from semiconducting and metallic tubes and also contain different diameter distribution. Therefore, the analysis of the Raman spectra or the optical absorption bands is somehow complicated. Recently K. Yanagi *et al.* [128], isolated single chirality (11,10) SWCNTs from a mixture of different nanotubes chiralities. The Raman scattering peaks and the optical absorption bands of the single chirality (11,10) SWCNTs have smaller FWHM compared to the mixture chiralities sample. So, the analysis of the optical absorption bands will be quite simple.

- The effect of argon and nitrogen as PTM does not prevent the pressure-induced anomalies in the electronic transitions due to tubular deformation as expected by Raman studies. Argon and nitrogen used in the present work are cryogenic fluids and with increasing pressure they solidify. Therefore, the probability of filling the tubes with argon or nitrogen fluids will be very low with applying pressure. Therefore, the nanotubes can be filled with nitrogen or argon in the gas phase similar to the peapods method and after that the effect of the pressure on the stability of the SWCNTs filled with argon or nitrogen gas can be performed using different PTMs.
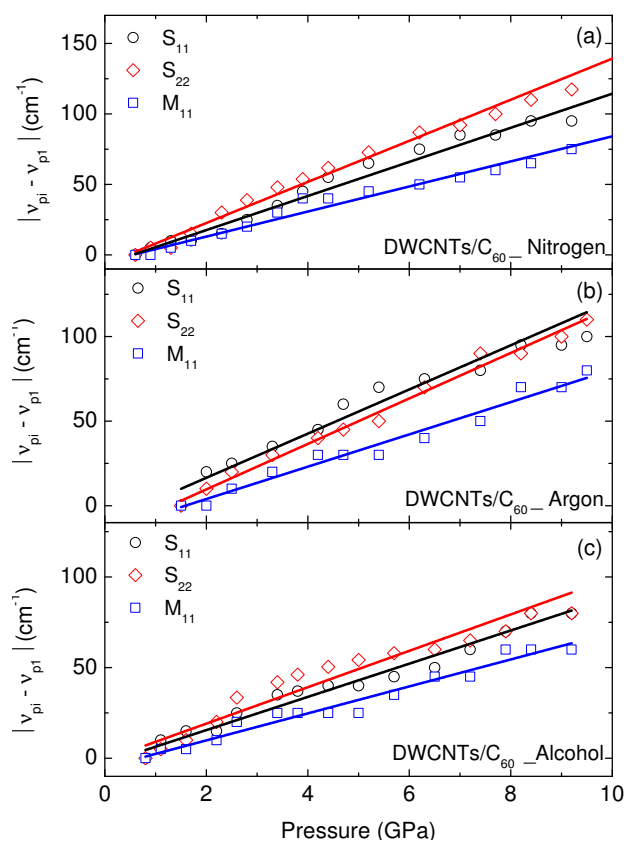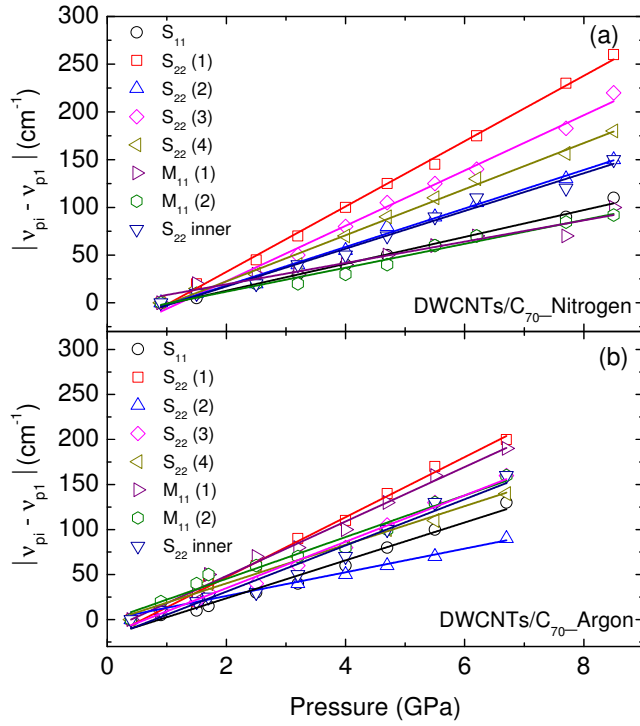
Appendix A

Figure 1: The solid lines show the linear fit for the relative energy shift of the optical transitions as a function of pressure in DWCNTs/C_{60} using (a) nitrogen, (b) argon, and (c) alcohol-mixture as PTM. The values are in the range $\approx$ 9-15 cm^{-1}/GPa

Figure 2: The solid lines show the linear fit for the relative energy shift of the optical transitions as a function of pressure in DWCNTs/C_{70} using (a) nitrogen and (b) argon as PTM. The values are in the range $\approx$ 15-30 cm^{-1}/GPa
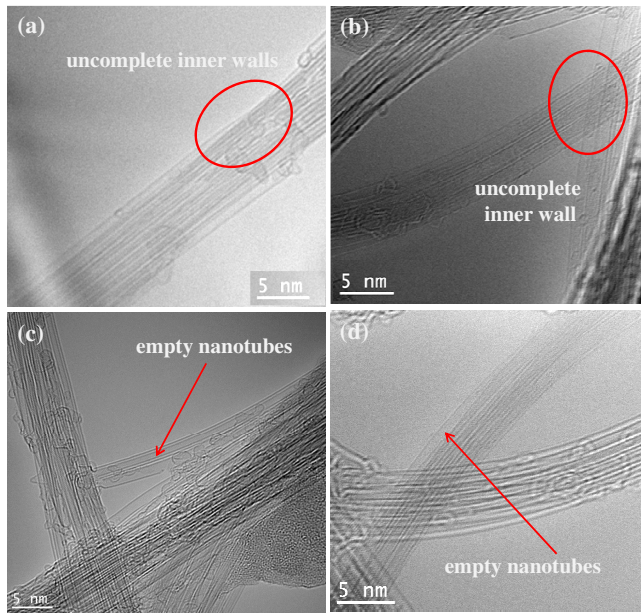

Figure 3: HRTEM images for DWCNTs/C_{60} showing different defects from the transformation of the C_{60} molecules to inner tube. (a) and (b) show uncomplete inner tubes and (c) and (d) show empty nanotubes.
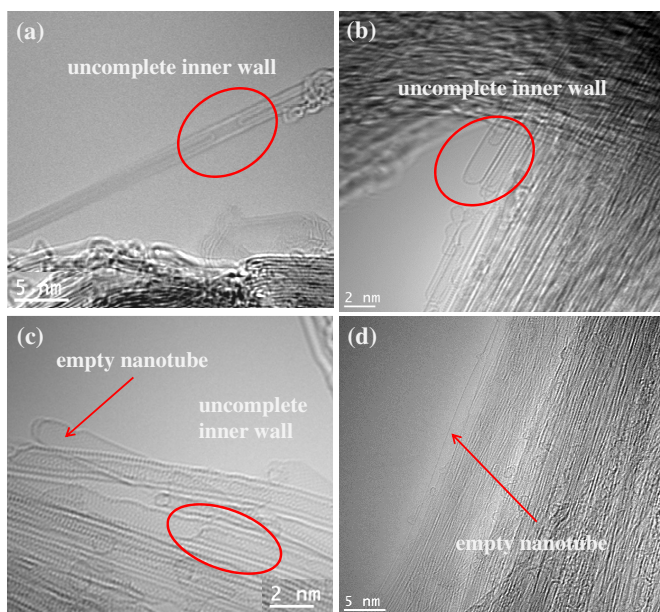
Figure 4: HRTEM images for DWCNTs/C_{70} showing different defects from the transformation of the C_{70} molecules to inner tube. (a) and (b) show uncomplete inner tubes and (c) and (d) show empty nanotubes.
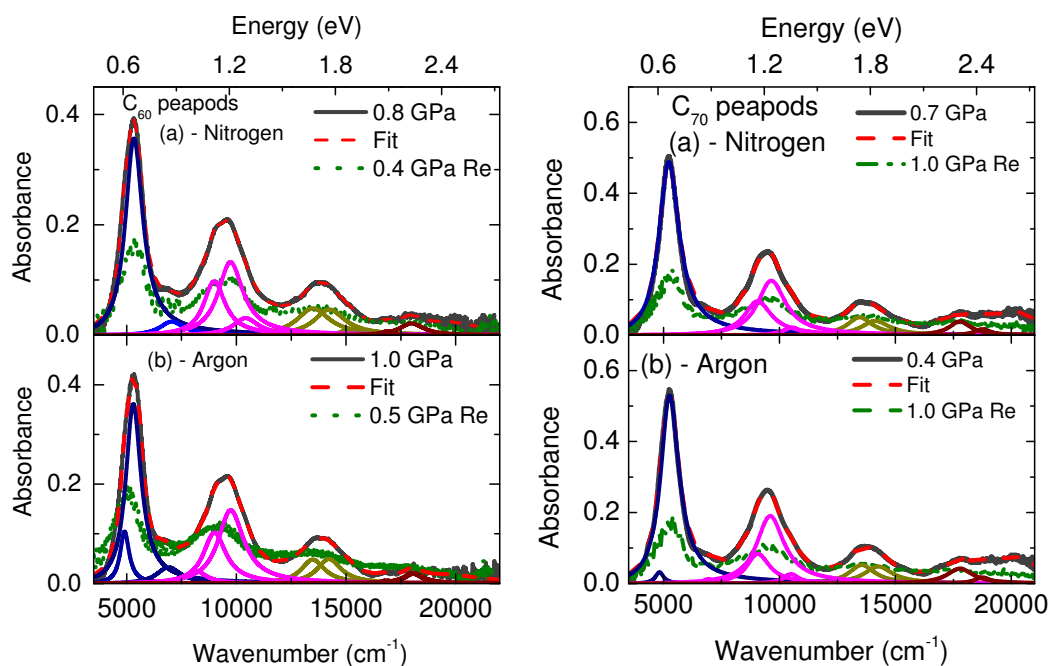
Figure 5: Left panel shows the optical absorbance spectrum at the lowest pressure during pressure increase together with the various Lorentzian contributions and the absorbance spectrum at the lowest pressure during pressure release, for the C_{60} peapods, using (a) nitrogen, (b) argon as PTM in the NIR-VIS range. Right panel shows the optical absorbance spectrum at the lowest pressure during pressure increase together with the various Lorentzian contributions and the absorbance spectrum at the lowest pressure during pressure release, for the C_{70} peapods, using (a) nitrogen, (b) argon as PTM in the NIR-VIS range.
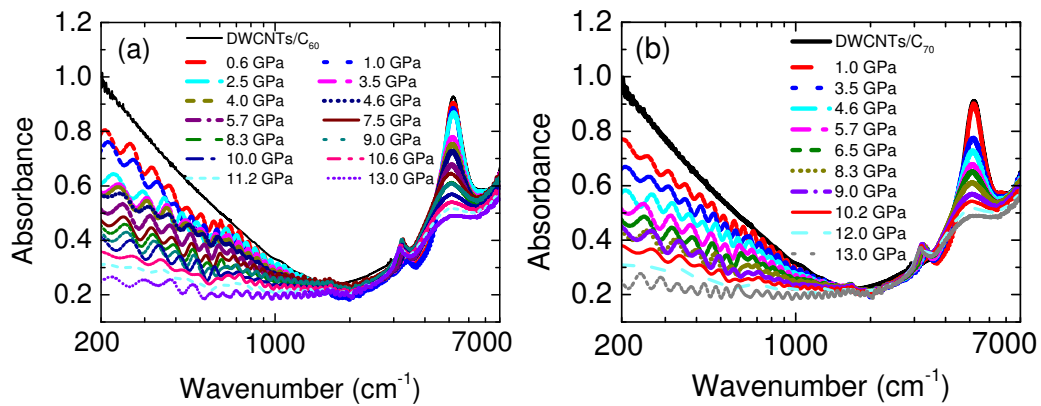
Figure 6: Absorbance spectra of (a) DWCNTs/C_{60} and (b) DWCNTs/C_{70} films for selected pressures up to 13 GPa over a broad frequency range (200-7000 cm^{-1}) in MIR-FIR region using nitrogen as PTM.
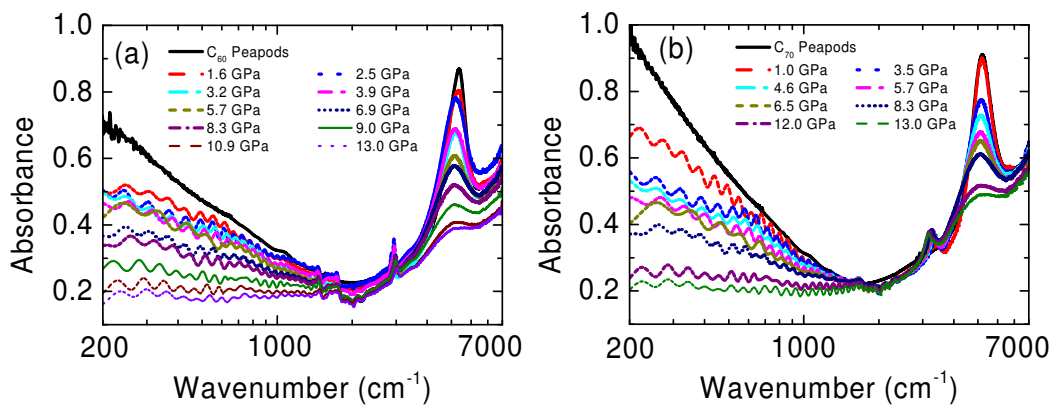

Figure 7: Absorbance spectra of (a) C_{60} peapods and (b) C_{70} peapods films for selected pressures up to 13 GPa over a broad frequency range (200-7000 cm^{-1}) in MIR-FIR region using nitrogen as PTM.
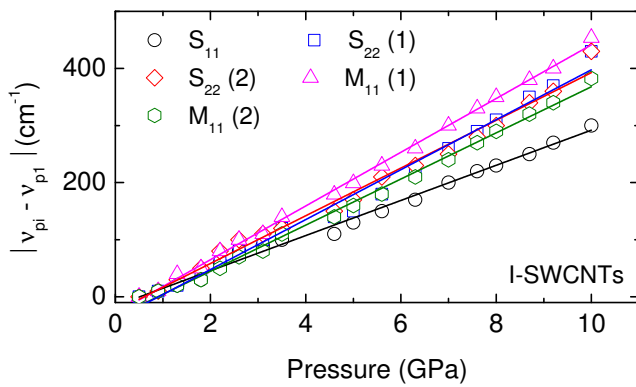
Figure 8: The solid lines show the linear fit for the relative energy shift of the optical transitions as a function of pressure in I-SWCNTs using nitrogen as PTM. The values are in the range $\approx$ 30-50 cm^{-1}/GPa

References

[1] A. K. Geim and K. S. Novoselov, Nat. Mater. **6**, 183 (2007).

[2] P. R. Wallace, Phys. Rev. **71**, 622 (1947).

[3] K. S. Novoselov, A. K. Geim, S. V. Morozov, D. Jiang, Y. Zhang, S. V. Dubonos, I. V. Grigorieva, and A. A. Firsov, Science **306**, 666 (2004).

[4] K. S. Novoselov, D. Jiang, F. Schedin, T. J. Booth, V. V. Khotkevich, S. V. Morozov, and A. K. Geim, Proc. Natl Acad. Sci. USA **102**, 10451 (2005).

[5] D. S. L. Abergel, A. Russell, and V. I. Falko, Appl. Phys. Lett. **91**, 063125 (2007).

[6] E. Y. Andrei, G. Li, and X. Du, Rep. Prog. Phys. **75**, 056501 (2012).

[7] W. Andreoni, *The Physics of Fullerene-Based and Fullerene-Related Materials* (Springer, Berlin, 2000).

[8] R. Saito, G. Dresselhaus, and M. S. Dresselhaus, *Physical Properties of Carbon Nanotubes* (Imperial College Press, London, 1998).

[9] A. H. Castro Neto, F. Guinea, N. M. R. Peres, K. S. Novoselov, and A. K. Geim, Rev. Mod. Phys. **81**, 109 (2009).

[10] A. Jorio, R. Saito, G. Dresselhaus, and M. S. Dresselhaus, *Raman Spectroscopy in Graphene Related Systems* (WILEY-VCH Verlag GmbH, Germany, 2011).

[11] http://jahschem.wikispaces.com/bonding.

REFERENCES

[12] N. W. Ashcroft and N. D. Mermin, *Solid State Physics* (Harcourt College Publishers, USA, 1976).

[13] A. H. Castro Neto, F. Guinea, N. M. R. Peres, K. S. Novoselov, and A. K. Geim, Rev. Mod. Phys. **81**, 109 (2009).

[14] P. Avouris, Nano Lett. **10**, 4285 (2010).

[15] M. I. Katsnelson, Mater. Today **10**, 20 (2007).

[16] M. S. Fuhrer, Nature Mater. **9**, 1099 (2010).

[17] http://demonstrations.wolfram.com/GrapheneBrillouinZone.

[18] G. S. Painter and D. E. Ellis, Phys. Rev. B **1**, 4747 (1970).

[19] M. S. Dresselhaus, G. Dresselhaus, K. Sugihara, I. L. Spain, and H. A. Goldberg, *Graphite Fibers and Filaments* (Springer Series in Materials Science, Springer-Verlag,Berlin., 1988).

[20] R. Saito, A. Grneis, G. Samsonidze, G. Dresselhaus, M. Dresselhaus, A. Jorio, L. Canado, M. Pimenta, and A. Souza Filho, Appl. Phys. A Mater. Sci. Process. **78**, 1099 (2004).

[21] G. G. Samsonidze, A. Saito, D. Jorio, E. Pimenta, E. Souza Filho, F. Gruneis, D. Dresselhaus, and M. Dresselhausa, J. Nanosci. Nanotechnol. **3**, 431 (2003).

[22] J. W. G. Wilder, L. C. Venema, A. G. Rinzler, and C. Dekker, Nature **391**, 59 (1998).

[23] http://www.fisica.unam.mx/cecilia/nanotubos.jpg.

[24] M. Dresselhaus, G. Dresselhaus, R. Saito, and A. Jorio, Phys. Rep. **409**, 47 (2005).

[25] M. Burghard, Surf. Sci. Rep. **58**, 1 (2005).

[26] C. T. White and J. W. Mintmire, Nature **394**, 29 (1998).

REFERENCES

[27] J.-C. Charlier and P. Lambin, Phys. Rev. B **57**, R15037 (1998).

[28] J. W. Mintmire and C. T. White, Phys. Rev. Lett. **81**, 2506 (1998).

[29] S. Reich, C. Thomsen, and Maultzsch, *Carbon nanotubes: Basic concepts and physical properties* (WILEY-VCH Verlag GmbH, Germany, 2004).

[30] J. Kürti, V. Zlyomi, M. Kertesz, and G. Sun, New J. Phys. **5**, 125 (2003).

[31] R. Saito, G. Dresselhaus, and M. S. Dresselhaus, Phys. Rev. B **61**, 2981 (2000).

[32] R. Saito and H. Kataura, in *Carbon Nanotubes, Topics Appl. Phys.*, edited by M. S. Dresselhaus, G. Dresselhaus, and P. Avouris (Springer-Verlag Berlin, Heidelberg, 2001), vol. 80, pp. 213–247.

[33] C. Thomsen and S. Reich, in *Light Scattering in Solid IX, Topics Appl. Physics*, edited by M. Cardona and R. Merlin (Springer-Verlag Berlin, Heidelberg, 2007), vol. 108, p. 115232.

[34] N. Minami, S. Kazaoui, R. Jacquemin, H. Yamawaki, K. Aoki, H. Kataura, and Y. Achiba, Synt. Met. **116**, 405 (2001).

[35] M. Y. Sfeir, T. Beetz, F. Wang, L. Huang, X. M. H. Huang, M. Huang, J. Hone, S. O'Brien, J. A. Misewich, T. F. Heinz, et al., Science **312**, 554 (2006).

[36] T. W. Odom, J.-L. Huang, P. Kim, and C. M. Lieber, J. Phys. Chem. B **104**, 2794 (2000).

[37] H. Kataura, Y. Kumazawa, Y. Maniwa, I. Umezu, S. Suzuki, Y. Ohtsuka, and Y. Achiba, Syn. Met. **103**, 2555 (1999).

[38] http://photon.t.u-tokyo.ac.jp/ maruyama/kataura/kataura.pdf.

[39] A. Kleiner and S. Eggert, Phys. Rev. B **64**, 113402 (2001).

[40] A. Kleiner and S. Eggert, Phys. Rev. B **63**, 073408 (2001).

[41] C. L. Kane and E. J. Mele, Phys. Rev. Lett. **78**, 1932 (1997).

REFERENCES

[42] H. J. Liu and C. T. Chan, Phys. Rev. B **66**, 115416 (2002).

[43] I. Cabria, J. W. Mintmire, and C. T. White, Phys. Rev. B **67**, 121406 (2003).

[44] V. N. Popov, New J. Phys. **6**, 17 (2004).

[45] A. Jorio, R. Saito, G. Dresselhaus, and M. S. Dresselhaus, Phil. Trans. R. Soc. Lond. A **362**, 2311 (2004).

[46] A. M. Rao, E. Richter, S. Bandow, B. Chase, P. C. Eklund, K. A. Williams, S. Fang, K. R. Subbaswamy, M. Menon, A. Thess, et al., Science **275**, 187 (1997).

[47] M. A. Pimenta, A. Marucci, S. A. Empedocles, M. G. Bawendi, E. B. Hanlon, A. M. Rao, P. C. Eklund, R. E. Smalley, G. Dresselhaus, and M. S. Dresselhaus, Phys. Rev. B **58**, R16016 (1998).

[48] G. Duesberg, W. Blau, H. Byrne, J. Muster, M. Burghard, and S. Roth, Chem. Phys. Lett. **310**, 8 (1999).

[49] A. Jorio, R. Saito, J. H. Hafner, C. M. Lieber, M. Hunter, T. McClure, G. Dresselhaus, and M. S. Dresselhaus, Phys. Rev. Lett. **86**, 1118 (2001).

[50] O. Dubay and G. Kresse, Phys. Rev. B **67**, 035401 (2003).

[51] R. Pfeiffer, H. Kuzmany, F. Simon, S. N. Bokova, and E. Obraztsova, Phys. Rev. B **71**, 155409 (2005).

[52] R. Jishi, L. Venkataraman, M. Dresselhaus, and G. Dresselhaus, Chem. Phys. Lett. **209**, 77 (1993).

[53] J. Kürti, G. Kresse, and H. Kuzmany, Phys. Rev. B **58**, R8869 (1998).

[54] D. Sánchez-Portal, E. Artacho, J. M. Soler, A. Rubio, and P. Ordejón, Phys. Rev. B **59**, 12678 (1999).

[55] G. D. Mahan, Phys. Rev. B **65**, 235402 (2002).

REFERENCES

[56] S. Bandow, G. Chen, G. U. Sumanasekera, R. Gupta, M. Yudasaka, S. Iijima, and P. C. Eklund, Phys. Rev. B **66**, 075416 (2002).

[57] S. D. M. Brown, A. Jorio, P. Corio, M. S. Dresselhaus, G. Dresselhaus, R. Saito, and K. Kneipp, Phys. Rev. B **63**, 155414 (2001).

[58] A. M. Rao, P. C. Eklund, S. Bandow, A. Thess, and R. E. Smalley, Nature **388**, 257 (1997).

[59] J. Maultzsch, S. Reich, U. Schlecht, and C. Thomsen, Phys. Rev. Lett. **91**, 087402 (2003).

[60] M. Hulman, R. Pfeiffer, and H. Kuzmany, New J. Phys. **6**, 1 (2004).

[61] A. G. Souza Filho, A. Jorio, G. G. Samsonidze, G. Dresselhaus, M. A. Pimenta, M. S. Dresselhaus, A. K. Swan, M. S. Ünlü, B. B. Goldberg, and R. Saito, Phys. Rev. B **67**, 035427 (2003).

[62] A. S. Filho, A. Jorio, G. Samsonidze, G. Dresselhaus, M. Dresselhaus, A. K. Swan, M. nl, B. Goldberg, R. Saito, J. Hafner, et al., Chem. Phys. Lett. **354**, 62 (2002), ISSN 0009-2614.

[63] S. Okubo, T. Okazaki, N. Kishi, S.-K. Joung, T. Nakanishi, S. Okada, and S. Iijima, J. Phys. Chem. C **113**, 571 (2009).

[64] A. Ryabenko, N. Kiselev, J. Hutchison, T. Moroz, S. Bukalov, L. Mikhalitsyn, R. Loutfy, and A. Moravsky, Carbon **45**, 1492 (2007).

[65] S. Okada, S. Saito, and A. Oshiyama, Phys. Rev. Lett. **86**, 3835 (2001).

[66] A. Oshiyama, S. Okada, and S. Saito, Physica B **323**, 21 (2002).

[67] A. Rochefort, Phys. Rev. B **67**, 115401 (2003).

[68] R. Pfeiffer, T. Pichler, Y. A. Kim, and H. Kuzmany, in *Carbon Nanotubes, Topics Appl. Phys.*, edited by A. Jorio, G. Dresselhaus, and M. S. Dresselhaus (Springer-Verlag Berlin, Heidelberg, 2008), vol. 111, p. 495.

REFERENCES

[69] R. Pfeiffer, H. Peterlik, H. Kuzmany, H. Shiozawa, A. Grneis, T. Pichler, and H. Kataura, phys. status solidi (b) **244**, 4097 (2007).

[70] F. Hasi, F. Simon, and H. Kuzmany, J. Nanosci. Nanotechnol. **5**, 1785 (2005).

[71] Y. Fujita, N. Niwa, S. Bandow, and S. Iijima, Appl. Phys. A Mater. Sci. Process. **85**, 307 (2006).

[72] A. L. Aguiar, A. San-Miguel, E. B. Barros, M. Kalbáč, D. Machon, Y. A. Kim, H. Muramatsu, M. Endo, and A. G. Souza Filho, Phys. Rev. B **86**, 195410 (2012).

[73] S. Bandow, T. Hiraoka, T. Yumura, K. Hirahara, H. Shinohara, and S. Iijima, Chem. Phys. Lett. **384**, 320 (2004).

[74] F. Ding, Z. Xu, B. I. Yakobson, R. J. Young, I. A. Kinloch, S. Cui, L. Deng, P. Puech, and M. Monthioux, Phys. Rev. B **82**, 041403 (2010).

[75] S. Han, M. Yoon, S. Berber, N. Park, E. Osawa, J. Ihm, and D. Tománek, Phys. Rev. B **70**, 113402 (2004).

[76] H. Ueno, S. Ōsawa, E. Ōsawa, and K. Takeuchi, Fullerene Sci. Technol. **6**, 319 (1998).

[77] M. S. Dresselhaus, G. Dresselhaus, and P. C. Eklund, *Science of fullerenes and carbon nanotubes* (Academic Press, San Diego, 1996).

[78] S.-P. Chan, W.-L. Yim, X. G. Gong, and Z.-F. Liu, Phys. Rev. B **68**, 075404 (2003).

[79] C. Caillier, D. Machon, A. San-Miguel, R. Arenal, G. Montagnac, H. Cardon, M. Kalbac, M. Zukalova, and L. Kavan, Phys. Rev. B **77**, 125418 (2008).

[80] A. L. Aguiar, E. B. Barros, R. B. Capaz, A. G. Souza Filho, P. T. C. Freire, J. M. Filho, D. Machon, C. Caillier, Y. A. Kim, H. Muramatsu, et al., J. Phys. Chem. C **115**, 5378 (2011).

REFERENCES

[81] R. Pfeiffer, H. Kuzmany, C. Kramberger, C. Schaman, T. Pichler, H. Kataura, Y. Achiba, J. Kürti, and V. Zólyomi, Phys. Rev. Lett. **90**, 225501 (2003).

[82] P. Puech, H. Hubel, D. J. Dunstan, R. R. Bacsa, C. Laurent, and W. S. Bacsa, Phys. Rev. Lett. **93**, 095506 (2004).

[83] A. San-Miguel, C. Cailler, D. Machon, E. Barros, A. Aguiar, and A. Filho, in *High-Pressure Crystallography*, edited by E. Boldyreva and P. Dera (Springer Netherlands, 2010), NATO Science for Peace and Security Series B: Physics and Biophysics, pp. 435–446.

[84] X. Yang, G. Wu, and J. Dong, Appl. Phys. Lett. **89**, 113101 (2006).

[85] V. Gadagkar, P. K. Maiti, Y. Lansac, A. Jagota, and A. K. Sood, Phys. Rev. B **73**, 085402 (2006).

[86] V. Gadagkar, S. Saha, D. Muthu, P. K. Maiti, Y. Lansac, A. Jagota, A. Moravsky, R. Loutfy, and A. Sood, J. Nanosci. Nanotechnol. **7**, 1753 (2007).

[87] K. V. Shanavas and S. M. Sharma, Phys. Rev. B **79**, 155425 (2009).

[88] L. Alvarez, J.-L. Bantignies, R. Le Parc, R. Aznar, J.-L. Sauvajol, A. Merlen, D. Machon, and A. San Miguel, Phys. Rev. B **82**, 205403 (2010).

[89] Y. Zou, B. Liu, L. Wang, D. Liu, S. Yu, P. Wang, T. Wang, M. Yao, Q. Li, B. Zou, et al., Proc. Natl. Acad. Sci. **106**, 22135 (2009).

[90] R. A. Serway and C. Vuille, *College Physics* (Charles Hartford, Boston, 2012), ninth ed.

[91] T. Deleporte, *Quantitative infrared Fourier transform spectroscopy: Absolute line intensities for $^{13}CO_2$ and HOBr* (Faculté des Sciences - Département de Physique, Université Libre de Bruxelles, 2008), ph.D thesis.

REFERENCES

[92] B. H. Stuart, *Infrared Spectroscopy: Fundamentals and Applications* (John Wiley Sons, Ltd, England, 2004).

[93] B. C. Smith, *Fundamentals of Fourier Transform Infrared Spectroscopy* (CRC Press - Taylor Francis Group, USA, 2011).

[94] P. L. King, M. S. Ramsey, and G. A. Swayze, *Infrared spectroscopy in geochemistry, exploration geochemistry and remote sensing*, vol. 33 (Mineralogical Association of Canada, Ottawa, 2004).

[95] P. Wilhelm and B. S. Chernev, in *Microscopy: Science, Technology, Applications and Education*, edited by A. Méndez-Vilas and J. Díaz (Formatex Research Center, 2010), vol. 3, pp. 2062–2071.

[96] M. Born and E. Wolf, *Principles of optics: Electromagnetic theory of propagation, interference, and diffraction of light* (Pergamon Press, London, 1959).

[97] K. Thirunavukkuarasu, *Carbon Nanostructures Under High Pressure Studied By Infrared Spectroscopy* (Mathematisch-Naturwissenschaftlichen Fakultät, Universität Augsburg, 2009), ph.D thesis.

[98] F. Wooten, *Optical properties of Solids* (Academic press, USA, 1972).

[99] M. Fox, *Optical properties of Solids* (Oxford University press, New York, USA, 2001).

[100] P. C. Sahu and N. V. C. Shekar, in *High Pressure Research on Materials* (Resonance, 2007), pp. 10–23.

[101] A. Jayaraman, Rev. Mod. Phys. **55**, 65 (1983).

[102] G. Huber, K. Syassen, and W. B. Holzapfel, Phys. Rev. B **15**, 5123 (1977).

[103] http://www.easylab.co.uk/ProductDetails.aspx?PID=56.

[104] S. Sugano and Y. Tanabe, J. Phys. Soc. Jpn. **13**, 880 (1958).

[105] D. F. Nelson and M. D. Sturge, Phys. Rev. **137**, A1117 (1965).

REFERENCES

[106] H. K. Mao, J. Xu, and P. M. Bell, J. Geophys. Res. **91**, 4673 (1986).

[107] J. D. Barnett, S. Block, and G. J. Piermarini, Rev. Sci. Instrum. **44**, 1 (1973).

[108] G. J. Piermarini, S. Block, J. D. Barnett, and R. A. Forman, J. Appl. Phys. **46**, 2774 (1975).

[109] T. Zhou, *Optical Spectroscopic Studies on Transition Metal Oxides and H_gO under High Pressure* (MPI for solid state research, Universität Stuttgart, 1998), ph.D thesis.

[110] Newport, MS260i 1/4M imaging spectrographs http://assets.newport.com/webDocuments-EN/images/12389.pdf.

[111] A. Abouelsayed, K. Thirunavukkuarasu, F. Hennrich, and C. A. Kuntscher, J. Phys. Chem. C **114**, 4424 (2010).

[112] S. Klotz, J.-C. Chervin, P. Munsch, and G. L. Marchand, J. Phys. D: Appl. Phys. **42**, 075413 (2009).

[113] Z. Wu, Z. Chen, X. Du, J. M. Logan, J. Sippel, M. Nikolou, K. Kamaras, J. R. Reynolds, D. B. Tanner, A. F. Hebard, et al., Science **305**, 1273 (2004).

[114] K. Hata, D. N. Futaba, K. Mizuno, T. Namai, M. Yumura, and S. Iijima, Science **306**, 1362 (2004).

[115] E. Flahaut, A. Peigney, W. S. Bacsa, R. R. Bacsa, and C. Laurent, J. Mater. Chem. **14**, 646 (2004).

[116] L. S. Panchakarla, A. Govindaraj, and C. N. R. Rao, ACS Nano **1**, 494 (2007).

[117] A. R. Biris, D. Lupu, A. Gruneis, P. Ayala, M. H. Rümmeli, T. Pichler, Z. Li, Y. Xu, I. Misan, E. Dervishi, et al., Chem. Mater. **20**, 3466 (2008).

[118] B. W. Smith, R. M. Russo, S. B. Chikkannanavar, F. Stercel, and D. E. Luzzi, Mater. Res. Soc. Symp. Proc. **706**, Z.313.1 (2002).

REFERENCES

[119] L. Guan, K. Suenaga, Z. Shi, Z. Gu, and S. Iijima, Nano Lett. **7**, 1532 (2007).

[120] F. Banhart, Rep. Prog. Phys. **62**, 1181 (1999).

[121] B. W. Smith, M. Monthioux, and D. E. Luzzi, Nature **396**, 323 (1999).

[122] K. Suenaga, T. Okazaki, C.-R. Wang, S. Bandow, H. Shinohara, and S. Iijima, Phys. Rev. Lett. **90**, 055506 (2003).

[123] S. Bandow, M. Takizawa, K. Hirahara, M. Yudasaka, and S. Iijima, Chem. Phys. Lett. **337**, 48 (2001).

[124] S. Bandow, M. Takizawa, H. Kato, T. Okazaki, H. Shinohara, and S. Iijima, Chem. Phys. Lett. **347**, 23 (2001).

[125] S. Okada, Chem. Phys. Lett. **438**, 59 (2007).

[126] S.-K. Joung, T. Okazaki, S. Okada, and S. Iijima, Phys. Chem. Chem. Phys. **12**, 8119 (2010).

[127] A. H. R. Palser, Phys. Chem. Chem. Phys. **1**, 4459 (1999).

[128] M. Kawai, H. Kyakuno, T. Suzuki, T. Igarashi, H. Suzuki, T. Okazaki, H. Kataura, Y. Maniwa, and K. Yanagi, J. Am. Chem. Soc. **134**, 9545 (2012).

[129] B. Anis, M. Fischer, M. Schreck, K. Haubner, L. Dunsch, and C. A. Kuntscher, phys. stat. sol. (b) **249**, 2345 (2012).

[130] A. N. Khlobystov, R. Scipioni, D. Nguyen-Manh, D. A. Britz, D. G. Pettifor, G. A. D. Briggs, S. G. Lyapin, A. Ardavan, and R. J. Nicholas, Appl. Phys. Lett. **84**, 792 (2004).

[131] B. Verberck and K. H. Michel, Phys. Rev. B **75**, 045419 (2007).

[132] B. Verberck, Phys. Rev. B **83**, 045405 (2011).

[133] P. M. Rafailov, C. Thomsen, and H. Kataura, Phys. Rev. B **68**, 193411 (2003).

REFERENCES

[134] L. Kavan, L. Dunsch, H. Kataura, A. Oshiyama, M. Otani, and S. Okada, J. Phys. Chem. B **107**, 7666 (2003).

[135] D. S. Bethune, G. Meijer, W. C. Tang, H. J. Rosen, W. G. Golden, H. Seki, C. A. Brown, and M. S. de Vries, Chem. Phys. Lett. **179**, 181 (1991).

[136] K. Hirahara, K. Suenaga, S. Bandow, H. Kato, T. Okazaki, H. Shinohara, and S. Iijima, Phys. Rev. Lett. **85**, 5384 (2000).

[137] H. Kuzmany, R. Pfeiffer, C. Kramberger, T. Pichler, X. Liu, M. Knupfer, J. Fink, H. Kataura, Y. Achiba, B. Smith, et al., Appl. Phys. A **76**, 449 (2003).

[138] H. Kuzmany, R. Pfeiffer, F. Simon, C. Kramberger, M. Hulman, and P. Costa, Fullerenes, Nanotubes and Carbon Nanostruct. **13**, 179 (2005).

[139] V. Schettino, M. Pagliai, and G. Cardini, J. Phys. Chem. A **106**, 1815 (2002).

[140] S. H. Gallagher, R. S. Armstrong, R. D. Bolskar, P. A. Lay, and C. A. Reed, J. Am. Chem. Soc. **119**, 4263 (1997).

[141] M. Kalbac, L. Kavan, M. Zukalova, and L. Dunsch, Adv. Funct. Mater. **15**, 418 (2005).

[142] V. N. Popov and P. Lambin, Phys. Rev. B **73**, 165425 (2006).

[143] H. Rauf, T. Pichler, R. Pfeiffer, F. Simon, H. Kuzmany, and V. N. Popov, Phys. Rev. B **74**, 235419 (2006).

[144] A. Jorio, G. Dresselhaus, M. S. Dresselhaus, M. Souza, M. S. S. Dantas, M. A. Pimenta, A. M. Rao, R. Saito, C. Liu, and H. M. Cheng, Phys. Rev. Lett. **85**, 2617 (2000).

[145] R. Pfeiffer, F. Simon, H. Kuzmany, and V. N. Popov, Phys. Rev. B **72**, 161404 (2005).

[146] Z. Wang, L. Wang, Z. Shi, J. Lu, Z. Gu, and Z. Gao, Chem. Commun. p. 3429 (2008).

REFERENCES

[147] G. U. Sumanasekera, J. L. Allen, S. L. Fang, A. L. Loper, A. M. Rao, and P. C. Eklund, J. Phys. Chem. B **103**, 4292 (1999).

[148] K. Kamará, K. Thirunavukkuarasu, C. Kuntscher, M. Dressel, F. Simon, H. Kuzmany, D. Walters, and D. Moss, Infrared Phys. Technol. **49**, 35 (2006).

[149] M. E. Itkis, S. Niyogi, M. E. Meng, M. A. Hamon, H. Hu, and R. C. Haddon, Nano Lett. **2**, 155 (2002).

[150] F. Hennrich, R. Wellmann, S. Malik, S. Lebedkin, and M. M. Kappes, Phys. Chem. Chem. Phys. **5**, 178 (2003).

[151] F. Hennrich, S. Lebedkin, S. Malik, J. Tracy, M. Barczewski, H. Rosner, and M. Kappes, Phys. Chem. Chem. Phys. **4**, 2273 (2002).

[152] N. Akima, Y. Iwasa, S. Brown, A. Barbour, J. Cao, J. Musfeldt, H. Matsui, N. Toyota, M. Shiraishi, H. Shimoda, et al., Adv. Mater. **18**, 1166 (2006).

[153] U. J. Kim, X. M. Liu, C. A. Furtado, G. Chen, R. Saito, J. Jiang, M. S. Dresselhaus, and P. C. Eklund, Phys. Rev. Lett. **95**, 157402 (2005).

[154] V. Kovalenko, R. Mukhamadeeva, L. Maklakova, and N. Gustova, J. Struct. Chem. **34**, 540 (1994).

[155] U. J. Kim, C. A. Furtado, X. Liu, G. Chen, and P. C. Eklund, J. Am. Chem. Soc. **127**, 15437 (2005).

[156] P. E. Fanning and M. Vannice, Carbon **31**, 721 (1993).

[157] F. Lapointe, E. Gaufrès, I. Tremblay, N. Y.-W. Tang, R. Martel, and P. Desjardins, Phys. Rev. Lett. **109**, 097402 (2012).

[158] R. Saito, G. Dresselhaus, and M. S. Dresselhaus, J. Appl. Phys. **73**, 494 (1993).

[159] W. Song, M. Ni, J. Lu, Z. Gao, S. Nagase, D. Yu, H. Ye, and X. Zhang, Chem. Phys. Lett. **414**, 429 (2005).

REFERENCES

[160] J. Chen, X. Wang, S. Leng, and Z. Yang, Phys. Lett. A **351**, 105 (2006).

[161] R. Jacquemin, S. Kazaoui, D. Yu, A. Hassanien, N. Minami, H. Kataura, and Y. Achiba, Synt. Met. **115**, 283 (2000), ISSN 0379-6779.

[162] H. Hu, B. Zhao, M. A. Hamon, K. Kamaras, M. E. Itkis, and R. C. Haddon, J. Am. Chem. Soc. **125**, 14893 (2003).

[163] S. J. Yosim, J. Chem. Phys. **40**, 3069 (1964).

[164] A. Abouelsayed, *Pressure effect on Single-walled and Double-walled Carbon Nanotubes Investigated by Infrared Spectroscopy* (Mathematisch-Naturwissenschaftlichen Fakultät, Universität Augsburg, 2012), ph.D thesis.

[165] S. Kazaoui, N. Minami, H. Yamawaki, K. Aoki, H. Kataura, and Y. Achiba, Phys. Rev. B **62**, 1643 (2000).

[166] J. Wu, W. Walukiewicz, W. Shan, E. Bourret-Courchesne, J. W. Ager, K. M. Yu, E. E. Haller, K. Kissell, S. M. Bachilo, R. B. Weisman, et al., Phys. Rev. Lett. **93**, 017404 (2004).

[167] K. Thirunavukkuarasu, F. Hennrich, K. Kamarás, and C. A. Kuntscher, Phys. Rev. B **81**, 045424 (2010).

[168] C. A. Kuntscher, A. Abouelsayed, K. Thirunavukkuarasu, and F. Hennrich, Phys. Status Solidi (b) **247**, 2789 (2010).

[169] C. A. Kuntscher, A. Abouelsayed, . Botos, . Pekker, and K. Kamarás, Phys. Status Solidi (b) **248**, 2732 (2011).

[170] J. C. Charlier, P. Lambin, and T. W. Ebbesen, Phys. Rev. B **54**, R8377 (1996).

[171] G. Liu, X. Wang, J. Chen, and H. Lu, phys. status solidi (b) **245**, 689 (2008).

[172] R. S. Deacon, K.-C. Chuang, J. Doig, I. B. Mortimer, and R. J. Nicholas, Phys. Rev. B **74**, 201402 (2006).

REFERENCES

[173] A. Abouelsayed, K. Thirunavukkuarasu, K. Kamars, F. Hennrich, and C. A. Kuntscher, High Pressure Research **29**, 559 (2009).

[174] M. Yao, Z. Wang, B. Liu, Y. Zou, S. Yu, W. Lin, Y. Hou, S. Pan, M. Jin, B. Zou, et al., Phys. Rev. B **78**, 205411 (2008).

[175] P. T. Araujo, N. M. Barbosa Neto, H. Chacham, S. S. Carara, J. S. Soares, A. D. Souza, L. G. Canado, A. B. de Oliveira, R. J. C. Batista, E. Joselevich, et al., Nano Lett. **12**, 4110 (2012).

[176] J. Tersoff and R. S. Ruoff, Phys. Rev. Lett. **73**, 676 (1994).

[177] M. J. López, A. Rubio, J. A. Alonso, L.-C. Qin, and S. Iijima, Phys. Rev. Lett. **86**, 3056 (2001).

[178] R. B. Capaz, C. D. Spataru, P. Tangney, M. L. Cohen, and S. G. Louie, Phys. Status Solidi (b) **241**, 3352 (2004).

[179] M. H. F. Sluiter and Y. Kawazoe, Phys. Rev. B **69**, 224111 (2004).

[180] J. A. Elliott, J. K. W. Sandler, A. H. Windle, R. J. Young, and M. S. P. Shaffer, Phys. Rev. Lett. **92**, 095501 (2004).

[181] M. Hasegawa and K. Nishidate, Phys. Rev. B **74**, 115401 (2006).

[182] U. D. Venkateswaran, A. M. Rao, E. Richter, M. Menon, A. Rinzler, R. E. Smalley, and P. C. Eklund, Phys. Rev. B **59**, 10928 (1999).

[183] M. J. Peters, L. E. McNeil, J. P. Lu, and D. Kahn, Phys. Rev. B **61**, 5939 (2000).

[184] J. Sandler, M. S. P. Shaffer, A. H. Windle, M. P. Halsall, M. A. Montes-Morán, C. A. Cooper, and R. J. Young, Phys. Rev. B **67**, 035417 (2003).

[185] B. Anis, K. Haubner, F. Börrnert, L. Dunsch, M. H. Rümmeli, and C. A. Kuntscher, Phys. Rev. B **86**, 155454 (2012).

[186] K. Gao, R. Dai, Z. Zhao, Z. Zhang, and Z. Ding, Solid State Commun. **147**, 65 (2008).

REFERENCES

[187] M. S. Amer, M. M. El-Ashry, and J. F. Maguire, J. Chem. Phys. **121**, 2752 (2004).

[188] S. Rols, M. R. Johnson, P. Zeppenfeld, M. Bienfait, O. E. Vilches, and J. Schneble, Phys. Rev. B **71**, 155411 (2005).

[189] S. Agnihotri, J. P. B. Mota, M. Rostam-Abadi, and M. J. Rood, Langmuir **21**, 896 (2005).

[190] A. Merlen, N. Bendiab, P. Toulemonde, A. Aouizerat, A. San Miguel, J. L. Sauvajol, G. Montagnac, H. Cardon, and P. Petit, Phys. Rev. B **72**, 035409 (2005).

[191] K. Kamaras, M. E. Itkis, H. Hu, B. Zhao, and R. C. Haddon, Science **301**, 1501 (2003).

[192] W. Bu, J. Jiang, and J. Dong, Phys. Lett. A **302**, 125 (2002).

[193] J. Arvanitidis, D. Christofilos, K. Papagelis, K. S. Andrikopoulos, T. Takenobu, Y. Iwasa, H. Kataura, S. Ves, and G. A. Kourouklis, Phys. Rev. B **71**, 125404 (2005).

[194] P. Puech, E. Flahaut, A. Sapelkin, H. Hubel, D. J. Dunstan, G. Landa, and W. S. Bacsa, Phys. Rev. B **73**, 233408 (2006).

[195] J. Arvanitidis, D. Christofilos, G. A. Kourouklis, S. Ves, T. Takenobu, Y. Iwasa, and H. Kataura, High Pressure Res. **28**, 591 (2008).

[196] S. Kawasaki, T. Hara, T. Yokomae, F. Okino, H. Touhara, H. Kataura, T. Watanuki, and Y. Ohishi, Chem. Phys. Lett. **418**, 260 (2006).

[197] M. Chorro, S. Rols, J. Cambedouzou, L. Alvarez, R. Almairac, J.-L. Sauvajol, J.-L. Hodeau, L. Marques, M. Mezouar, and H. Kataura, Phys. Rev. B **74**, 205425 (2006).

[198] Y. Zou, B. Liu, M. Yao, Y. Hou, L. Wang, S. Yu, P. Wang, B. Li, B. Zou, T. Cui, et al., Phys. Rev. B **76**, 195417 (2007).

156

REFERENCES

[199] R. Poloni, M. V. Fernandez-Serra, S. Le Floch, S. De Panfilis, P. Toulemonde, D. Machon, W. Crichton, S. Pascarelli, and A. San-Miguel, Phys. Rev. B **77**, 035429 (2008).

[200] C. Thomsen, S. Reich, A. R. Goi, H. Jantoljak, P. M. Rafailov, I. Loa, K. Syassen, C. Journet, and P. Bernier, phys. status solidi (b) **215**, 435 (1999).

[201] N. M. Pugno and J. A. Elliott, Physica E **44**, 944 (2012).

[202] N. M. Pugno, J. Mech. Phys. Solids **58**, 1397 (2010).

[203] K. N. Kudin, G. E. Scuseria, and B. I. Yakobson, Phys. Rev. B **64**, 235406 (2001).

[204] U. D. Venkateswaran, E. A. Brandsen, M. E. Katakowski, A. Harutyunyan, G. Chen, A. L. Loper, and P. C. Eklund, Phys. Rev. B **65**, 054102 (2002).

[205] E. Philp, J. Sloan, A. I. Kirkland, R. R. Meyer, S. Friedrichs, J. L. Hutchison, and M. L. H. Green, Nat. Mater. **2**, 788 (2003).

[206] H. Olijnyk, W. Li, and A. Wokaun, Phys. Rev. B **50**, 712 (1994).

[207] A. Congeduti, P. Postorino, M. Nardone, and U. Buontempo, Phys. Rev. B **65**, 014302 (2001).

Acknowledgements

Curriculum Vitae

Personal information

Date of birth	01 January 1978
Nationality	Egyptian
Gender	Male
Martial status	Married

Education

Sep 1983 - May 1995	All Egyptian Primary and Secondary Schools.
Sep 1995 - May 1999	Bachelor's degree in Physics and Chemistry , Faculty of Science, Physics Department, Cairo University, El-Fayoum, Egypt.
Sept 2002 - Sept 2003	Pre-Master studies of Physics, Faculty of Science, Physics Department, El-Fayoum University, Cairo, Egypt.
April 2004 - Sep 2005	Master project at Fayoum University, Fayoum, Egypt; title of the Master Thesis: Investigation of some Physical Properties of Methyl-2-Hydroxyethyl Cellulose Doped with Rare Earth Metal Salts
Sep 2005	Master degree in Physics.
Since June 2006	Researcher Assistant, Spectroscopy Department, Physics Division, National Research Center Giza, Egypt.
May 2007 - Sep 2009	Enrolled in a Ph.D. Program at El-Mansoura University, El-Mansoura , Egypt; title of the Ph.D thesis: Studies on the Effect of Particle Size and Structure on the Optical and Electrical Properties of some Nanoparticle Materials

September 2009	Ph.D programme at El-Mansoura University cancelled.
May 2009	Awarded DAAD scholarship.
Oct - April 2010	Studies of German language at Goethe institute, Freiburg , Germany.
April 2010	Ph.D project at the Institut für Physik, Universität Augsburg within the frame of a DAAD scholarship.
September 2013	PhD examination at the Universität Augsburg, title of PhD thesis: Stabilization of Carbon Nanotubes: An Infrared and Optical Spectroscopy Study on Peapods and Double-Walled Carbon Nanotubes under Pressure.

List of Publications

- *Synthesis and characterization of peapods and DWCNTs.*
  B. Anis, M. Fischer, M. Schreck, K. Haubner, L. Dunsch and
  C. A. Kuntscher, Phys. Status Solidi B **249**, 2345 (2012).

- *Stabilization of carbon nanotubes by filling with inner tubes: An optical spectroscopy study on double-walled carbon nanotubes under hydrostatic pressure.*
  B. Anis, K. Haubner, F. Brrnert, L. Dunsch, M. H. Rmmeli and
  C. A. Kuntscher **86**, 155454 (2012).

- *Effect of stabilizing agent on the morphology and optical properties of silver nanoparticles.*
  R. Seoudi , A. Shabaka, Z. A. El Sayed, and B. Anis, Physica E
  44,440 (2011).

- *Effect of the prepared temperature on the size of CdS and ZnS nanoparticle.*
  R. Seoudi, A. Shabaka, W. H. Eisa, B. Anis, and N.M. Farage,
  Physica E **409**, 919 (2010).

- *Differential scanning calorimetry and dielectric properties of methyl-2-hydroxyethyl cellulose doped with erbium nitrate salt.*
  G. Said, F. H. Abd-El Kader, M. M. El-Naggar, and B. Anis,
  Carbohydrate Polymers **65**, 253 (2006).

- *Characterization and electrical properties of methyl-2-hydroxyethyl cellulose doped with erbium nitrate salt.*
  F.H. Abd-El Kader, G. Said, B. Anis and M.M. El-Naggar, Journal of Applied Polymer Science **102**, 2352 (2006).